Flow Systems Integrating Heterogeneous Catalysts and Quinone Mediators Enable Power Generation and H_2-Promoted Electrosynthesis

By

Mathew R. Johnson

A dissertation submitted in partial fulfillment of
the requirements for the degree of

Doctor of Philosophy
(Chemistry)

at the
UNIVERSITY OF WISCONSIN-MADISON
2022

Date of final oral examination: 11/18/2022

The dissertation is approved by the following members of the Final Oral Committee:

Shannon S. Stahl, Professor, Chemistry
Thatcher W. Root, Professor, Chemical Engineering
Kyoung-Shin Choi, Professor, Chemistry
Ive Hermans, Professor, Chemistry

Flow Systems Integrating Heterogeneous Catalysts and Quinone Mediators Enable Power Generation and H_2-Promoted Electrosynthesis

By Mathew R. Johnson

Under the supervision of Professor Shannon S. Stahl

At the University of Wisconsin – Madison

Abstract

Molecular redox mediators incorporated into electrochemical systems can enable a wide array of redox processes for energy storage and energy conversion applications. These mediators are oxidized or reduced at an electrode interface, are transported into the bulk solution, and are then regenerated through reaction with a chemical substrate (frequently in a catalyzed process). Mediators allow engagement of substrates that are otherwise transport-limited, such as those which are poorly soluble or bound to a solid. They also obviate the need for fast on-electrode kinetics for the terminal reagent. For these reasons, mediators are frequently encountered in biological systems (e.g., quinones in the Calvin cycle, cytochrome c in the electron transport chain) and are a critical component of redox flow batteries. Use of mediators also continues to provide opportunity for the development of new fuel cell technologies and electrosynthesis applications.

This dissertation demonstrates the design and implementation of fuel cell systems with cathodic and anodic redox mediators, an electrosynthetic system utilizing mediators to enable hydrogen-driven cross-electrophile coupling, and non-PGM heterogeneous catalysts for mediator regeneration. It explores both conceptual similarities in the development of these systems and specific challenges for each. **Chapter 1** of this work includes a preface for the non-expert, aimed

at contextualizing this work for the taxpayers who funded much of it and for whom it will be made publicly available. This chapter will then introduce the field of mediator-driven electrocatalysis and will provide several examples of existing fuel cell and organic electrosynthesis systems intended to give the reader context for the innovations presented in subsequent chapters. It will briefly characterize the major components of flow systems designed for these applications. **Chapter 2** will focus on two mediated fuel cell designs, one pairing a traditional hydrogen anode with a mediated cathode and the other demonstrating a dually mediated system. **Chapter 3** will extend this concept from fuel cells to demonstrate that the same lessons can enable reductive synthesis of high-value, pharmaceutically relevant molecules using a mediated hydrogen anode. All of these systems make use of heterogeneous catalysts for chemical regeneration of mediator species, and so **Chapter 4** will introduce the class of non-precious metal "M-N-C" catalysts. It will describe them, summarize their applications for organic chemistry, and then describe synthesis and characterization of several such materials, with an emphasis on lessons learned for further synthetic optimization. **Appendix 1** will be appended to the main text and will recount two strategies that were explored for incorporating heterogeneous catalysts into a flow system without using small granular solids in a packed bed.

Acknowledgements

I owe many acknowledgments to those who have helped me to complete this body of work.

Professionally, I would like to acknowledge:

- Professor Shannon Stahl, who has been a tireless advisor, who sets a superlative example as a dedicated researcher, and whose constant commitment to academic rigor has helped me become a better scientist.
- Professor Thatcher Root, who has been more generous with his time than any student could reasonably expect, who has been an invaluable resource as I learned to analyze data and plan experiments, and whose extensive feedback has been an essential part of my professional development in graduate school.
- Several collaborators, without whom this thesis would be impoverished. I owe thanks to:
    - the members of the Center for Molecular Electrocatalysis (particularly Professor Yogesh Surendranath and William Howland)
    - the electrochemists in the process development team at Merck (particularly Drs. François Lévesque, Dan Lehnherr, and Cecilia Bottecchia)
    - the facilities within the Chemistry Department which have supported my research and encouraged my creative drive (particularly Steve Meyers and Tracy Drier)
- The many peers I have had the good fortune to learn from during my tenure as a graduate student. They are too numerous to name exhaustively, but not too numerous to appreciate. Particular thanks to Dr. Yulia Preger, an excellent and encouraging mentor; Dr. James

Gerken, whose incredible depth of expertise remains largely unplumbed even after more than five years of my best efforts; and to Vinayak Sidana, for his patience and good cheer as I've learned to be a mentor myself.

- And finally, to the Stahl group as a whole. Academic groups have a great deal of turnover, so I am especially grateful for the work everyone has done and continues to do to ensure that we remain unfailingly friendly and collegial despite the changing faces.

On a personal note, I cannot adequately express my gratitude for the people who have offered love, kindness, and support as I took on the challenging task of completing this degree. Countless thanks to:

- My partners, Amanda Johnson and Kirbie Luther. You're both the best, and I count myself lucky to have your love.
- My family, who are very far away but rarely absent from my life. Special thanks are due to my parents, whose unfailing support is not taken for granted, and to my newer family by marriage, whose enthusiastic welcome continues to mean a great deal to me.
- The many friends I have had the pleasure to meet here in Wisconsin, and the smaller number I have had the great fortune to maintain across trials of time and distance. Special thanks to Gabriel Acosta, J.D., and to Tori Venter for providing the relaxation and fun that everyone needs to stay productive.

Table of Contents

Chapter 1

Use of Redox Mediators for Mediated Fuel Cells and Mediated Electrosynthesis

Parts of this chapter have been submitted for publication. A credit statement is provided below to clarify this author's contributions.

- Johnson wrote the section included within this dissertation.
- Johnson and Stahl created the included graphic.
- Johnson, Stahl, and Gebbie edited the text of section 1.2 for content and clarity.

Carroll, G. A.; Gebbie, M. A.; Stahl, S. S.; Johnson, M. R.; Luca O.; Peterson, H.; Bomble, Y.; Neale, N. R.; and Cortright, R. The Prospect of Alternative Energy Carriers: Unique Interfaces for Electrochemical Hydrogenic Transformations. Submitted to *Adv. Ener. Lett.* **2022**.

1.1 Preface for the Non-Scientific Reader

This preface exists to partially rectify the problem of impenetrability that is common to scientific writing. The text in this document is intended to be read by experts in the domains of chemistry and chemical engineering. Care has been taken to define terms and to make acronyms explicit, but it is not possible within this dissertation to provide meaning and context to the dozens of concepts that are provided to professional researchers through years of education and that may be opaque or confusing to the layman. This presents a moral dilemma, since most of the funding for this research was provided by taxpayers who largely fall into this category and who might thereby reasonably hope to benefit from its summation. A careful lay reader *should* be able to glean useful information from the introductions in **Chapter 1** and at the start of each subsequent chapter, and should be able to follow the causative sequence described within each section to understand and appreciate the major conclusions. The rationale for many of the steps taken and the data that leads to those conclusions, however, will perforce be technical in nature and may create a barrier to deeper understanding. This short section, provided at the very beginning of the text, aims to mitigate these conceptual barriers by giving digestible summaries of a couple of major concepts that are crucial to the understanding of this research and of chemical research more generally.

The body of work described herein focuses largely on systems that either generate energy in the form of electricity or, conversely, that use electricity to provide energy and drive reactions which need it to take place. (The former is called power generation, the latter, electrosynthesis). As such, it is appropriate to contextualize this section in terms of how reactions make use of, and then sometimes release, energy. Chemical education typically broaches this subject by use of a “reaction coordinate diagram,” but here we can be less concrete. Let’s instead adopt a metaphor used by Max Tegmark, MIT physics professor, who has described other abstract concepts to non-scientists in terms of a ball, hills, and valleys.[1] If we imagine a ball in this sort of topologically diverse environment, it immediately becomes apparent that it can only lay at rest in a valley. (If it were on a slope, of course, it would be rolling downward even as we imagine it). This ball represents all the chemicals we're hoping to see react, and the valley in which it rests initially is the stable state of the starting materials. The role of a chemist is to identify interesting combinations of chemicals (fun balls, to carry the metaphor), and then to make them "react," which is to say to move them from one valley to another (carefully chosen) one. If we imagine that this new valley is on the other side of a hill from our starting place, it certainly appears that we have some work to do! The ball will need to be pushed up the hill until it reaches the summit, after which it can be rolled downward without further effort, and will actually generate some energy of its own while it rolls.

The large majority of reaction design can be understood using this simple paradigm. An energy-generating system is one in which the final valley sits at a lower elevation than the initial one, with the free-rolling ball on the backslope creating more energy as it rolls than was put into the system to get it up the hill. A system that consumes energy is one where the final valley is at a *higher* elevation than the initial one – although, crucially, even energy-generating systems need to get over the hill before they can start rolling, and so will need to satisfy their "activation energy" in order to react. Energy is commonly provided to reactions in the form of heat, light, electricity, or mechanical force; we predominantly focus here on the use of electricity as an energy-carrying medium, delivering energy from one starting molecule's reaction to fuel the reaction of another and sometimes making an "energy profit" that we can extract as power. Catalysis is a common theme throughout this dissertation, and a catalyst can be thought of as a tunnel-boring drill, a tool that allows us to get from one valley to another without climbing the entire hill in between them, doing so by creating an alternative, lower-barrier route between the two. When “chemical selectivity” is discussed, it refers to our ability to decide which valley the ball ends up in after it has been pushed; this is a hugely complex domain, but much of the screening of reaction components, solvents, and other conditions can be thought of as means of controlling this variable. Taken together, the field of chemistry is basically hundreds of tiny sub-skills and esoteric pieces of knowledge focused on getting balls to the desired valleys as quickly, cheaply, and safely as possible.

It is well worth noting, though, that even taking everything we have learned above into account fails to explain the significant complexity of the systems that we will shortly begin describing. Nothing said so far provides a compelling reason to ever deviate from the reaction setup of dumping starting chemicals into a bucket and then heating or electrifying it. This sort of batch chemistry *does* have its place, and indeed slightly more complex versions of this setup are featured within the following chapters. Most of our systems work by doing *flow* electrochemistry, however; they feature additional complexities such as recirculating reservoirs, gas diffusion layers, packed bed reactors, and pumps to move liquid between all these components. These components can generally be considered to be solving “kinetic” and/or “mass transport” problems. Said another way, these innovations are designed to ensure that all of our components mix together fast enough for the different reaction starting materials (and the intermediates they make on the way to becoming the final product) to efficiently combine and form the desired product(s). They do not typically determine which product is made – this is not how we control where the ball ends up –

but they *do* help ensure that the ball starts rolling and finishes in a timely fashion, and they are a critical piece of making systems that can be feasibly implemented in industrial labs to make tons of product, rather than being limited to the academy.

Keep these energetic and kinetic factors in mind as you continue reading into the following sections. The vast majority of the results to come are simply steps towards very specific iterations of the goals we have highlighted here.

1.2 Redox Mediators for Fuel Cells and Organic Electrosynthesis

Molecular redox mediators can serve as energy carriers equipped to use renewable electricity to drive diverse redox processes for energy storage and conversion. Energy conversion includes chemical synthesis of products not readily integrated within conventional electrochemical systems. Molecular mediators under consideration here undergo liquid-phase oxidation or reduction at the electrode interface (**Fig. 1.1**). They are then transported (e.g., by convection, diffusion) into the bulk solution where they undergo chemical reaction with a substrate molecule or with a catalyst species that subsequently reacts with the substrate of interest. In this process, the mediator effectively serves as a "soluble electrode," capturing the energy supplied by the solid electrode and delivering it elsewhere within the system. Various types of mediated redox reactions are possible, but they most commonly feature electron transfer (ET) or electron-proton transfer (EPT) reactions. ET and EPT mediators are widely encountered in biology. For example, photosynthesis involves the use of quinones (EPT mediators) and other molecular species to shuttle electrons between enzymes in reaction pathways such as the reverse Krebs cycle and the Calvin cycle. Similarly, mitochondrial respiration leverages quinones, cytochrome c (ET mediator), and other diffusible ET and EPT mediators to support NADH oxidation by O_2. This net reaction releases energy, akin to H_2 oxidation by O_2 in a fuel cell, and this energy provides the driving force to pump protons across a membrane to promote ATP synthesis.[2] Redox flow batteries (RFBs) pair high-potential and low-potential mediators in a liquid-phase electrochemical cell that stores and releases electrochemical energy via reversible ET or EPT redox reactions of the mediators at the electrode. These biological and RFB examples validate the utility of dissolved mediators as energy carriers for energy transduction and storage, and they provide a foundation for development of mediated EHT applications, ranging from fuel cells to chemical synthesis.

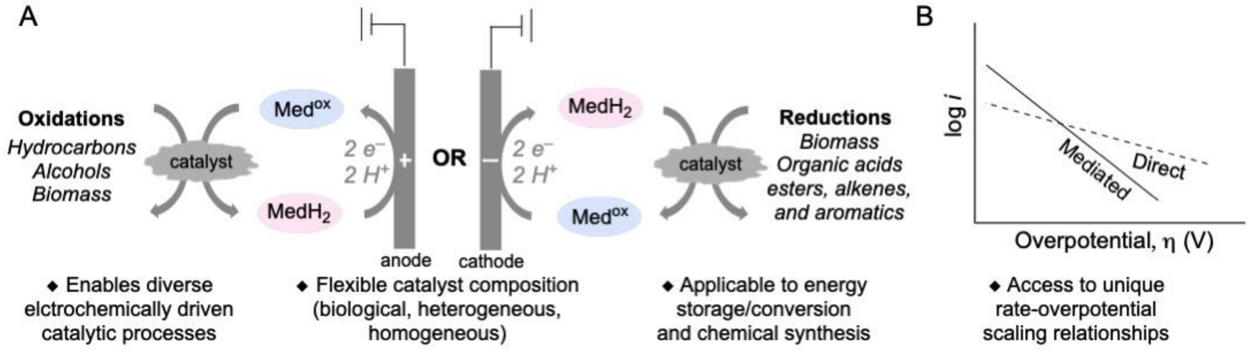

Figure 1.1: A. Mediated electrochemistry provide a means to enable diverse electricity-driven redox processes that may be challenging via direct electrolysis. B. Different thermodynamic-kinetic scaling relationships are among the potential opportunities that may be realized via mediated electrolysis.[3]

Mediated EHT has been the focus of historical attention for power generation, using both conventional and non-conventional fuels.[4, 5] Polymer electrolyte membrane fuel cells (PEMFCs) typically work by coupling anodic reaction of a fuel such as H_2 and cathodic reaction of an oxidant such as O_2 to form a galvanic cell, with charge balance and reaction stoichiometry maintained by migration of protons through a hydrated polymeric separator. Desirable alternative fuels such as alcohols or biomass feedstocks can be challenging to use in typical PEMFC configurations due to their low aqueous solubility and/or poor catalytic kinetics at the electrode interface. Development of fuel cells that employ mediators in liquid-phase electrolytes can address several limitations that have been encountered, including electrode ‘flooding’ with liquid fuels, mass transport limitations of complex substrates to the electrode surface, and challenges with solid or sparingly soluble fuels in aqueous electrolyte.

Both inorganic and molecular mediators have been used to good effect, enabling fuel cell concepts to be demonstrated with a wide variety of fuels. Inorganic mediators, including Fe^{2+}/Fe^{3+} complexes or salts and polyoxometalates (POMs), have been used in fuel cells that oxidize alcohols,[6,7] sugars,[8] biomass,[9-11] and even coal.[12] The iron systems are notable for often achieving relatively high power densities of 50-100 mW/cm^2 while operating with challenging fuels such as glucose, wheat, or grasses. POM systems frequently operate at lower current densities, and often require the integration of separate chemical and electrochemical processes; however, these materials interface well with heterogeneous or polymeric feedstocks and resist poisoning. Substituted quinones are among the most commonly used organic energy carriers for EHT in fuel cells. Fuel cell systems have been demonstrated that incorporate organic mediators for oxidation of alcohols, sugars, and lignin.[13-15] The energy output, duration of operation, and experimental parameters in these demonstrations are still relatively poor and will require further improvement to achieve commercial viability. Quinone systems can be tuned by the addition of various substituents to the central ring to promote solubility and to adjust the redox potential, making them well-suited as tunable energy carriers. This concept has been demonstrated in mediated fuel cell cathodes[16] and anodes.[17]

These same mediator concepts have been leveraged for electrochemical synthesis, where the end goal of the EHT is generation of a value-added product rather than electricity. Mediated electrolysis frequently leads to advantages in chemoselectivity.[18] Inorganic and organic mediator species have been applied for this purpose and have facilitated both installation of attractive functional groups during synthetic efforts and production of commodity chemicals.[19-22] Additional value can be found by harnessing mediated systems to improve product purity via phase-transfer technology.[23] The mediator is a crucial enabling technology for this application, avoiding gas diffusion kinetics which might hinder a solid electrode and allowing for interfacial reaction between species in different liquid streams, which is frequently impractical for direct electrochemical systems. As emphases on atom economy and green chemistry continue to foster the growth of industrial electrochemistry, approaches to maximize product purity and minimize cross-contamination during mediated electrolysis are expected to become more important.

Key basic science challenges remain as this field evolves. The multiple requirements for an appropriate mediator – stability, solubility, redox potential, electrochemical and thermal kinetics – sometimes make it challenging to identify candidates for a given system. The design of new mediators and chemical modification of existing ones to optimize properties of interest represent key molecular/materials synthesis challenges.[24,25] This issue is especially evident with high-potential organic mediators, owing to the common instability of highly oxidizing organic molecules.[26] In the field of energy storage, research efforts have demonstrated that modifications to mediators like fluorenone or *N*-oxyl species can enhance stability and tune redox potentials to improve system voltages.[27,28] Synthetically modulating a mediator’s potential is especially impactful given that energy carriers can be used to escape the limits of traditional electrochemical Tafel slopes, enabling higher catalytic rates at lower overpotentials (Figure 4B).[29] As new mediated systems are identified, it will also become increasingly important to determine the mechanisms by which they operate. Reactions that pair mediators with thermal heterogeneous catalysts (i.e., not physically integrated with the electrode) can potentially operate by different pathways. One possibility involves direct chemical reaction between the substrate and mediator on the catalyst surface, while another involves formal "electrochemical" half-reactions that take place at different sites on a conductive catalyst surface. Studies to elucidate these catalytic mechanisms in mediated and non-mediated systems are an area of active study.[29-34] Further efforts to probe these questions will be crucial to improve performance of mediated systems and extend mediator accessibility to new applications. Potential applications are diverse, and mediators are well-suited to leverage electrochemical energy to drive chemical transformations with off-electrode catalyst systems, including molecular, heterogeneous, enzymatic, and microbial catalysts.

1.3 Anatomy of a Mediated Electrochemical Flow System

The following chapters will explore several electrochemical flow systems that utilize mediators as part of the operation of one or both half-cells. To facilitate comparison between each particular design, this section focuses on a discussion of the "anatomy" of such systems, giving attention to the general components they share. **Figure 1.2** depicts a fully general schematic that represents the approach taken when designing these cells. No one system will include all of these components, but each component is represented at least once in the actual designs. The purpose and function of these sub-systems can be elaborated upon further.

Every design discussed in this dissertation will have anodic and cathodic half-cells separated by a semi-permeable cation-exchange membrane. Reactions take place in a recirculation mode, with reagents moving through a flow path (parallel plate, serpentine, or interdigitated), undergoing partial conversion at the electrode, and then flowing out. We derive inspiration from the traditional fuel cell, and so hydrogen oxidation is the net anodic process in each system, sometimes used directly on-electrode and sometimes in a mediated process. For our power-generating cells, we also use oxygen reduction as the net cathodic process, although the final iterations of these systems are always mediated. Our electrosynthetic cell showcases cathodic cross-electrophile coupling as a high-value electrochemical reduction of interest. In each of these systems, the membrane serves to maintain charge balance between the half-cells while retaining species that do not have the appropriate charge to pass. Note that, unlike in traditional fuel cell systems, not all of the systems described will make use of protons as the primary trans-membrane charge carrier.

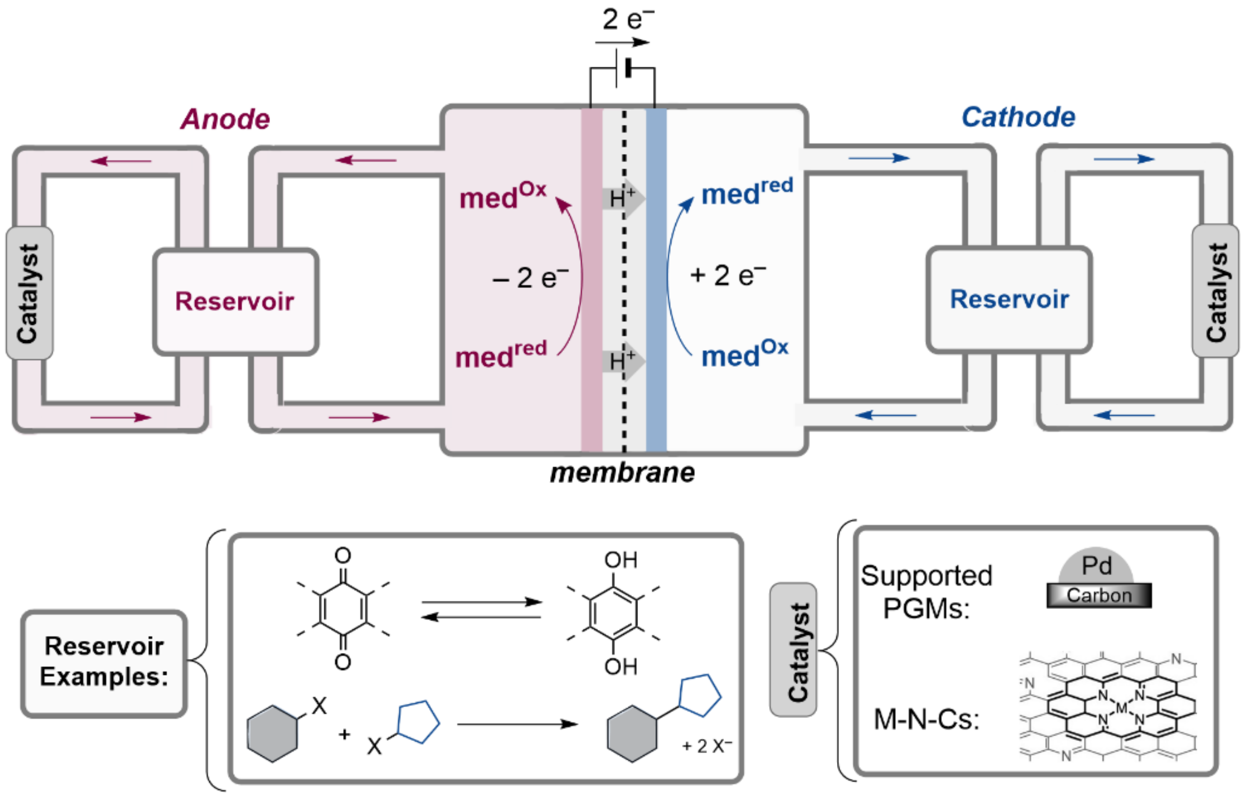

Figure 1.2: A generalized schematic of a mediated electrochemical flow system. Some subset of the depicted components will be present in each actualized system discussed in subsequent chapters. Conceptually, the system is composed of two half-cells separated by a semi-permeable membrane. Each

half-cell drives an electrochemical reaction, which may be a mediator rather than the terminal reagent. The system may also include a reservoir in which reaction components mix and/or a separate flow loop in which the terminal reagent reacts to regenerate the mediator.

In half-cell configurations that involve recirculating solutions, the solution then leaves the electrochemical cell and is returned to a reservoir to allow for mixing and participation in other processes. This reservoir can act as a batch reactor in which electrochemically activated species undergo relatively slow chemical reactions, or it can simply allow for homogenization of multiple feed streams. In half-cells that contain a separate catalytic loop for the reaction of substrate and mediator, solution is also pumped into and out of the reservoir through that loop. The catalytic loops in these systems make use of packed beds (cf. **Appendix 1**), wherein the heterogeneous catalyst may be a precious metal such as supported Pd nanoparticles or may be a non-precious metal catalyst in the M-N-C family of materials, discussed in more detail in **Chapter 4**.

This thread of commonality between these configurations belies the complexity of tuning electrochemical flow systems for various applications. One major goal of the subsequent chapters is to illustrate how relatively modest differences in intended use (e.g. oxidizing hydrogen to produce power vs oxidizing hydrogen to apply driving force to a synthetic reaction) will lead to very different practical considerations and therefore substantially different final system configurations.

References

---

1. Tegmark, M. *Life 3.0*; Penguin Books, 2018.

2. Noack, J.; Roznyatovskaya, N.; Herr, T.; Fischer, P., The Chemistry of Redox-Flow Batteries. *Angewandte Chemie International Edition* **2015,** *54* (34), 9776-9809.

3. Bates, J. S.; Biswas, S.; Suh, S.-E.; Johnson, M. R.; Mondal, B.; Root, T. W.; Stahl, S. S., Chemical and Electrochemical O2 Reduction on Earth-Abundant M-N-C Catalysts and Implications for Mediated Electrolysis. *Journal of the American Chemical Society* **2022,** *144* (2), 922-927.

4. Anson, C. W.; Stahl, S. S., Mediated Fuel Cells: Soluble Redox Mediators and Their Applications to Electrochemical Reduction of O2 and Oxidation of H2, Alcohols, Biomass, and Complex Fuels. *Chem. Rev.* **2020,** *120* (8), 3749-3786.

5. Tolmachev, Y. V.; Vorotyntsev, M. A., Fuel cells with chemically regenerative redox cathodes (review). *Russian Journal of Electrochemistry* **2014,** *50* (5), 403-411.

6. Bergens, S. H.; Gorman, C. B.; Palmore, G. T.; Whitesides, G. M., A Redox Fuel Cell That Operates with Methane as Fuel at 120{degrees}C. *Science* **1994,** *265* (5177), 1418-20.

7. Liu, W.; Mu, W.; Deng, Y., High-Performance Liquid-Catalyst Fuel Cell for Direct Biomass-into-Electricity Conversion. *Angewandte Chemie International Edition* **2014,** *53* (49), 13558-13562.

8. Xu, F.; Li, H.; Liu, Y.; Jing, Q., Advanced redox flow fuel cell using ferric chloride as main catalyst for complete conversion from carbohydrates to electricity. *Scientific Reports* **2017,** *7* (1), 5142.

---

9. Gong, J.; Liu, W.; Du, X.; Liu, C.; Zhang, Z.; Sun, F.; Yang, L.; Xu, D.; Guo, H.; Deng, Y., Direct Conversion of Wheat Straw into Electricity with a Biomass Flow Fuel Cell Mediated by Two Redox Ion Pairs. *ChemSusChem* **2017,** *10* (3), 506-513.

10. Zu, X.; Sun, L.; Gong, J.; Liu, X.; Liu, Y.; Du, X.; Liu, W.; Chen, L.; Yi, G.; Zhang, W.; Lin, W.; Li, W.; Deng, Y., Ferric ion pair mediated biomass redox flow fuel cell and related chemical reaction kinetics study. *Chemical Engineering Journal* **2018,** *348*, 476-484.

11. Zhao, X.; Zhu, J. Y., Efficient Conversion of Lignin to Electricity Using a Novel Direct Biomass Fuel Cell Mediated by Polyoxometalates at Low Temperatures. *ChemSusChem* **2016,** *9* (2), 197-207.

12. Zhang, Z.; Liu, C.; Liu, W.; Cui, Y.; Du, X.; Xu, D.; Guo, H.; Deng, Y., Innovative design of coal utilization – A green pathway for direct conversion of coal to electricity through flow fuel cell technology. *Applied Energy* **2017,** *200*, 226-236.

13. Hertl, W.; Weetall, H. H., A photo-chemical electrical fuel cell: Part I. Alcohol fuels. *Bioelectrochemistry and Bioenergetics* **1985,** *14* (4), 357-366.

14. Hertl, W.; Weetall, H. H., A photo-chemical electrical fuel cell: Part II. Carbohydrate fuels. *Bioelectrochemistry and Bioenergetics* **1985,** *14* (4), 367-373.

15. Weetal, H. H.; Forsyth, B. D.; Hertl, W., A direct fuel cell for the production of electricity from lignin. *Biotechnology and Bioengineering* **1985,** *27* (7), 972-979.

16. Preger, Y.; Gerken, J. B.; Biswas, S.; Anson, C. W.; Johnson, M. R.; Root, T. W.; Stahl, S. S., Quinone-Mediated Electrochemical O2 Reduction Accessing High Power Density with an Off-Electrode Co-N/C Catalyst. *Joule* **2018,** *2* (12), 2722-2731.

---

17. Preger, Y.; Johnson, M. R.; Biswas, S.; Anson, C. W.; Root, T. W.; Stahl, S. S., Anthraquinone-Mediated Fuel Cell Anode with an Off-Electrode Heterogeneous Catalyst Accessing High Power Density When Paired with a Mediated Cathode. *ACS Energy Letters* **2020,** *5* (5), 1407-1412.

18. Waldvogel, S. R.; Janza, B., Renaissance of Electrosynthetic Methods for the Construction of Complex Molecules. *Angewandte Chemie International Edition* **2014,** *53* (28), 7122-7123.

19 . Stergiou, A. D.; Symes, M. D., Organic transformations using electro-generated polyoxometalate redox mediators. *Catalysis Today* **2022,** *384-386*, 146-155.

20. Lian, F.; Xu, K.; Zeng, C., Indirect Electrosynthesis with Halogen Ions as Mediators. *The Chemical Record* **2021,** *21* (9), 2290-2305.

21. Francke, R.; Little, R. D., Redox catalysis in organic electrosynthesis: basic principles and recent developments. *Chemical Society Reviews* **2014,** *43* (8), 2492-2521.

22. Nutting, J. E.; Rafiee, M.; Stahl, S. S., Tetramethylpiperidine N-Oxyl (TEMPO), Phthalimide N-Oxyl (PINO), and Related N-Oxyl Species: Electrochemical Properties and Their Use in Electrocatalytic Reactions. *Chemical Reviews* **2018,** *118* (9), 4834-4885.

23. Murray, A. T.; Voskian, S.; Schreier, M.; Hatton, T. A.; Surendranath, Y., Electrosynthesis of Hydrogen Peroxide by Phase-Transfer Catalysis. *Joule* **2019,** *3* (12), 2942-2954.

24. Wang, W.; Luo, Q.; Li, B.; Wei, X.; Li, L.; Yang, Z., Recent Progress in Redox Flow Battery Research and Development. *Advanced Functional Materials* **2013,** *23* (8), 970-986.

25. Li, Z.; Lu, Y.-C., Material Design of Aqueous Redox Flow Batteries: Fundamental Challenges and Mitigation Strategies. *Advanced Materials* **2020,** *32* (47), 2002132.

---

26. Gerken, J. B.; Stamoulis, A.; Suh, S.-E.; Fischer, N. D.; Kim, Y. J.; Guzei, I. A.; Stahl, S. S., Efficient electrochemical synthesis of robust, densely functionalized water soluble quinones. *Chemical Communications* **2020,** *56* (8), 1199-1202.

27. Feng, R.; Zhang, X.; Murugesan, V.; Hollas, A.; Chen, Y.; Shao, Y.; Walter, E.; Wellala, N. P. N.; Yan, L.; Rosso, K. M.; Wang, W., Reversible ketone hydrogenation and dehydrogenation for aqueous organic redox flow batteries. *Science* **2021,** *372* (6544), 836-840.

28. Hu, S.; Wang, L.; Yuan, X.; Xiang, Z.; Huang, M.; Luo, P.; Liu, Y.; Fu, Z.; Liang, Z., Viologen-Decorated TEMPO for Neutral Aqueous Organic Redox Flow Batteries. *Energy Material Advances* **2021,** *2021*, 9795237.

29. Bates, J. S.; Biswas, S.; Suh, S.-E.; Johnson, M. R.; Mondal, B.; Root, T. W.; Stahl, S. S., Chemical and Electrochemical O2 Reduction on Earth-Abundant M-N-C Catalysts and Implications for Mediated Electrolysis. *Journal of the American Chemical Society* **2022,** *144* (2), 922-927.

30. Ryu, J.; Bregante, D. T.; Howland, W. C.; Bisbey, R. P.; Kaminsky, C. J.; Surendranath, Y., Thermochemical aerobic oxidation catalysis in water can be analysed as two coupled electrochemical half-reactions. *Nature Catalysis* **2021,** *4* (9), 742-752.

31. Adams, J. S.; Chemburkar, A.; Priyadarshini, P.; Ricciardulli, T.; Lu, Y.; Maliekkal, V.; Sampath, A.; Winikoff, S.; Karim, A. M.; Neurock, M.; Flaherty, D. W., Solvent molecules form surface redox mediators in situ and cocatalyze O2 reduction on Pd. *Science* **2021,** *371* (6529), 626-632.

---

32. Adams, J. S.; Kromer, M. L.; Rodríguez-López, J.; Flaherty, D. W., Unifying Concepts in Electro- and Thermocatalysis toward Hydrogen Peroxide Production. *Journal of the American Chemical Society* **2021,** *143* (21), 7940-7957.

33. Howland, W. C.; Gerken, J. B.; Stahl, S. S.; Surendranath, Y., Thermal Hydroquinone Oxidation on Co/N-doped Carbon Proceeds by a Band-Mediated Electrochemical Mechanism. *Journal of the American Chemical Society* **2022,** *144* (25), 11253-11262.

34. Huang, X.; Akdim, O.; Douthwaite, M.; Wang, K.; Zhao, L.; Lewis, R. J.; Pattisson, S.; Daniel, I. T.; Miedziak, P. J.; Shaw, G.; Morgan, D. J.; Althahban, S. M.; Davies, T. E.; He, Q.; Wang, F.; Fu, J.; Bethell, D.; McIntosh, S.; Kiely, C. J.; Hutchings, G. J., Au–Pd separation enhances bimetallic catalysis of alcohol oxidation. *Nature* **2022,** *603* (7900), 271-275.

Chapter 2

Mediated Fuel Cells Using Substituted Quinones for Indirect Anodic or Cathodic Reactivity

Note: The content in this chapter has been published. A credit statement is provided below to clarify this author's contributions.

Section 2.1:

This section is provided primarily for context. Johnson assisted Preger in the assembly of the fully constituted mediated fuel cell, in the collection of the benchmarking data in **Figure 2.4**, and in the "on-off" experiments in **Figure 2.6**. As a young graduate student, his contributions to this work (while meritorious) did not constitute intellectual leadership. Johnson made minor contributions to the text of the manuscript.

Preger, Y.; Gerken, J. B.; Biswas, S.; Anson, C. W.; Johnson, M. R.; Root, T. W.; Stahl, S. S., Quinone-Mediated Electrochemical O2 Reduction Accessing High Power Density with an Off-Electrode Co-N/C Catalyst. *Joule* 2018, *2* (12), 2722-2731.

Section 2.2:

Johnson began work on this project after its conception and initial troubleshooting. His contributions here included much of the work done with the article's final fuel cell iteration. Johnson and Preger assembled the fully constituted, doubly mediated fuel cell. Jointly, Johnson and Preger conducted polarization and power curve analysis. Johnson optimized the system to allow for the stability assay. Johnson conducted the experiments to demonstrate mediator stability in the fully constituted system. Johnson participated in, but did not take leadership of, the writing of the manuscript.

Preger, Y.; Johnson, M. R.; Biswas, S.; Anson, C. W.; Root, T. W.; Stahl, S. S., Anthraquinone-Mediated Fuel Cell Anode with an Off-Electrode Heterogeneous Catalyst Accessing High Power Density When Paired with a Mediated Cathode. *ACS Energy Letters* **2020,** *5* (5), 1407-1412.

2.1 A Mediated ORR Fuel Cell Cathode Enabled by a Highly Substituted Quinone

Abstract

New methods for interconversion of electrical and chemical energy are crucial to address emerging challenges in renewable energy storage and conversion. Dissolved redox mediators provide an effective means to transport electrons (and protons) between an electrode and catalysts that are not in direct physical contact with an electrode. Mediators are widely implemented in biofuel cells, but such devices typically exhibit low power densities. Here, we report the development of a tetrasubstituted quinone mediator that exhibits excellent stability under strongly acidic conditions and supports electrochemical reduction of O_2 at an off-electrode heterogeneous cobalt catalyst contained within a packed-bed reactor. Efficient oxidation of the hydroquinone by O_2 in the reactor provides the basis for mediator regeneration, and an integrated "flow cathode" fuel-cell system supports high power densities. These results establish the combination of organic mediators with off-electrode heterogeneous catalysts as a versatile platform for development of new electrode-driven chemical redox transformations.

Introduction

The electron-transport chain in cellular respiration uses the thermodynamic driving force of NADH oxidation by O_2 to generate an electrochemical proton gradient across the mitochondrial membrane. The overall process features a sequence of redox reactions catalyzed by membrane-bound enzymes, with ubiquinone and cytochrome *c* playing important roles as diffusible redox mediators to transport electrons and protons between the enzymes in the chain (**Figure 2.1 A**). Here, we demonstrate that analogous principles of quinone-mediated catalytic reduction of O_2 can provide the basis for a fuel cell capable of generating high power density. This system is enabled

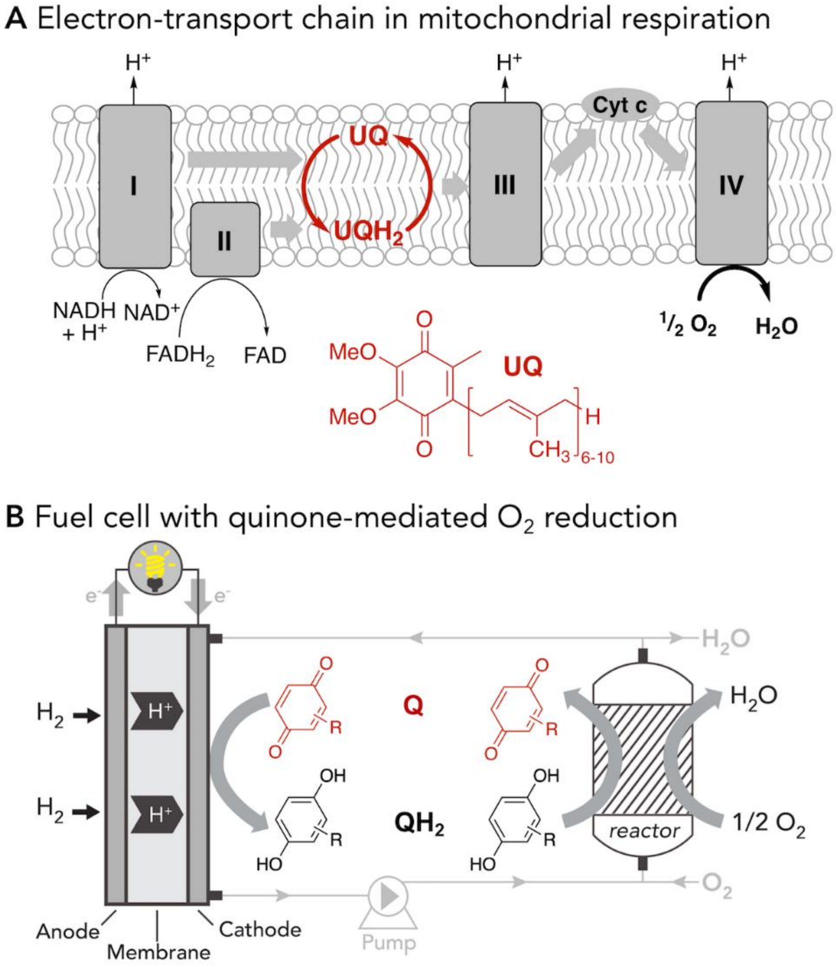

Figure 2.1: Quinone-mediated electron-proton transport for O_2 reduction**.** A. Electron-transport chain in mitochondrial respiration. Structures **I**–**IV** consist of membrane-bound enzymes that catalyze redox reactions. B. Flow-cathode design involving quinone-mediated electrocatalytic O_2 reduction with an off-electrode heterogeneous catalyst in a packed-bed reactor.

by (1) design and synthesis of a quinone mediator that exhibits good solubility and stability under acidic aqueous conditions, (2) identification of a heterogeneous cobalt-based catalyst that supports efficient aerobic oxidation of the corresponding hydroquinone under the acidic conditions, and (3) integration of a packed-bed flow reactor containing the off-electrode catalyst with a membrane-electrode assembly, allowing for sustained fuel cell operation (**Figure 2.1 B**). This flow-cathode design supports high current and power densities when combined with a conventional hydrogen anode in a fuel cell. These results establish a versatile concept for electrode-driven redox transformations, with opportunities that extend well beyond the mediated O_2 reduction process elaborated herein.

Quinones are appealing redox mediators because their modular structure allows their redox potentials to be tuned by > 1 V.[1,2] They have been widely used as mediators to support diverse redox processes, ranging from homogeneous catalytic aerobic oxidation reactions for organic synthesis[3] to electrochemical methods for energy storage[4-14] and conversion.[15-18] Mediated electrolysis is commonly featured in biofuel cells, where quinones or other organic mediators shuttle electrons (and protons) between the electrode and an enzyme or microbe.[16-18] The power density associated with these systems tends be quite low (often ≤ 2 mW/cm^2), however, owing to constraints associated with conditions needed to support the biological catalysts. Redox flow batteries (RFBs) represent another prominent application of redox mediators and are the focus of growing attention for reversible energy storage. While conventional mediators for aqueous RFBs are composed of inorganic materials ($Fe^{3+/2+}$, $V^{5+/4+}$, Br_2/Br^-, polyoxometalates),[4,5] recent advances highlight the ability of water soluble quinones to serve as effective mediators using the 2 e^-/2 H^+ quinone/hydroquinone redox couple.[9-12,15] The good solubility and electrochemical kinetics of sulfonated quinones have allowed for power densities of > 1 W/cm^2 in devices of this type.[10] These results prompted us to consider whether a high-power mediated fuel cell could be attained by combining a quinone-based mediator with a catalyst capable of promoting aerobic oxidation of hydroquinones (**Figure 2.1 B**).

Results and Discussion

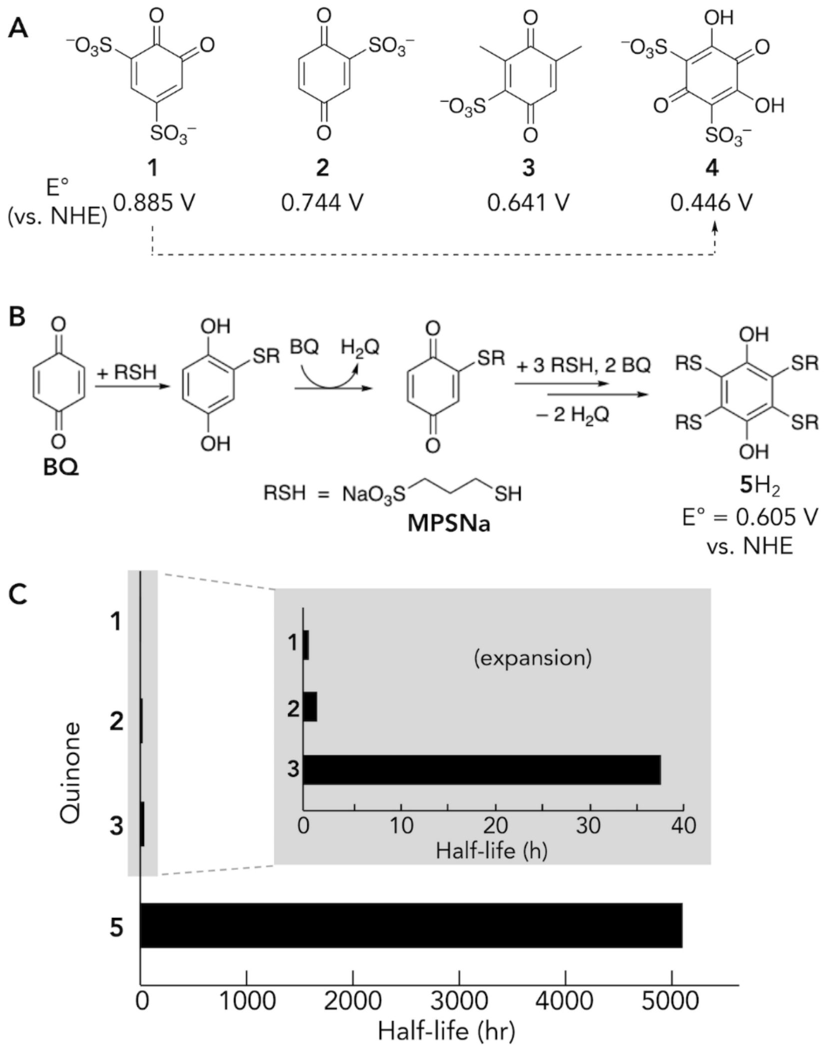

Figure 2.2: Development of quinone cathode mediator. A. Previously reported sulfonated quinones. B. Synthesis of a fully substituted hydroquinone mediator, compound **5**H_2. C. Mediator stability/half-life experiments.

The water-soluble quinones **1**–**3** (**Figure 2.2 A**) have been demonstrated previously as cathodic mediators,[8,11,12,15] and they provided a natural starting point for the present effort. Relatively few heterogeneous catalysts have been reported for aerobic oxidation of hydroquinones, and the majority of examples feature noble-metal catalysts and are used in organic solvents.[19] Building on these precedents, our initial tests evaluated aerobic oxidation of hydroquinone **2**H_2 in 1 M H_2SO_4 with a commercially available Pt/C (10 wt%) catalyst. Facile oxidation of **2**H_2 to **2** was observed under mild conditions (1 atm O_2, room temperature, 1–2 h), but significant decomposition of the mediator was evident during the reaction. Subsequent tests showed that all three quinones **1–3** are unstable in 1 M H_2SO_4, even in the absence of catalyst. Various quinone decomposition pathways have been noted in the literature.[7] For example, quinone **1** converts to the hydroxylated derivative **4** via sequential water-addition/oxidation steps,[11] and the byproduct **4** has a 2 e^-/2 H^+ reduction potential > 400 mV lower than that of **1** (446 mV vs. 885 mV, respectively). In other cases, hydroquinones undergo nucleophilic addition to quinones, leading to dimerization, oligomerization, and, eventually, tar formation.[20] This decomposition pathway seems to occur with quinone **2**.

We reasoned that introduction of substituents on all four positions of a benzoquinone could prevent the decomposition pathways evident with **1**–**3**. No precedents existed, however, for fully substituted high-potential quinones that exhibit good aqueous solubility (>100 mM). To access such structures, we took advantage of the nucleophilicity of thiols and their facile addition to quinones[21] to prepare the tetra-thioether hydroquinone derivative **5**H_2 (**Figure 2.2 B**). The synthesis proceeds by addition of the sodium salt of 3-mercapto-1-propanesulfonate (MPSNa) to benzoquinone in water and ethanol, followed by a sequence of three oxidation/thiol-addition steps, as shown in **Figure 2.2 B**. The stability of **5** was then compared to quinones **1**–**3** by dissolving each compound in acidic aqueous solution at 60 °C (0.1 M quinone in 0.5 M D_2SO_4/D_2O) and monitoring their fate by ^1H NMR spectroscopy. The data in **Figure 2.2 C** show that quinone **5** is dramatically more stable than the other quinone derivatives, exhibiting a half-life of > 5000 h under these conditions. The similar redox potentials of **3** and **5** ($E_{1/2}$ = 641 and 605 mV, respectively, vs. NHE) indicate that the >2-order-of-magnitude increase in stability predominantly arises from complete substitution of quinone **5**, rather than electronic effects.

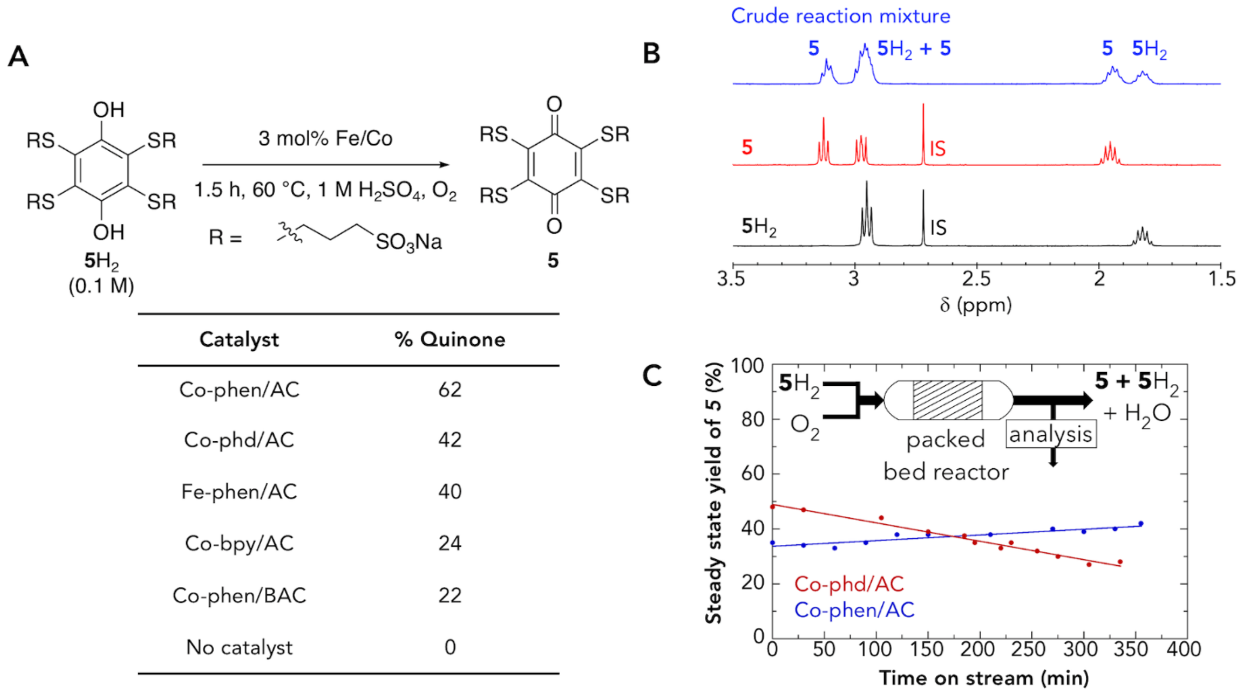

Catalyst	% Quinone
Co-phen/AC	62
Co-phd/AC	42
Fe-phen/AC	40
Co-bpy/AC	24
Co-phen/BAC	22
No catalyst	0

Figure 2.3: Oxidation of compound **5**H_2 by heterogeneous catalysts. A. Batch oxidation of **5**H_2 by non-Pt heterogeneous catalysts. Conditions: 1 mL of 0.1 M **5**H_2 in 1 M H_2SO_4, catalyst (3 mol % as-synthesized Co/Fe), 60 °C, O_2, 1.5 h. Carbon sources used for screening: amorphous activated carbon (AC) and bead activated carbon (BAC). Nitrogen ligands used for screening: 1,10 phenanthroline (phen), 2,2′-bipyridine (bpy), and 1,10-phenanthroline-5,6-dione (phd). B. NMR spectra of **5**H_2, isolated **5**, and the crude reaction

mixture following oxidation by Co-phen/AC (IS = $MeSO_3H$ internal standard). C. Time on stream steady state yields for the oxidation of $\mathbf{5}H_2$ in a continuous flow process. Yields analyzed by ^{1}H NMR spectroscopy. Conditions: 0.1 M $\mathbf{5}H_2$ in 1 M H_2SO_4, flow rate: 0.25 mL/min, catalyst (250 mg catalyst), 50 °C, O_2 flow rate: 1.1 mL/min. Inset schematic showing the design of the experiment.

With access to a robust soluble quinone, we focused on identification of a non-precious-metal, heterogeneous catalyst that could promote aerobic oxidation of hydroquinone $\mathbf{5}H_2$ under strongly acidic conditions. No direct precedents existed for such catalytic reactivity, but our attention was drawn to a family of heterogeneous catalysts composed of nitrogen-doped carbon containing cobalt and iron (Co- and Fe-N/C), recently reported by Beller and coworkers for aerobic oxidation of alcohols.[22] Although the previous reactions were reported in organic solvents containing a Brønsted base, the catalyst compositions closely resemble Pt-free catalysts that have been used as electrocatalysts for O_2 reduction at both high and low pH.[23-25] A series of catalysts were prepared via wet-impregnation of a carbon support with a nitrogen-ligated Co or Fe complex [ligand = 1,10 phenanthroline (phen), 2,2′-bipyridine (bpy), and 1,10-phenanthroline-5,6-dione (phd)], followed by pyrolysis under N_2 at 800 °C. The catalysts are composed of a mixture of oxidic and metallic nanoparticles encapsulated by nitrogen rich carbon layers (see associated publication and ref. 22 for details). Each of the Co- and Fe-N/C catalysts prepared by this method exhibited activity for aerobic oxidation of $\mathbf{5}H_2$ under batch reaction conditions in 1 M H_2SO_4 (**Figure 2.3 A**). The tests were run to partial conversion to facilitate comparison of catalyst performance, and the highest activity was observed with a catalyst derived from $Co(OAc)_2$/phen deposited on an amorphous activated carbon (Co-phen/AC). Analysis of the crude reaction mixture from the Co-phen/AC-catalyzed reaction by NMR spectroscopy revealed very clean oxidation of the hydroquinone to the quinone, with no evidence of decomposition or side-product formation (**Figure 2.3 B**). The two best catalyst compositions, Co-phen/AC and Co-phd/AC, were then tested in a packed-bed reactor (1/4" o.d. stainless steel tubing) to probe their performance during continuous operation. The hydroquinone **5**H_2 was delivered into the reactor under conditions selected to achieve approximately 40% single-pass conversion, and the steady state yield of quinone **5** was monitored as function of time on stream to detect changes in catalyst performance (**Figure 2.3 C**). The Co-phen/AC catalyst showed stable performance, while the Co-phd/AC catalyst showed a decline in performance over the course of the reaction. On the basis of these batch and flow reaction data, the Co-phen/AC catalyst was selected for fuel cell testing.

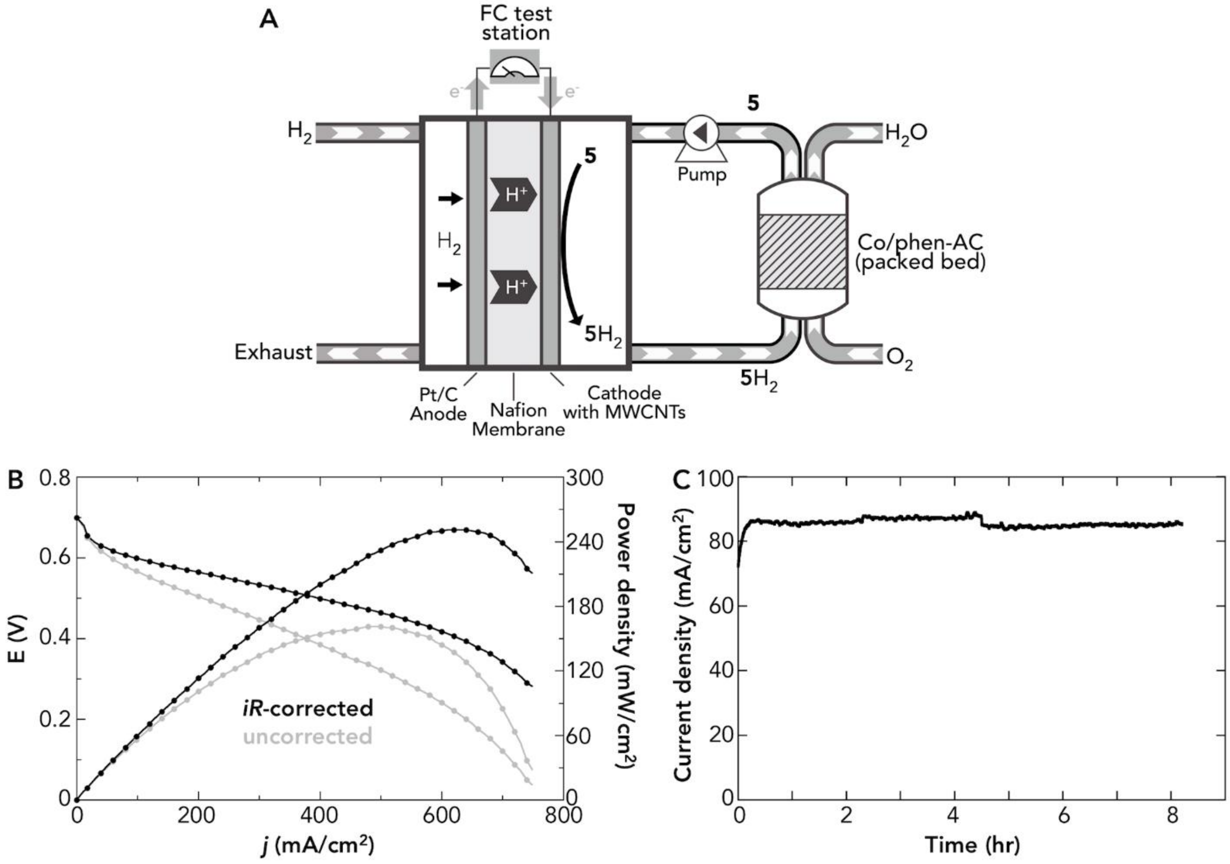

Figure 2.4: Operation of the integrated fuel cell with catalytic regeneration of the mediator. A. Design of fuel cell integrated with packed bed reactor. B. Polarization and power density curves with H_2 at the anode and 0.1 M **5** in 1 M H_2SO_4 at the cathode, with iR (gray) and iR-corrected (black). C**.** Constant potential experiment at 0.5 V with 0.1 M **5** in 1 M H_2SO_4.

To implement the Co-phen/AC catalyst system in a fuel cell, the packed-bed reactor containing the Co-phen/AC catalyst was connected via tubing to a pump and the cathode compartment of a 5 cm^2 membrane-electrode assembly, which featured a conventional H_2 anode with a Pt/C catalyst, a Nafion 117 membrane, and a carbon-paper cathode functionalized with multi-walled carbon nanotubes to facilitate quinone reduction (**Figure 2.4 A**, see this section's supplementary information for details).[26] A mediator solution composed of 0.1 M **5**H_2 in 1 M H_2SO_4 was passed through the catalyst bed in the reactor with 1 atm oxygen gas to charge the flow-cathode system with oxidized quinone. The fuel cell was then operated at 60 °C with the liquid mediator solution cycled through the cathode and reactor compartments, while H_2 was delivered to the anode at 0.2 L/min. A polarization curve was collected with the mediator solution containing a **5**:**5**H_2 ratio of 95:5 (i.e., a 95% state-of-charge). As shown in Figure 4B, the fuel cell exhibited a peak power density of 161 mW/cm^2, with an iR-corrected value of 251 mW/cm^2, when operating under these conditions. By matching the rates of electrochemical reduction of the quinone at the cathode with the rate of aerobic oxidation of hydroquinone in the packed bed reactor, it was possible to establish stable continuous operation (**Figure 2.4 C**). Inclusion of a small liquid reservoir between the cathode and packed-bed reactor compartments allows the liquid flow rates through the cathode and the reactor to be different, allowing for optimal performance in the individual units to be maintained while supporting system-wide stability. An initial mediator state-of-charge of approximately 60% was established prior to steady state operation, and this value was maintained throughout the experiment, as determined by in-line potentiometric analysis of the mediator solution. In a separate experiment, the balance between the rates of the two redox processes was tested and confirmed by interrupting the oxygen flow to the reactor over a period of 15 min (see **Figure 2.6** in this section's supplemental information).

These results represent the first combination of organic mediators with heterogeneous catalysts in mediated electrolysis, and they display approximately two orders-of-magnitude higher power density than that typically observed from the combination of organic mediators and biological catalysts in biofuel cells.[18] This performance improvement, in part, reflects the benefits arising from mediators and catalysts compatible with strongly acidic fuel cell conditions. The approach described here for mediated O_2 reduction also offers a compelling alternative to the use of inorganic mediators, such as Br_2, vanadyl ion, polyoxometalates (POMs), and NO_x species.[27] Flow cathode concepts employing POM-based mediators, in particular, have been the focus of considerable recent attention, including commercialization efforts, by ACAL Energy and others.[28-30] Rather than relying on a single component to conduct both electrochemical redox and catalytic reactivity with O_2 (as with POMs), the present approach presents an opportunity to tune and optimize the mediator and catalyst components independently. This feature should facilitate future improvements to system performance. Recent studies of electrochemical O_2 reduction with molecular catalysts also show that organic mediators, including hydroquinones, can improve catalytic performance through the onset of cooperative catalyst/mediator mechanistic pathways.[31,32] Analogous pathways should be accessible from combinations of organic mediators and heterogeneous catalysts.

The ability to tune the structure and molecular properties of organic mediators is already evident in the development of the tetrasubstituted quinone **5**. This new quinone exhibits excellent solubility (approximately 0.25 M as the tetrasodium salt and >1 M as the tetraacid at room temperature) and orders-of-magnitude improved stability relative to previously reported quinones. The stabilization imparted by tetrasubstitution of the quinone should have a major impact on the development of new mediators. A natural next step in this area will be the development of quinones with higher redox potentials, for example, by replacing one or more of the thioether groups in **5** with an electron-withdrawing group. These efforts will need to be paired with efforts to develop catalysts that enable efficient aerobic oxidation of mediators with redox potentials that approach the O_2/H_2O thermodynamic potential.

The present system does not yet match the performance metrics of current state-of-the-art fuel cells that contain Pt or non-platinum-group metal (non-PGM) electrocatalysts. The main performance limitation with the present flow-cathode system is the redox potential of the mediator, however, and preliminary modeling of fuel cell performance with higher-potential mediators suggests much higher power densities, approaching 1 W/cm^2, should be accessible (see associated publication for further discussion). Such performance, which has been achieved with flow batteries using organic mediators,[10] would surpass existing non-PGM cathode systems.[33, 34] Realization of such improvements will provide a basis for broader technoeconomic analysis of this non-traditional fuel cell system to consider how the benefits (e.g., improved energy efficiency and thermal and water management) offset additional costs (e.g., the requirement for pumps, additional weight).

Conclusion

Overall, new strategies such as the approach described here warrant attention in the effort to achieve efficient fuel cell performance with non-PGM catalysts. The present results also provide a foundation for diverse mediated electrolysis processes, with potential applications including CO_2 reduction, liquid fuel cells, and conversion of biomass-derived feedstocks.[35] Implementation of a heterogeneous catalyst in a packed-bed reactor leverages classical reaction engineering technology widely used in the chemical industry to achieve high kinetic and volumetric efficiencies. The ability to exploit such well-established technology should enable rapid expansion of the scope and utility of electrode-driven redox transformations.

Supplemental Information

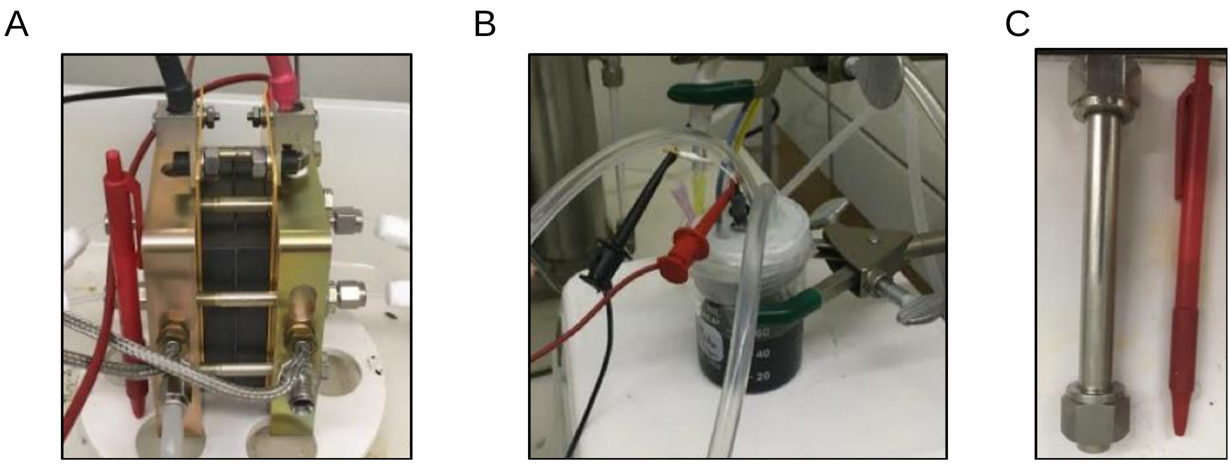

Figure 2.5: Photos of major components of integrated reactor-fuel cell. A**.** Fuel cell with 5 cm^2 membrane-electrode assembly. B. Reservoir with glassy carbon working electrode and Ag/AgCl reference electrode. C. Packed bed reactor.

Full Cell Assembly and Operation. The 5 cm^2 membrane-electrode assembly (MEA) consisted of a Nafion117 membrane with a 0.5 mg Pt/cm^2 conventional H_2 anode (purchased from the Fuel

Cell Store) and two pieces of Sigracell 29AA carbon paper for the cathode. The carbon paper was functionalized with MWCNTs by sonicating the paper for several minutes in an ethanol solution containing the nanotubes. The MEA was enclosed by two PTFE gaskets, graphite blocks with interdigitated flow channels (channel width = 0.032 in, channel depth = 0.039 in, lands between channels = 0.03 in), current collectors (gold-plated copper plates), and aluminum heating blocks. All of the fuel cell hardware except the graphite blocks was supplied by Fuel Cell Technologies. The flow blocks were machined from 0.5 in. thick impervious, resin-impregnated bipolar graphite plates (Graphite Store) to minimize fluid absorption. The cell temperature was monitored via a thermocouple inserted in an aluminum block and maintained by cartridge heaters inserted in both aluminum blocks. Fluid was circulated through the fuel cell cathode compartment using a Cole-Palmer peristaltic pump and Masterflex Tygon E-LFL tubing. 1/8 in. PTFE tubing passing through the heating blocks to the flow plates prevented fluid/metal contact. During operation, the cell was heated to 60 °C and H_2 flowed through the anode at 0.2 L/min without humidification, given the ample water available at the cathode.

A reservoir with 60 mL of 0.1 M **5**H_2 in 1 M H_2SO_4 was placed between the cathode and the reactor to serve as a buffer for slight mismatches in their rates and to enable operation at different flow rates (50-100 mL/min for the fuel cell to minimize mass transfer losses and up to 30 mL/min for the reactor to minimize pressure drop through the catalyst bed; total mediator solution volume = reservoir + reactor volume = 80 mL). A Cole-Palmer peristaltic pump circulated the contents of the reservoir through a packed bed reactor in co-current upflow with O_2 (controlled by a Teledyne Hastings mass flow controller). The packed-bed reactor and a pre-heating zone were wrapped in heating tape and the temperature was maintained at 50 °C based on a built-in thermocouple touching the reactor wall. After reacting over the catalyst, the electrolyte was returned to the reservoir. To monitor the extent of mediator oxidation, a working electrode (glassy carbon) and a reference electrode (Ag/AgCl) were placed in the reservoir. The electrodes were connected to a multimeter and the measured potential converted to a **5**:**5**H_2 ratio according to the Nernst equation.

The packed-bed reactor was made from a 6.25 in. length of 0.5 in. o.d. (3/8 in. i.d.) stainless steel tube with 7/8 in. of glass wool inside a Swagelok fitting. Co-phen/AC (~5 g) was added, leaving 1 in of open space for more glass wool to be retained by another Swagelok fitting.

Polarization curves were collected with the assembly described above. The solution (0.1 M **5** in 1 M H_2SO_4) in the reservoir was circulated through the packed-bed reactor at a flow rate of 15 mL/min with 10 mL/min of O_2 until the reservoir state-of-charge was ~95 %. After the fuel cell was heated to 60 °C, polarization curves were collected with H_2 flowing at 0.2 L/min and the catholyte circulating at 100 mL/min. iR-corrected data was based on the fuel cell high frequency resistance measurement.

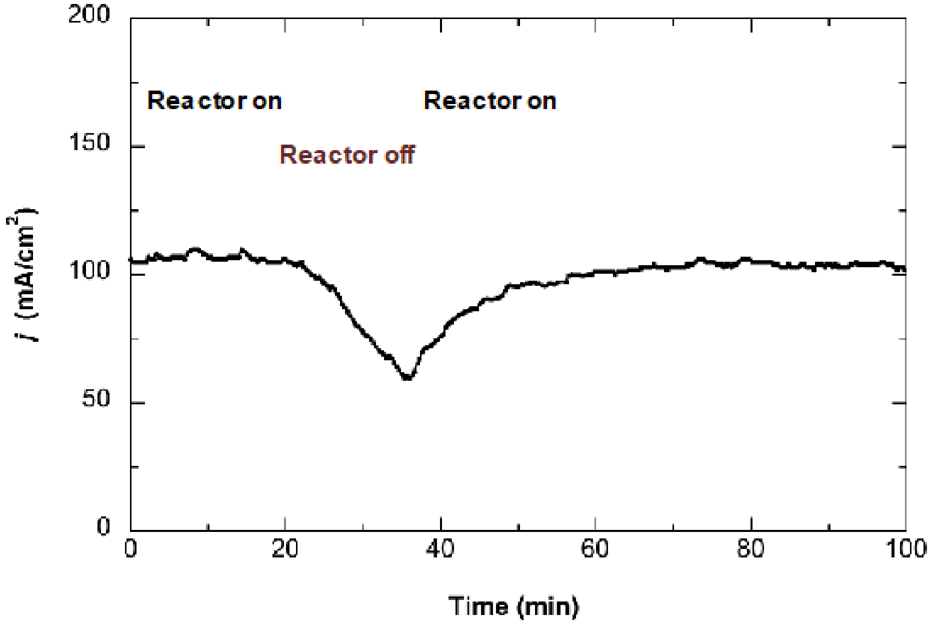

Figure 2.6: Operation of fuel cell integrated with mediator regenerator. Constant potential experiment at 0.5 V with 0.1 M **5** in 1 M H_2SO_4. O_2 flow to the reactor turned off at t = 20 min and back on at t = 36 min.

References

---

1. Er, S., Suh, C., Marshak, M. P., and Aspuru-Guzik, A. (2015). Computational design of molecules for an all-quinone redox flow battery. Chem. Sci. *6*, 885-893.

2. Huynh, M. T., Anson, C. W., Cavell, A. C., Stahl, S. S., and Hammes-Schiffer, S. (2016). Quinone 1 e- and 2 e-/2 H+ reduction potentials: identification and analysis of deviations from systematic Scaling relationships. J. Am. Chem. Soc. *138*, 15903-15910.

3. Piera, J. and Bäckvall, J.-E. (2008). Catalytic oxidation of organic substrates by molecular oxygen and hydrogen peroxide by multistep electron transfer – a biomimetic approach. Angew. Chem. Int. Ed. *47*, 3506-3523.

4. Soloveichik, G. L. (2015). Flow batteries: current status and trends. Chem. Rev. *115*, 11533-11558.

5. Winsberg, J., Hagemann, T., Janoschka, T., Hager, M. D., and Schubert, U. S. (2017). Redox-flow batteries: from metals to organic redox-active materials. Angew. Chem. Int. Ed. *56*, 686-711.

6. Wei, X., Pan, W., Duan, W., Hollas, A., Yang, Z., Li, B., Nie, Z., Liu, J., Reed, D., Wang, W., and Sprenkle, V. (2017). Materials and systems for organic redox flow batteries: status and challenges. ACS Energy Lett. *2*, 2187-2204.

7. Wedege, K., Dražević, E., Konya, D., and Bentien, A. (2016). Organic redox species in aqueous flow batteries: redox potentials, chemical stability and solubility. Sci. Rep. *6*, 39101.

8. Rausch, B., Symes, M. D., and Cronin, L. (2013). A bio-inspired, small molecule electron-coupled-proton buffer for decoupling the half-reactions of electrolytic water splitting. J. Am. Chem. Soc. *135*, 13656-13659.

---

9. Huskinson, B., Marshak, M. P., Suh, C., Er, S., Gerhardt, M. R., Galvin, C. J., Chen, X., Aspuru-Guzik, A., Gordon, R. G., and Aziz, M. J. (2014). A metal-free organic-inorganic aqueous flow battery. Nature *505*, 195-198.

10. Chen, Q., Gerhardt, M. R., Hartle, L., and Aziz, M. J. (2016). A quinone-bromide flow battery with 1 W/cm2 power density. J. Electrochem. Soc. *163*, A5010-A5013.

11. Yang, B., Hoober-Burkhardt, L., Krishnamoorthy, S., Murali, A., Prakash, G. K. S., and Narayanan, S. R. (2016). High-performance aqueous organic flow battery with quinone-based redox couples at both electrodes. J. Electrochem. Soc. *163*, A1442 - A1449.

12. Hoober-Burkhardt, L., Krishnamoorthy, S., Yang, B., Murali, A., Nirmalchandar, A., Prakash, G. K. S., and Narayanan, S. R. (2017). A new Michael-reaction-resistant benzoquinone for aqueous organic redox flow batteries. J. Electrochem. Soc. *164*, A600 - A607.

13. Son, E. J., Kim, J. H., Kim, K., and Park, C. B. (2016). Quinone and its derivatives for energy harvesting and storage materials. J. Mater. Chem. A *4*, 11179-11202.

14. Zhu, Y. G., Wang, X., Jia, C., Yang, J., and Wang, Q. (2016). Redox-Mediated ORR and OER Reactions: Redox Flow Lithium Oxygen Batteries Enabled with a Pair of Soluble Redox Catalysts. ACS Catal. *6*, 6191-6197.

15. Li, W., Fu, H.-C., Li, L., Cabán-Acevedo, M., He, J.-H., and Jin, S. (2016). Integrated photoelectrochemical solar energy conversion and organic redox flow battery devices. Angew. Chem. Int. Ed. *55*, 13104-13108.

16. Kavanagh, P. and Leech, D. (2013). Mediated electron transfer in glucose oxidising enzyme electrodes for application to biofuel cells: recent progress and perspectives. Phys. Chem. Chem. Phys. *15*, 4859-4869.

---

17. Milton, R. D., Hickey, D. P., Abdellaoui, S., Lim, K., Wu, F., Tan, B., and Minteer, S. D. (2015). Rational design of quinones for high power density biofuel cells. Chem. Sci. *6*, 4867-4875.

18. Mano, N. and de Poulpiquet, A. (2018). O2 reduction in enzymatic biofuel cells. Chem. Rev. *118*, 2392-2468.

19. Miyamura, H., Shiramizu, M., Matsubara, R., and Kobayashi, S. (2008). Aerobic oxidation of hydroquinone derivatives catalyzed by polymer-incarcerated platinum catalyst. Angew. Chem. Int. Ed. *47*, 8093-8095.

20 . Erdtman, H. and Hogberg, H.-E. (1979). The acid-catalysed oligomerisation of *p*-benzoquinone. Tetrahedron *35*, 535-540.

21. Vadnere, M. K., Maggiora, L., and Mertes, M. P. (1986). Thiol addition to quinones: model reactions for the inactivation of thymidylate synthase by 5-*p*-benzoquinonyl-2'-deoxyuridine 5'-phosphate. J. Med. Chem. *29*, 1714-1720.

22. He, L., Weniger, F., Neumann, H., and Beller, M. (2016). Synthesis, characterization, and application of metal nanoparticles supported on nitrogen-doped carbon: catalysis beyond electrochemistry. Angew. Chem. Int. Ed. *55*, 12582-12594.

23 . Wu, G., More, K. L., Johnston, C. M., and Zelenay, P. (2011). High-performance electrocatalysts for oxygen reduction derived from polyaniline, iron, and cobalt. Science *332*, 443-447.

24 . Shao, M., Chang, Q., Dodelet, J.-P., and Chenitz, R. (2016). Recent advances in electrocatalysts for oxygen reduction reaction. Chem. Rev. *116*, 3594-3657.

25. Gewirth, A. A., Varnell, J. A., and DiAscro, A. M. (2018). Nonprecious metal catalysts for oxygen reduction in heterogeneous aqueous systems. Chem. Rev. *118*, 2313-2339.

---

26. Qi, H. and Zhang, C. (2005). Simultaneous determination of hydroquinone and catechol at a glassy carbon electrode modified with multiwall carbon nanotubes. Electroanalysis *17*, 832-838.

27. Tolmachev, Y. V. and Vorotyntsev, M. A. (2014). Fuel cells with chemically regenerative redox cathodes (review). Russ. J. Electrochem. *50*, 403-411.

28. Creeth, A. (2011) Pt-free PEM cathode technology with fundamental durability benefits: FlowCath®. Fuel Cells Bull. *2011*, 12-15.

29. Gunn, N. L. O., Ward, D. B., Menelaou, C., Herbert, M. A., and Davies, T. J. (2017). Investigation of a chemically regenerative redox cathode polymer electrolyte fuel cell using a phosphomolybdovanadate polyoxoanion catholyte. J. Power Sources *348*, 107-117.

30. Liu, W., Mu, W., and Deng, Y. (2014). High-Performance Liquid-Catalyst Fuel Cell for Direct Biomass-into-Electricity Conversion. Angew. Chem. Int. Ed. *53*, 13558-13562.

31. Gerken, J. B. and Stahl, S. S. (2015). High-potential electrocatalytic O2 reduction with nitroxyl/NOx mediators: implications for fuel cells and aerobic oxidation catalysis. ACS Cent. Sci. *1*, 234-243.

32. Anson, C. W. and Stahl, S. S. (2017). Cooperative electrocatalytic O2 reduction involving Co(salophen) with *p*-hydroquinone as an electron-proton transfer mediator. J. Am. Chem. Soc. *139*, 18472-18475.

33. Chung, H. T., Cullen, D. A., Higgins, D., Sneed, B. T., Holby, E. F., More, K. L., Zelenay, P. (2017). Direct atomic-level insight into the active sites of a high-performance PGM-free ORR catalyst. Science *357*, 479-484.

34. Wang, X. X., Cullen, D. A., Pan, Y.-T., Hwang, S., Wang, M., Feng, Z., Wang, J., Engelhard, M. H., Zhang, H., He, Y., Shao, Y., Su, D., More, K. L., Spendelow, J. S., Wu, G. (2018). Nitrogen-

Coordinated Single Cobalt Atom Catalysts for Oxygen Reduction in Proton Exchange Membrane Fuel Cells. Adv. Mater. *30*, 1706758.

35. Zhao, X., Liu, W., Deng, Y., and Zhu, J. Y. (2017). Low-temperature microbial and direct conversion of lignocellulosic biomass to electricity: Advances and challenges. Renew. Sust. Energ. Rev. *71*, 268-282.

2.2 An Anthraquinone-Mediated Fuel Cell Anode Paired with a Mediated Cathode Achieves High Power Densities.

Abstract

The development of processes for electrochemical energy conversion and chemical production could benefit from new strategies to interface chemical redox reactions with electrodes. Here, we employ a diffusible low-potential organic redox mediator, 9,10-anthraquinone-2,7-disulfonic acid (AQDS), to promote efficient electrochemical oxidation of H2 at an off-electrode heterogeneous catalyst. This unique approach to integrate chemical and electrochemical redox processes accesses power densities up to 228 mW/cm^2 (528 mW/cm^2 with iR-correction). These values are significantly higher than those observed in previous mediated electrochemical H_2 oxidation methods, including those using enzymes or inorganic mediators. The approach described herein shows how traditional catalytic chemistry can be coupled to electrochemical devices.

Introduction

Redox-active organic molecules have been widely employed as electrochemical mediators to enhance electron transfer between an electrode and a catalyst or chemical reagent in solution. Applications include electrochemical organic synthesis[1] and energy storage and conversion.[2] Enzymatic biofuel cells, for example, often use organic redox mediators to facilitate redox reactions with enzyme-based catalysts. Representative mediators include (anthra)quinones,[3] viologens,[4] and 2,2'-azino-bis(3-ethylbenzthiazoline-6-sulfonic acid (ABTS)[5] (**Figure 2.7 A**). Applications of these methods are typically limited to low-power applications, such as implantable biomedical devices and portable electronics,[6] because the conditions required to sustain enzyme activity and stability limit the fuel cell performance. Power densities accessed by enzymatic fuel cells are typically 2-3 orders of magnitude lower than those of conventional proton exchange

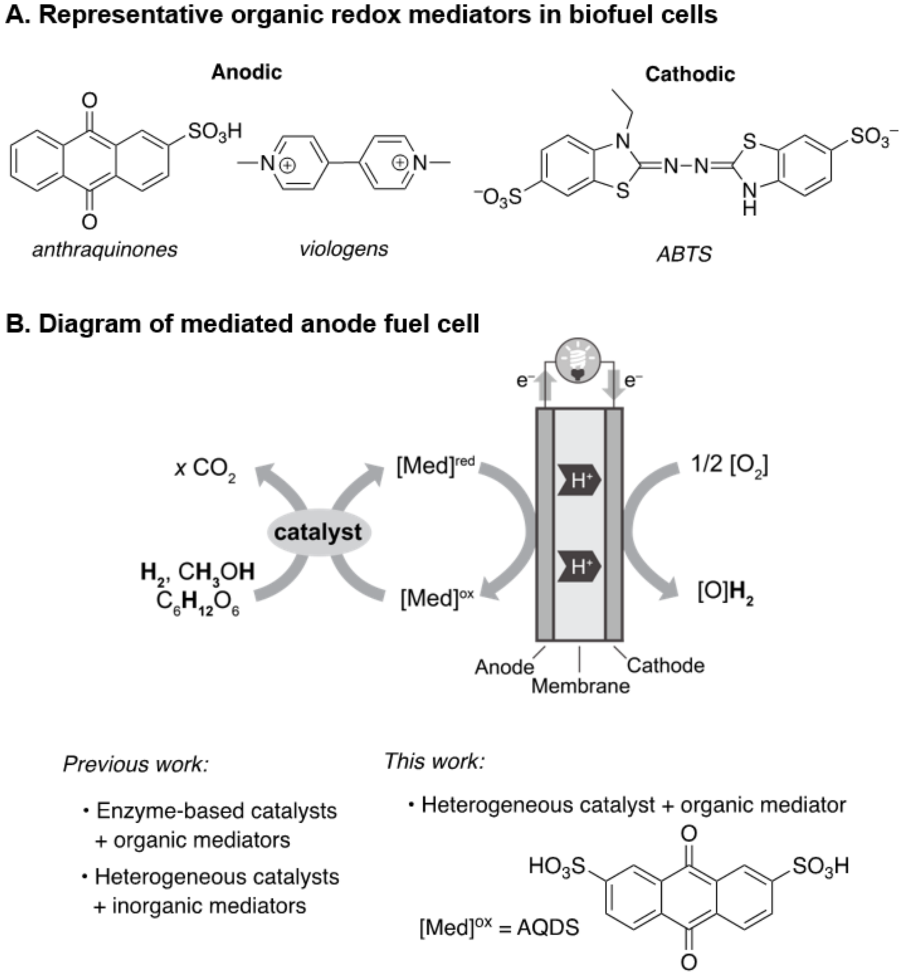

Figure 2.7: A. Organic redox mediators can play an important role in enzymatic fuel cells. B. They are also used in fuel cells with diverse catalysts.

membrane fuel cells (PEMFCs) (Figure **2.7 B**). Replacing the relatively fragile enzymes with heterogeneous catalysts capable of tolerating strongly acidic (or basic) fuel cell conditions and elevated temperatures provides a potential strategy to overcome this limitation. Here, we demonstrate this concept by employing 9,10-anthraquinone-2,7-disulfonic acid (AQDS) as a mediator for electrochemical oxidation of H_2 at an off-electrode Pt/C catalyst. iR-free power densities of > 500 mW/cm^2 are accessible when this anodic process is paired with a mediated cathode, employing a previously reported polyoxometalate-based mediator for O_2 reduction.[7] This system, which represents the first pairing of an organic mediator with an off-electrode heterogeneous catalyst in a fuel cell anode, leverages the strengths of both chemical and electrochemical redox reactions and establishes an important platform for development of new electrode-driven redox processes.

Organic mediators have been the focus of substantial recent attention for use in aqueous redox flow batteries (RFBs) and related energy-storage devices.[8,9] Quinones, aminoxyls, and other redox-active organic molecules complement the more widely used inorganic mediators, such as V, Fe, and Zn ions, in these devices.[2d] Aqueous RFBs with organic mediators have been shown to support high power densities (≥ 1 W/cm^2),[10] and anthraquinones are commonly featured anodic mediators in these applications.[11] Meanwhile, quinones have been widely used as reagents and catalytic mediators in chemical oxidation reactions,[12] and they undergo efficient catalytic oxidation[13] and reduction[14] over heterogeneous catalysts. A noteworthy example of the latter application is the "anthraquinone process" for industrial production of hydrogen peroxide, which features a two-stage sequence involving catalytic hydrogenation of an anthraquinone derivative followed by autoxidation of the corresponding anthrahydroquinone to generate H_2O_2 and the quinone derivative.[15] Collectively, these precedents provided an important foundation for the present study, which takes advantage of anthraquinones and heterogeneous catalysts to mediate the electrochemical reduction of H_2 in an off-electrode compartment.

Results and Discussion

AQDS was selected as a prototypical anode mediator owing to its good electrochemical behavior and the proximity of its redox potential to the thermodynamic H^+/H_2 potential. Both of these features are evident in the cyclic voltammogram of the disodium salt of AQDS ($AQDS\text{-}Na_2$), obtained in the 1 M sulfuric acid medium used in this study. The well-defined oxidation and reduction peaks and quasireversible redox potential of 220 mV vs. NHE (**Figure 2.8**) are consistent with previous reports.[11a]

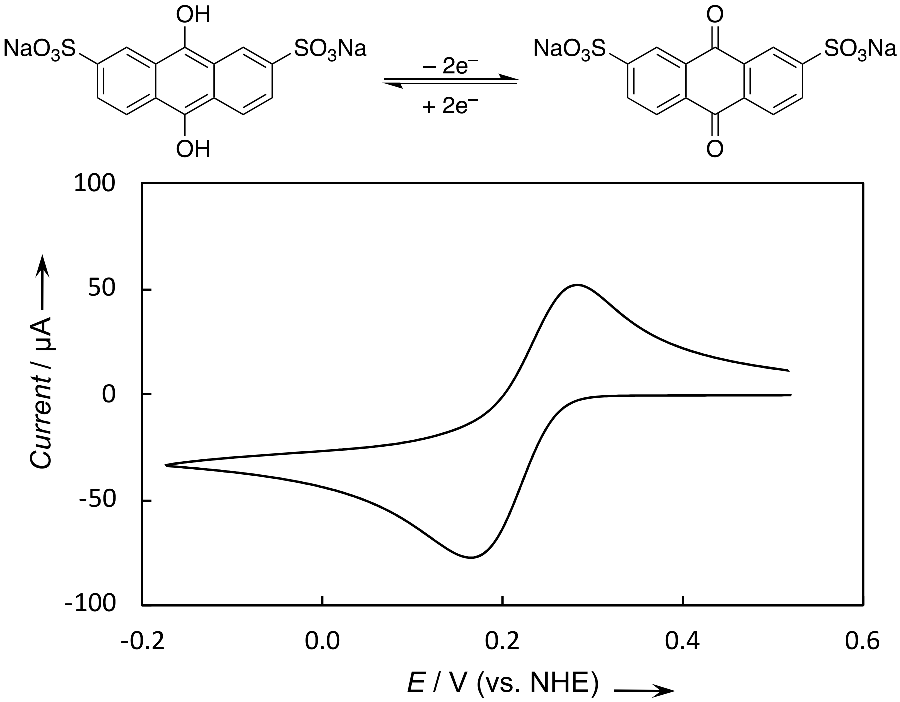

Figure 2.8: Cyclic voltammogram of 9,10-anthraquinone-2,7-disulfonic acid, disodium salt ($AQDS\text{-}Na_2$) in 1 M H_2SO_4. Conditions: $AQDS\text{-}Na_2$ (10 mM), glassy carbon working electrode, Pt-wire counter electrode, Ag/AgCl reference electrode; 10 mV s^{-1} scan rate.

The catalytic hydrogenation of anthraquinones has been extensively investigated in organic solvents or neutral aqueous media,[14] but such conditions are not conducive to fuel cell applications, which favor strongly acidic or basic aqueous conditions. Hydrogenation of quinones in acidic media has only been reported for the parent 1,4-benzoquinone, which has a potential ($E_{1/2}$ ~ 700 mV) more than 450 mV higher than that of AQDS.[14a] Nonetheless, this precedent employing a supported Pt catalyst prompted us to select a commercial Pt/C catalyst, sourced from Strem Chemicals, for our initial testing of AQDS-Na_2 hydrogenation in 1 M sulfuric acid. Monitoring of the hydrogenation of AQDS is complicated by the air sensitivity of AQDSH_2 (9,10-anthrahydroquinone-2,7-disulfonic acid), arising from its facile autoxidation to regenerate AQDS.

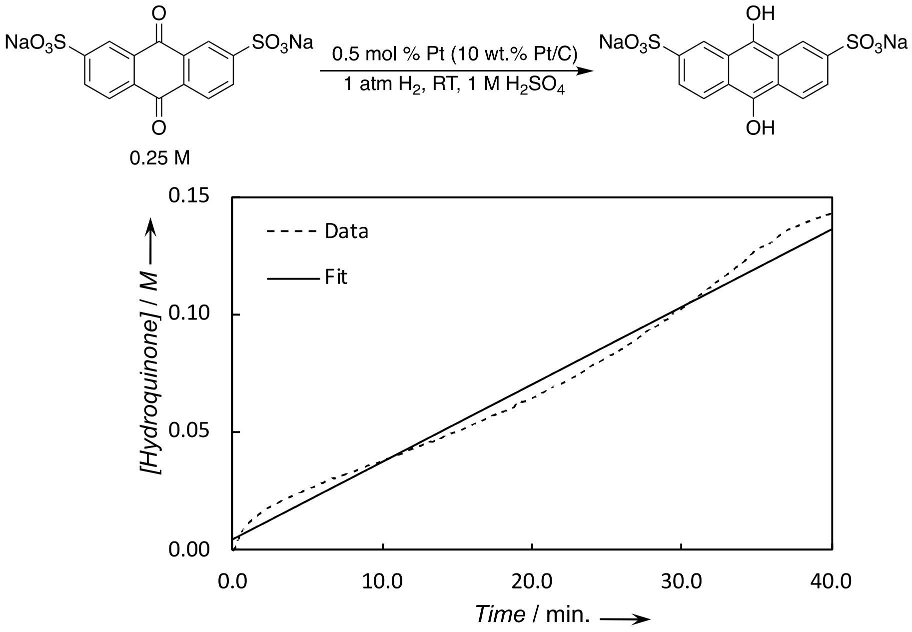

Figure 2.9: Reaction progress for batch hydrogenation of 9,10-anthraquinone-2,7-disulfonic acid, disodium salt catalyzed by Pt/C. Formation of hydroquinone was monitored via potentiometry. Dots are reaction data and the line reflects a linear correlation to the data.

To address this issue, the reaction progress was monitored in a sealed vessel via potentiometric analysis of the batch reaction mixture (**Figure 2.9**). The measured potential correlated with the relative concentrations of AQDS and $AQDSH_2$, as expected and selective formation of $AQDSH_2$ was confirmed by UV-visible and ^1H NMR spectroscopy. The UV-visible spectrum of a sample of hydrogenated AQDS matched the spectrum of electrochemically generated $AQDSH_2$ (see this section's supplemental information). Two distinct sets of peaks were apparent in the ^1H NMR spectrum of a hydrogenated sample that was maintained under N_2, and these peaks disappeared upon exposure of the sample to air leaving only signals corresponding to AQDS.[16]

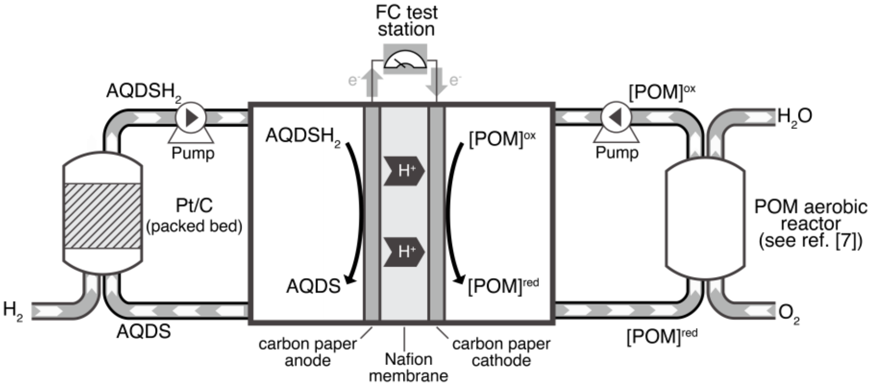

Figure 2.10: A schematic of the doubly mediated fuel cell.

With the successful demonstration of catalytic hydrogenation of AQDS under acidic conditions in batch, we then incorporated the Pt/C catalyst into a packed bed reactor (1/2" o.d. stainless steel tubing) to enable the continuous operation of an AQDS-mediated anode. The packed bed reactor was connected to the anode compartment of a 5 cm^2 fuel cell with serpentine flow plates. The membrane electrode assembly (MEA) featured a carbon cloth anode (Avcarb 1071HCB), a Nafion 115 membrane, and a conventional O_2 cathode (0.2 mg Pt/cm^2 on carbon). A solution of AQDS in 1 M H_2SO_4 was mixed with H_2 at a tee junction and fed into the packed bed reactor to charge the flow anode with reduced anthraquinone. The fuel cell was then operated at 60 °C with the liquid mediator solution cycled through the anode and reactor compartments, while O_2 was delivered to the cathode at 0.2 L/min. The preliminary results with this fuel cell arrangement, however, revealed significant complications associated with cathode flooding, arising from water migration through the membrane to the cathode. A power curve obtained during these tests showed significant mass-transport losses. (See associated publication for details). This phenomenon is not uncommon in liquid fuel cells and has been noted, for example, with other mediated anode [17] and direct methanol fuel cell systems.[18] To mitigate the impact of water crossover, we elected to replace the gas diffusion cathode with a mediated cathode system consisting of 0.3 M aqueous $Na_4H_3PMo_8V_4O_{40}$, a polyoxometalate (POM) similar to that reported previously.[7,19-20] Briefly, the POM solution was heated to 80 °C in a 75 mL vessel sparged with O_2, and the oxidized POM solution was flowed to the cathode compartment, where it underwent reduction and then circulated back to the regeneration compartment (see Section 4 of the Supporting Information for details). A schematic illustrating the resulting doubly mediated fuel cell is depicted in **Figure 2.10**.

A polarization curve for the AQDS/POM-mediated fuel cell was then collected using 1 M AQDS in 1 M H_2SO_4 at the anode at a state-of-charge of 90% (i.e., $AQDSH_2$:AQDS ratio of 90:10; **Figure 2.11 A**). An open-circuit potential of 0.73 V was observed, with a peak power density of 228 mW/cm^2 and an iR-corrected value of 528 mW/cm^2. Continuous fuel cell operation was established by matching the rate of the chemical reduction of AQDS in the packed bed reactor and the electrochemical oxidation of $AQDSH_2$ at the anode (**Figure 2.11 B**). Incorporation of a liquid reservoir between the anode and the packed bed reactor permitted in-line potentiometric monitoring of the mediator solution as well as the use of different liquid flow rates for improved performance in the individual units: 40 mL/min through the anode for improved mass transfer and 4 mL/min through the reactor to minimize pressure drop through the powder catalyst bed (for a schematic and photographs of the reactor set-up, see Figure S6). The integrated system sustained a current density of 50 mA/cm^2 at a mediator state-of-charge of approximately 70% for 8 hours. The contribution of the reactor to sustained system performance was confirmed in a separate experiment by interrupting the hydrogen flow over a period of one hour. The cell potential decreased steadily from 585 mV to 550 mV as the AQDS mediator state-of-charge decreased from 55% to 42%. Once hydrogen flow was reinitiated, reduction of AQDS ensued and the cell potential stabilized (see Figure S8 and Supporting Information for further details). These results demonstrate the steady-state integration of an electrochemical redox process (oxidation of $AQDSH_2$) with an off-electrode chemical redox reaction.

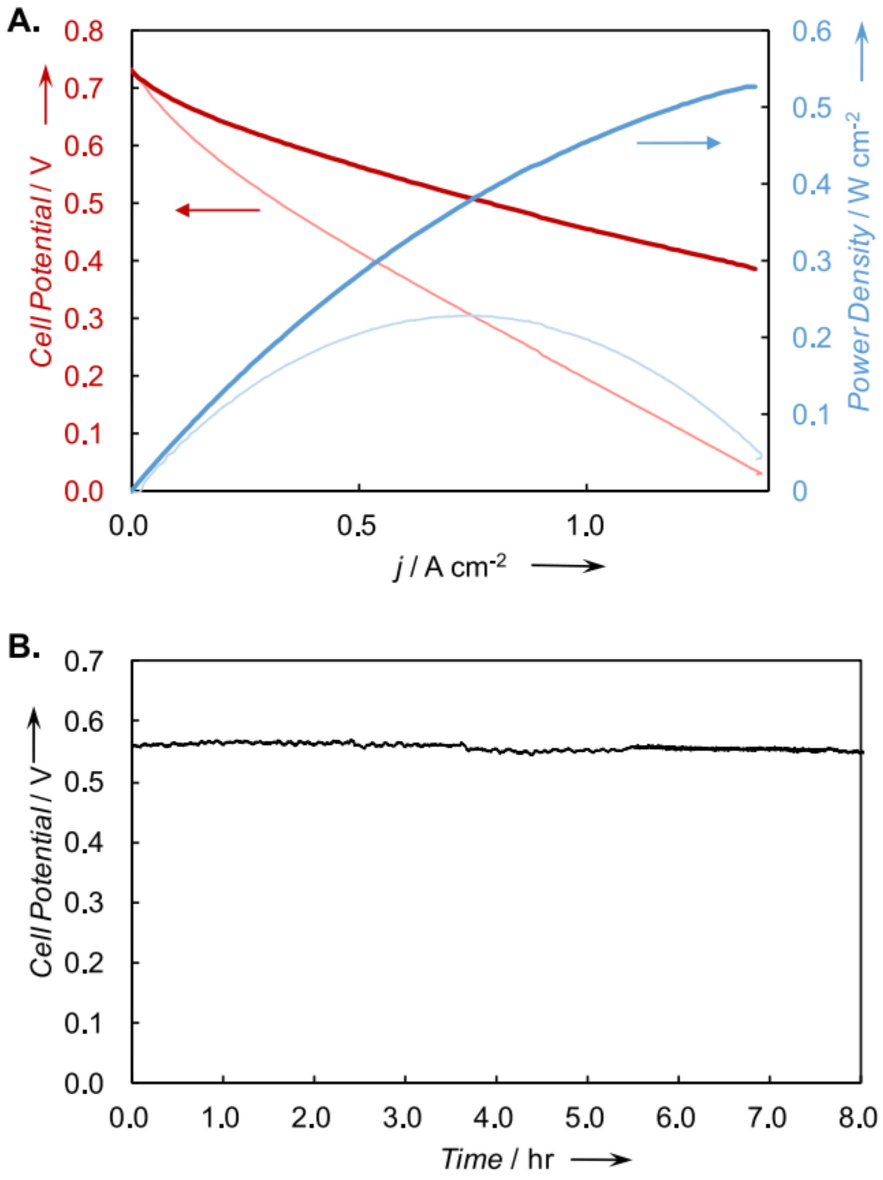

Figure 2.11: A. Polarization and power density curves with 1 M anthraquinone disulfonic acid in 1 M H_2SO_4 at the anode and 0.3 M $Na_4H_3PMo_8V_4O_{40}$ at the cathode. The fuel cell was operated at 60°C. B. Steady-state cell potentials observed from constant current operation of the doubly mediated fuel cell at 50 mA/cm^2.

The power densities and currents sustained in these experiments with AQDS are the highest reported to date for mediated electrolysis with hydrogen (**Figure 2.12**; see associated publication for calculation details). Early precedents for mediated fuel cells of this type employed hydrated metal ions as mediators, including $Ti^{3/4+}$, [21] $Sn^{2/4+}$, [22] $Fe^{2/3+}$, [22] $Cu^{0/2+}$, [22] and $Mo^{3/4+}$, [23] in addition to a Si-containing polyoxotungstate [23] and EDTA-ligated $Fe^{2/3+}$. [24] Each of these examples used off-electrode Pt or Pd catalysts for reduction of the mediator with H_2, although several examples only reported polarization curves, without demonstration of continuous, steady-state fuel cell operation.[22] The silicotungstic acid fuel cell accessed the highest power density at 136 mW/cm^2, or 173 mW/cm^2 with iR-compensation.

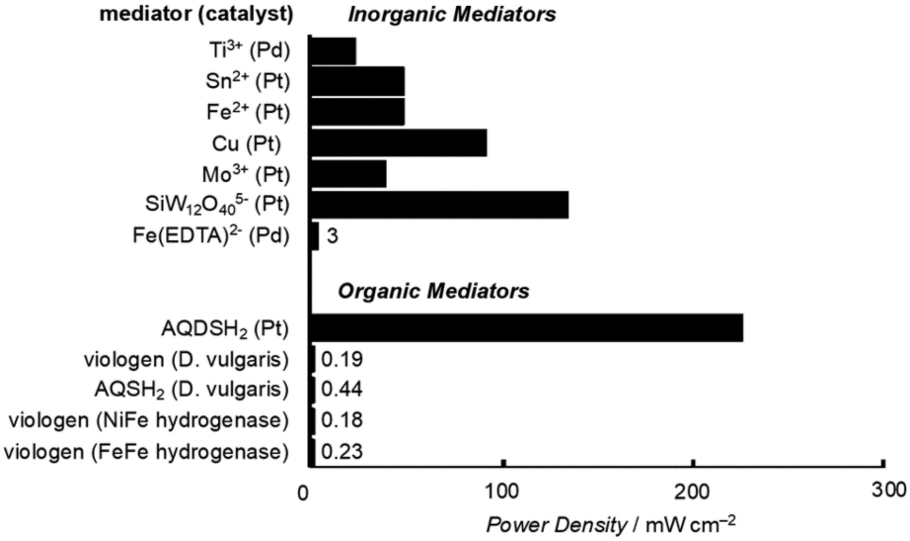

Figure 2.12: Comparison of power densities in fuel cells with anodic mediators using H_2 as the fuel. Power density was calculated from the highest performance reported in each reference.

More recently, organic mediators have been used in low power H_2 fuel cells to facilitate electron transfer with enzymatic catalysts. In the earliest example, 1.5 mM methyl viologen was paired with the bacterial cell *D. vulgaris* for a fuel cell with a power density of 0.19 mW/cm^2. [4b] Replacing the methyl viologen with 1.5 mM anthraquinone-2-sulfonic acid (AQS) increased the value to 0.44 mW/cm^2. Incorporation of viologen mediators into redox polymer networks with NiFe [25] and

FeFe[26] hydrogenases enabled power densities of approximately 0.2 mW/cm^2. The low power densities in these systems partly reflect the mild conditions needed to ensure enzyme stability and activity. For example, the pH typically varies from 4-11 and mediator concentrations are typically under 20 mM and operating temperatures under 40 °C. The ability to use a 1 M mediator concentration, operate the fuel cell at 60 °C, and employ a robust heterogeneous catalyst at pH 0 all contribute to the improved fuel cell performance observed in the present study.

Conclusion

The results described herein, which demonstrate the ability to produce power in a fuel cell by coupling a conventional catalytic hydrogenation reaction with electrochemical oxidation of an organic mediator, set the stage for a number of future research directions. Improved fuel cell performance should be accessible by using lower potential mediators that operate closer to the thermodynamic potential of the fuel. More broadly, this approach can leverage the widespread use of heterogeneous catalysts in organic chemical transformations. The development of new catalytic transfer (de)hydrogenation reactions between organic molecules and electrochemical mediators represents an important extension of the concepts reported here. For example, preliminary batch experiments show that formic acid and methanol may be used instead of H_2 to reduce AQDS to $AQDSH_2$ in the presence of a Pt/C catalyst (Figure S9). These results provide a starting point for development of mediated fuel cells that use more complex fuels than H_2. Such systems would have several appealing features, including ability to minimize fuel crossover and avoid gas generation at the electrode surface by moving the catalytic process off the electrode surface.[27]

Supplemental Information

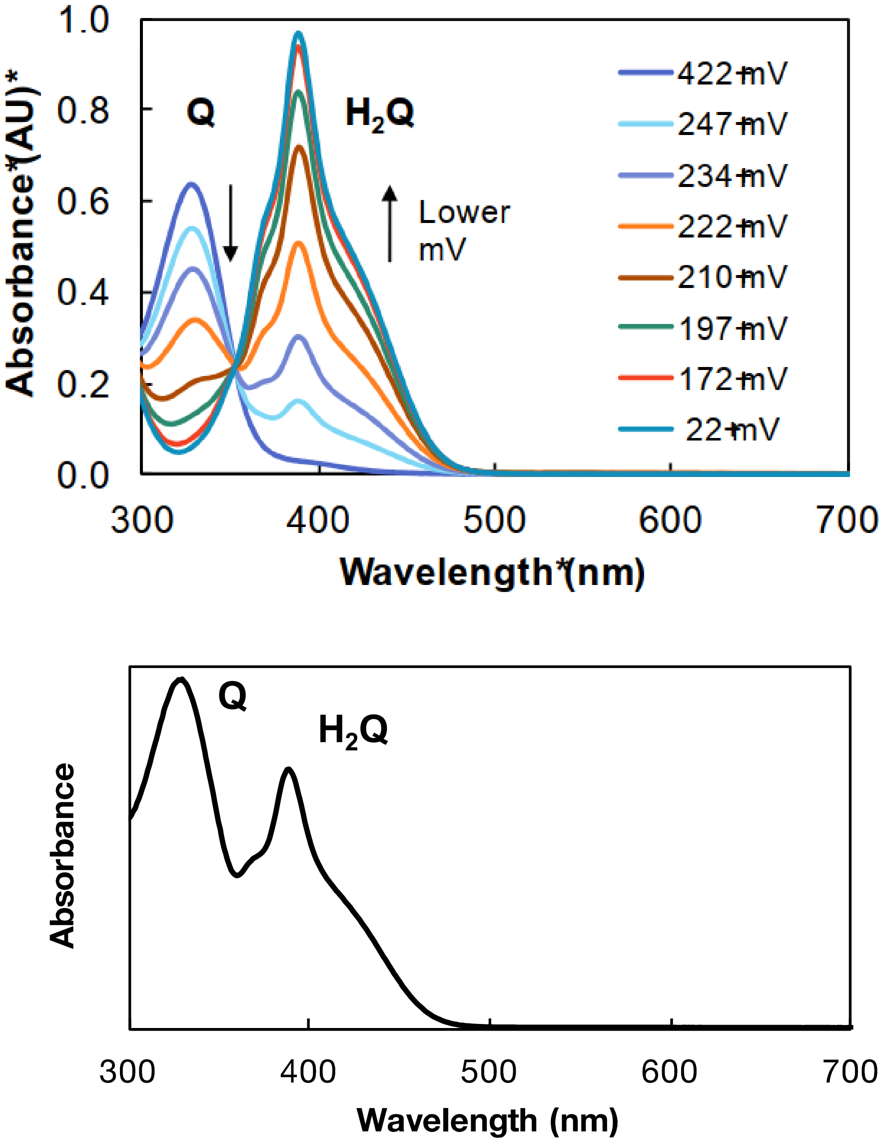

Figure 2.13: A. Spectroelectrochemistry of AQDS (0.1 mM) in 1 M H2SO4 on a Pt grid electrode. Potentials of 22 to 422 mV vs. NHE were applied. B. Spectrum of anthraquinone-2,7-disulfonic acid, disodium salt in 1 M H_2SO_4 following hydrogenation over a Pt/C catalyst.

UV-Vis analysis was used to compare the spectrum of electrochemically generated $AQDSH_2$ (acting as a standard) to that of the AQDS generated through chemical hydrogenation. Comparison of the resultant spectra confirms the claim of partial conversion through chemical hydrogenation.

Fuel Cell Preparation: The fuel cell hardware was supplied by Fuel Cell Technologies and the fuel cell test station by Scribner Associates Inc. The membrane electrode assembly (MEA) used a Nafion115 membrane sandwiched between 5 cm^2 carbon cloth electrodes (Avcarb 1071HCB). This was enclosed by two PTFE gaskets, graphite blocks with serpentine flow channels, current collectors (gold-plated copper plates), and aluminum heating blocks.

Fluid was circulated through the fuel cell using Cole-Palmer peristaltic pumps and Masterflex Tygon E-LFL tubing. 1/8 in. PTFE tubing passing through the heating blocks to the flow plates prevented fluid/metal contact.

For the anode, a glass beaker (reservoir) with 80 mL of ion-exchanged 1 M AQDS solution in 1 M H_2SO_4 was placed between the fuel cell and the reactor to enable operation at different flow rates (50-100 mL/min for the fuel cell to minimize mass transfer losses and up to 6 mL/min for the reactor to minimize pressure drop through the powder catalyst bed). A pump circulated the contents of the reservoir through a packed bed reactor. After reacting over the catalyst, the electrolyte was returned to the reservoir. To monitor the extent of the anthraquinone reduction, a working electrode (glassy carbon) and a reference electrode (Ag/AgCl) were placed in the reservoir. The solution color changed from orange/brown to green as the anthraquinone was reduced. At higher states of charge, or SoC (more anthrahydroquinone), the green color faded to yellow-orange, suggesting the break-up of the hydroxyanthraquinone-anthraquinone dimer.

The packed-bed reactor was made from a 1.75 inch length of 0.5 inch o.d. stainless steel tube with 0.5 inches of glass wool inside a Swagelok fitting with a 200-mesh stainless steel screen. Powdered catalyst (0.25 g of commercial 10 wt. % Pt/C from Strem Chemicals) was added, leaving 0.75 inches of open space for more glass wool to be retained by another 200-mesh stainless steel screen and Swagelok fitting.

The liquid solution was pumped through the reactor using a Hitachi L-6200 HPLC pump. The flow rate of H_2 was controlled by a Teledyne Hastings mass flow meter. The gas and liquid were mixed in an 1/8 in. tee and sent through a heated zone, after which they passed through the packed-bed reactor in an up-flow configuration. The pre-heated zone and packed bed reactor were wrapped in heating tape and the temperature maintained at 50 °C based on a built-in thermocouple touching the reactor wall.

For the cathode, a 0.3 M solution of the polyoxometalate (POM) $Na_4H_3PMo_8V_4O_{40}$ was synthesized according to the procedure disclosed in Odyakov et al.[28]

During fuel cell experiments, the solution was stored in a three-neck flask heated to 80 °C in a heating mantle. Solution was circulated to the fuel cell cathode from one neck (through a septum) and returned to the flask through a column of glass beads at another neck (to spread the solution and facilitate gas-liquid contact). An oxygen sparger was inserted at the third neck through a septum. The oxygen exited through the column of glass beads, in counter-current flow to the descending liquid solution. To facilitate reoxidation of the POM, care was taken to ensure that oxygen exited the flask only through the column. The solution color changed from blue/green to red/yellow as the POM was oxidized.

A liquid mediated cathode based on a polyoxometalate was used in the previous experiments because early experiments with a gas diffusion cathode had shown evidence of cathode flooding (Figure S7). A polarization curve completed with 30 mL/min of 0.1 M AQDS-Na_2 in 1 M H_2SO_4 at the anode (approximately 50 % state-of-charge) and 0.2 L/min O_2 at the cathode led to a power density of 43 mW/cm^2. Replacement of the gaseous cathode with a 75 mL reservoir of 0.3 M $Na_4H_3PMo_8V_4O_{40}$ flowing at 50 mL/min increased the power density to 177 mW/cm^2. With the gaseous cathode, the MEA consisted of a 5 cm^2 Nafion 117 membrane with a 0.2 mg Pt/cm^2 cathode and a piece of carbon cloth (Avcarb 1071HCB) for the anode. With the liquid cathode, the MEA included a 5 cm^2 Nafion 115 membrane with a piece of Avcarb 1071HCB carbon cloth at both the anode and cathode.

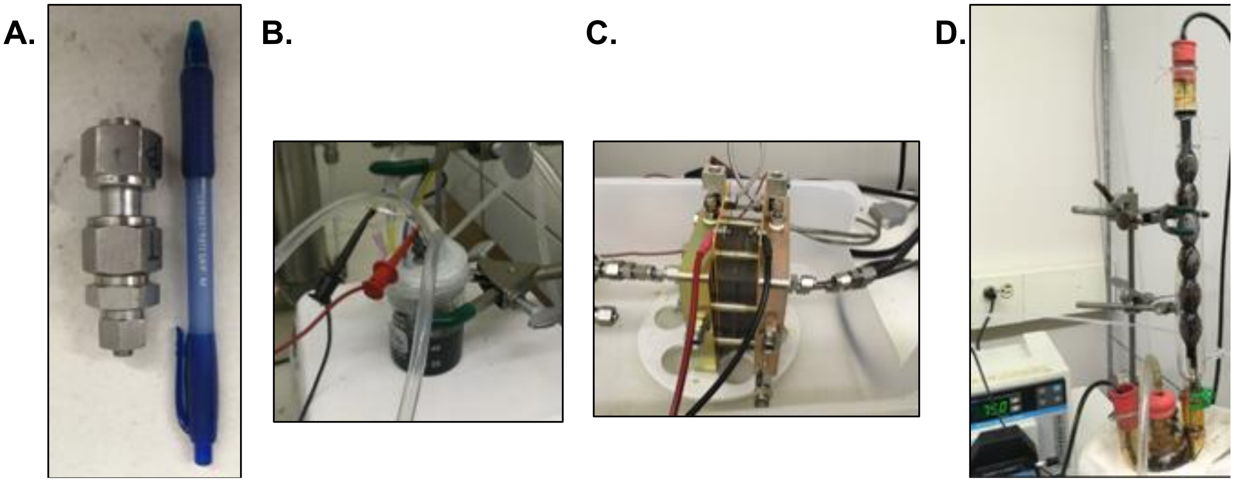

Figure 2.14: Photographs of various components of the mediated fuel cell. A. Packed bed hydrogenation reactor. B. Reservoir between hydrogenation reactor and fuel cell. C. Fuel cell. D. POM oxidation reactor.

AQDS Stability: Stability of the anodic mediator during fuel cell operation was assessed by ^{1}H-NMR. Using this spectroscopic approach, we were able to confirm the reversible formation of the anthrahydroquinone form of AQDS under reaction conditions. Samples were taken to characterize the mediator solution before and after prolonged use as mediator under operating fuel cell conditions, and the known autoxidation process was then used to confirm re-formation of the initial species (Figure 2.15).

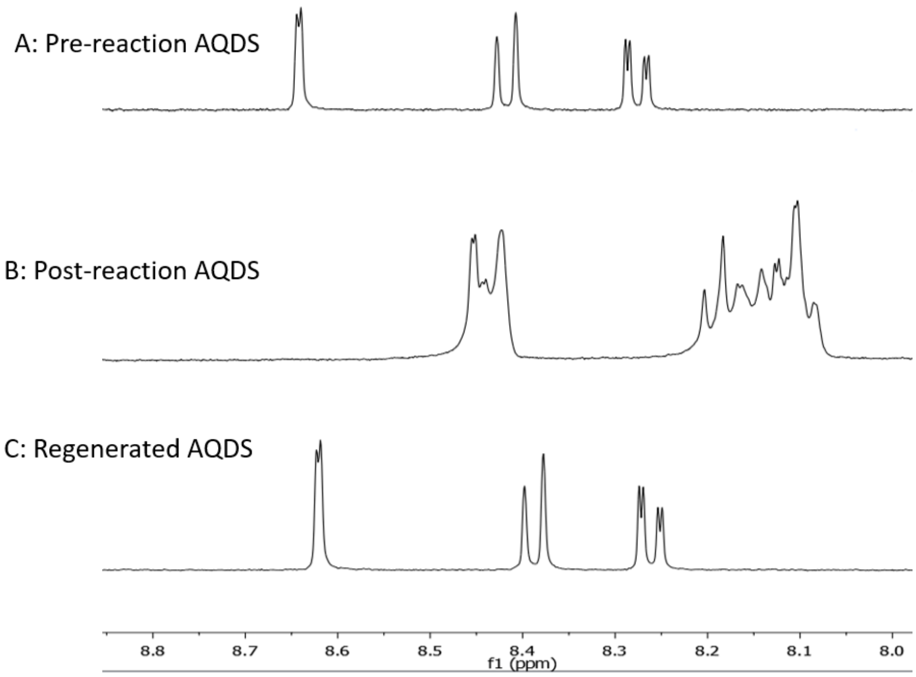

Figure 2.15: A. Ion-exchanged sample of AQDS: ^{1}H NMR (400 MHz, D_2O): 8.62 (d, J = 1.8 Hz, 2.0 H), 8.39 ppm. (d, J = 8.1 Hz, 2.0 H), 8.26 (dd, J = 8.1 Hz, 1.9 Hz, 2.0 H) ppm. B. Ion-exchanged AQDS after use as an anodic mediator for more than 8 hours (see **Figure 2.11 B**). The complex multiplets are the result

of overlap between oxidized and reduced AQDS. C. Sample B after exposure to air. The reduction is fully reversible, and no side peaks are observed.

References

1. a) E. Steckhan, *Angew. Chem. Int. Ed.* **1986**, *28*, 683-701;

   b) Y. N. Ogibin, M. N. Elinson, G. I. Nikishin, *Russ Chem Rev*. **2009**, *78*, 89-140;

   c) R. Francke, R. D. Little, *Chem. Soc. Rev*. **2014**, *43*, 2492-2521.

2. a) A. Hagfeldt, G. Boschloo, L. Sun, L. Kloo, H. Pettersson, *Chem. Rev*. **2010**, *110*, 6595-6663;

   b) B. D. McCloskey, D. Addison, *ACS Catal*. **2017**, *7*, 772-778;

   c) A. G. Wallace, M. D. Symes, *Joule*, **2018**, *2*, 1390-1395.

   d) G. L. Soloveichik, *Chem. Rev*. **2015**, *115*, 11533-11558.

   e) C. W. Anson, S. S. Stahl, *Chem. Rev*. **2020,** *120* (8), 3749-3786.

3. Examples of quinones in biofuel cells:

   a) X. Zhao, H. Jia, J. Kim, P. Wang, *Biotechnol. Bioeng*. **2009**, *104*, 1068-1074;

   b) Z. Zhu, Y.-H. P. Zhang, *Energy Sci. Eng*. **2015**, *3*, 490-497;

   c) R. D. Milton, D. P. Hickey, S. Abdellaoui, K. Lim, F. Wu, B. Tan, S. D. Minteer, *Chem. Sci*. **2015**, *6*, 4867-4875.

4. Examples of viologens in biofuel cells:

   a) G. T. R. Palmore, H. Bertschy, S. H. Bergens, G. M. Whitesides, *J. Electroanal. Chem.* **1998**, *443*, 155-161;

   b) S. Tsujimura, M. Fujita, H. Tatsumi, K. Kano, T. Ikeda, *Phys. Chem. Chem. Phys.* **2001**, *3*, 1331-1335;

   c) R. D. Milton, R. Cai, S. Abdellaoui, D. Leech, A. L. De Lacey, M. Pita, S. D. Minteer, *Angew. Chem. Int. Ed.* **2017**, *56*, 2680-2683.

---

5. N. Mano, A. de Poulpiquet, *Chem. Rev*. **2018**, *118*, 2392-2468.
6. For leading reviews of applications, see:

   a) S. C. Barton, J. Gallaway, P. Atanassov. *Chem. Rev*. **2004**, *104*, 4867-4886;

   b) M. Rasmussen, S. Abdellaoui, S. D. Minteer, *Biosens. Bioelectron.* **2016**, *76*, 91-102;

   c) M. Falk, C. W. Narváez Villarrubia, S. Babanova, P. Atanassov, S. Shleev. *ChemPhysChem*, **2013**, *14*, 2045-2058; d) Q. Xu, F. Zhang, L. Xu, P. Leung, C. Yang, H. Li. *Renew. Sust. Energ. Rev*. **2017**, *67*, 574-580.

7. D. B. Ward, N. L. O. Gunn, N. Uwigena, T. J. Davies, *J. Power Sources*, **2018**, *375*, 68-76.
8. For reviews of organic molecules in redox flow batteries, see:

   a) X. Wei, W. Pan, W. Duan, A. Hollas, Z. Yang, B. Li, Z. Nie, J. Liu, D. Reed, W. Wang, V. Sprenkle, *ACS Energy Lett.* **2017**, *2*, 2187-2204.

   b) J. Winsberg, T. Hagemann, T. Janoschka, M. D. Hager, U. S. Schubert, *Angew. Chem. Int. Ed*. **2017**, *56*, 686-711.

   c) P. Leung, A. A. Shah, L. Sanz, C. Flox, J. R. Morante, Q. Xu, M. R. Mohamed, C. Ponce de Leon, F. C. Walsh, *J. Power Sources*, **2017**, *360*, 243-283.

   d) J. Luo, B. Hu, M. Hu, Y. Zhao, T. L. Liu, *ACS Energy Lett.* **2019**, *4*, 2220-2240.

9. For selected primary references, see:

   a) B. Rausch, M. D. Symes, L. Cronin, *J. Am. Chem. Soc*. **2013**, *135*, 13656-13659;

   b) S. Liao, X. Zong, B. Seger, T. Pedersen, T. Yao, C. Ding, J. Shi, J. Chen, C. Li, *Nat. Commun*. **2016**, *7*, 11474;

c) W. Li, H.-C. Fu, L. Li, M. Cabán-Acevedo, J.-H. He, S. Jin, *Angew. Chem. Int. Ed.* **2016**, *55*, 13104-13108;

d) Y. G. Zhu, X. Wang, C. Jai, J. Yang, Q. Wang, *ACS Catal.* **2016**, *6*, 6191-6197.

10. Q. Chen, M. R. Gerhardt, L. Hartle, M. J. Aziz, *J. Electrochem. Soc*. **2016**, *163*, A5010-A5013.

11. For leading reference to the use of anthraquinones as anodic mediators in redox flow batteries, see:

a) B. Huskinson, M. P. Marshak, C. Suh, S. Er, M. R. Gerhardt, C. J. Galvin, X. Chen, A. Aspuru-Guzik, R. G. Gordon, M. J. Aziz, *Nature*, **2014**, *505*, 195-198;

b) B. Yang, L. Hoober-Burkhardt, F. Wang, G.K.S. Prakash, S. R. Narayanan, *J. Electrochem. Soc.*, **2014**, *161*, A1371-A1380;

c) K. Lin, Q. Chen, M. R. Gerhardt, L. Tong, S. B. Kim, L. Eisenach, A. W. Valle, D. Hardee, R. G. Gordon, M. J. Aziz, M. P. Marshak, *Science*, **2015**, *349*, 1529-1532.

d) L. Hoober-Burkhardt, S. Krishnamoorthy, B. Yang, A. Murali, A. Nirmalchandar, G. K. S. Prakash, S. R. Narayanan, *J. Electrochem. Soc.*, **2017**, *164*, A600-A607;

e) M. R. Gerhardt, L. Tong, R. Gomez-Bombarelli, Q. Chen, M. P. Marshak, C. J. Galvin, A. Aspuru-Guzik, R. G. Gordon, M. J. Aziz, *Adv. Energy Mater*., **2017**, 1601488.

f) D. G. Kwabi, K. Lin, Y. Ji, E. F. Kerr, M.-A. Goulet, D. de Porcellinis, D. P. Tabor, D. A. Pollack, A. Aspuru-Guzik, R. G. Gordon, M. J. Aziz, *Joule* **2018**, *2*, 1894-1906.

g) Y. Ji, M.-A. Goulet, D. A. Pollack, D. G. Kwwabi, S. Jin, D. De Porcellinis, E. F. Kerr, R. G. Gordon, M. J. Aziz, *Adv. Energy Mater.* **2019**, *9*, 1900039.

12. a) J. Piera, J.-E. Bäckvall, *Angew. Chem. Int. Ed*. **2008**, *47*, 3506-3523;

b) A. E. Wendlandt, S. S. Stahl, *Angew. Chem. Int. Ed.* **2015**, *54*, 14638-14658.

---

13. For leading references, see:

    a) H. Miyamura, M. Shiramizu, R. Matsubara, S. Kobayashi, *Angew. Chem. Int. Ed.* **2008**, *47*, 8093-8095;

    b) D. V. Jawale, E. Gravel, V. Geertsen, H. Li, N. Shah, I. N. N. Namboothiri, E. Doris, *ChemCatChem*, **2014**, *6*, 719-723;

    c) S. Donck, E. Gravel, A. Li, P. Prakash, N. Shah, J. Leroy, H. Li, I. N. N. Namboothiri, E. Doris, *Catal. Sci. Technol*. **2015**, *5*, 4542-4546.

14. For leading references, see:

    a) E. F. Rosenblatt, *J. Am. Chem. Soc.*, **1940**, *62*, 1092-1094;

    b) M. L. Khidekel, B. D. Polkovnikov, A. M. Taber, A. A. Balandin. *Izv. Akad. Nauk SSSR, Ser. Khim*. **1965**, *3*, 542-543;

    c) I. D. Entwistle, R. A. W. Johnstone, R. P. Telford, *J. Chem. Research (M)*, **1977**, 1382-1389.

15. a) G. Goor, J. Glenneberg, S. Jacobi in *Ullmann's Encyclopedia of Industrial Chemistry* (Ed.: B. Elvers), Wiley-VCH Verlag GmbH & Co. KGaA, **2007**, pp. 443-466;

    b) A. E. Wendlandt, S. S. Stahl in *Liquid Phase Aerobic Oxidation Catalysis* (Eds.: S. S. Stahl and P. Alsters), Wiley-VCH Verlag GmbH & Co. KGaA, **2016**, pp. 219-237.

16. Previous studies have suggested that anthrahydroquinones undergo acid-catalyzed disproportionation to the anthraquinone and the anthrone, but no new peaks were observed by 1H NMR spectroscopy in the present reactions.

---

a) F. Beck, G. Heydecke, *Ber. Bunsenges. Phys. Chem.*, **1987**, *91*, 37-43;

b) B. Wermeckes, F. Beck, *Denki Kagaku oyobi Kogyo Butsuri Kagaku*, **1994**, *62*, 1202-1205.

17. X. Zhao, J. Y. Zhu, *ChemSusChem*, **2016**, *9*, 197-207.
18. M. Ahmed, I. Dincer, *Int. J. Energy Res*. **2011**, *35*, 1213-1228.
19. While this work was ongoing, we were in the process of developing an alternative mediated cathode concept complementary to the present mediated anode system. The former approach is now published (ref. [20]) and would represent an alternative liquid cathode system.
20. Y. Preger, J. B. Gerken, S. Biswas, C. W. Anson, M. R. Johnson, T. W. Root, S. S. Stahl, *Joule*, **2018**, *2*, 2722-2731.
21. W. N. Carson, Jr., M. L. Feldman. *Proc. Ann. Power Sources Conf.*, **1959**, *13*, 111-113.
22. D.-G. Oei, *J. Appl. Electrochem.*, **1982**, *12*, 41-51.
23. J. T. Kummer, D.-G. Oei, *J. Appl. Electrochem.*, **1985**, *15*, 619-629.
24. B. Folkesson, *J. Appl. Electrochem.*, **1990**, *20*, 907-911.
25. N. Plumeré, O. Rüdiger, A. A. Oughli, R. Williams, J. Vivekananthan, S. Pöller, W. Schuhmann, W. Lubitz, *Nat. Chem.* **2014**, *6*, 822-827.
26. A. A. Oughli, F. Conzuelo, M. Winkler, T. Happe, W. Lubitz, W. Schuhmann, O. Rüdiger, N. Plumeré, *Angew. Chem. Int. Ed*. **2015**, *54*, 12329-12333.
27. a) M. Ahmed, I. Dincer, *Int. J. Energy Res.*, **2011**, *35*, 1213-1228.

    b) P. Kumar, K. Dutta, S. Das, P. P. Kundu, *Int. J. Energy Res*., **2014**, *38*, 1367-1390.
28. V. F. Odyakov, E. G. Zhizhina *React. Kinet. Catal. Lett*. **2008**, *95*, 21-28.

Chapter 3

Leveraging a Quinone-Mediated H_2 Anode for Ni-Catalyzed Cross-Electrophile Coupling

A manuscript for this chapter is being prepared for submission. A credit statement is provided below to clarify this author's contributions.

Johnson was a lead author for this work and was actively engaged in every part of its development. He led the design and implementation of the gram-scale flow reactor (featured in **Figures 3.3** and **3.4**), including characterization of the anodic mediator; contributed to the operation of the large-scale reactor (**Figure 3.4**); made minor contributions to the batch substrate scope (**Figure 3.2**); and collected or assisted in the collection of most of the data in the **Supplemental Information**. Johnson, Weix, and Twilton wrote the text of the manuscript, with edits from all authors.

Jack Twilton[†], Mathew R. Johnson[†], Cecilia Bottecchia, Dan Lehnherr, François Lévesque, Spring M. Knapp, Luning Wang, Vinayak Sidana, James B. Gerken, Mareena Franke, Cynthia M. Hong, Thomas P. Vickery, Mark Weisel, Neil A. Strotman, Daniel J. Weix, Thatcher W. Root, Shannon S. Stahl. Leveraging a Quinone-Mediated H_2 Anode for Ni-Catalyzed Cross Electrophile Coupling. In preparation for *Science.*

†These authors contributed equally to this work.

Abstract

Cross-coupling is a pivotal technology for modern organic synthesis as practiced in the synthesis of pharmaceuticals, fine chemicals, and natural products. Herein we report a method for the reductive cross-coupling of abundant aryl and alkyl halides delivering valuable $C_{sp}{}^3$–$C_{sp}{}^2$ coupled products. Key to our design is the use of hydrogen as terminal reductant, enabled by electrochemical oxidation of an organic mediator which is readily reduced by a heterogenous catalyst. The mediator, an inexpensive and readily available quinone, transfers electrons from H_2 to an electrochemical cell which "supercharges" their reducing ability and enables cathodic Ni-catalyzed cross-electrophile coupling. This approach obviates the need for sacrificial anode materials or stoichiometric metal reductants. This technology can be readily scaled for the synthesis of pharmaceutical ingredients and their precursors.

Introduction

The formation of C–C bonds is a key component of many industrially important organic synthetic routes, with special relevance in the pharmaceutical sector.[1, 2] This has traditionally been accomplished through Suzuki or Negishi reactions, coupling an organometallic nucleophilic substrate such as an organoboron or organozinc reagent to an electrophilic substrate, which is usually an organic halide or pseudohalide.[3] Recent synthetic advances are making it increasingly tractable to form new C–C bonds through cross electrophile coupling (XEC), a technique wherein the coupling partners are both electrophilic and a terminal reductant is consumed to facilitate bond formation.[4, 5] This approach is typically catalyzed by non-precious metals such as nickel, uses readily available and inexpensive starting materials, and crucially, can provide access C_{sp2}–C_{sp3} [6, 7]

and C_{sp2}–C_{sp2} bonds. [8, 9] These features make XEC highly attractive for chemical discovery, where it can offer alternative routes for the synthesis of new molecules from abundant raw materials.

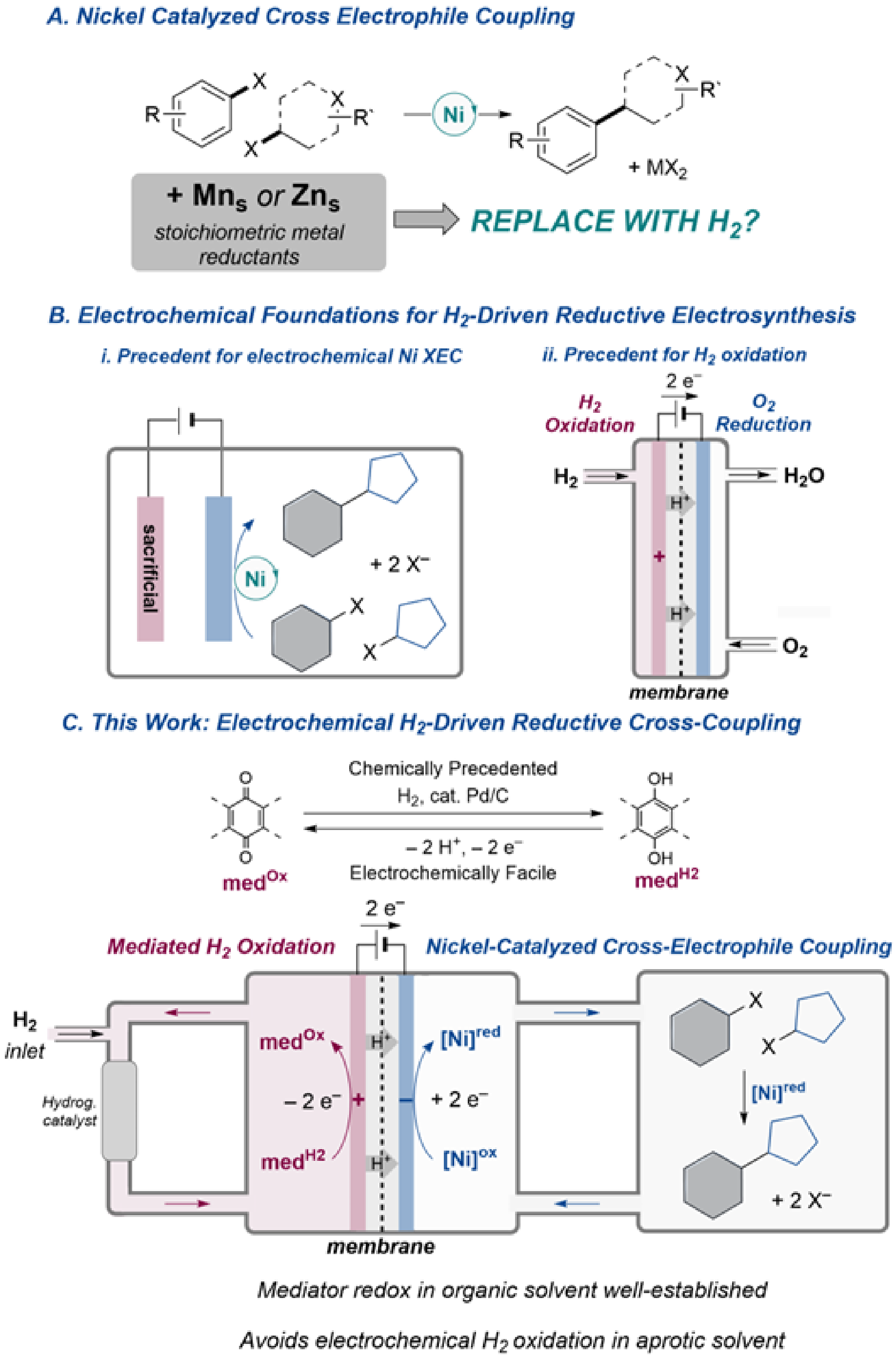

Figure 3.1: Strategies for Ni-Catalyzed Cross-Electrophile Coupling. A. Stoichiometric metals are typical reductants for Ni XEC and produce scalability challenges and stoichiometric waste. B. i. Electrochemically driven Ni XEC using sacrificial anode materials has been documented in the literature; ii. fuel cells demonstrate that oxidation of H_2 to drive cathodic electrochemistry is also feasible. C. An electrochemical flow cell using hydrogen as the terminal reductant to provide electrons for Ni XEC. The anode uses an organic redox mediator to manage protons and avoid the difficulties of H_2 oxidation in aprotic solvents.

However, implementing XEC on large scale presents several challenges, most stemming from currently available choices of terminal reductant. These reactions are typically performed using heterogeneous metal reductants such as zinc or manganese, which are supplied as granules or powders that can be non-uniform, leading to unpredictable reactivity and poor process robustness. [10, 11] These materials are also difficult to suspend in large reactors and the stoichiometric metal halide waste generated can be a process concern. [12] Ongoing research into alternative reductants has identified organic reductants such as amines, but these reductants are costly and their oxidation byproducts can sometimes exhibit downstream reactivity. [13–15] The ideal terminal reductant should be inexpensive, easily sourced, non-toxic, and should produce minimal waste. Hydrogen gas satisfies all of these constraints while also being a ubiquitous reductant in organic synthesis and integrating closely with renewable energy.

The use of hydrogen for Ni XEC requires solving several challenges. Hydrogen does not have sufficient thermodynamic driving force to reduce the nickel catalysts typically employed and it is not competent to drive the reaction. One means of solving these issues is to operate the cross-coupling reaction electrochemically, “supercharging” the hydrogen’s reduction potential with an applied electromotive force and controlling the rate of reduction of the XEC catalytic species by means of the applied current. Electrochemical XEC is precedented in the literature in both divided and undivided configurations, [16 – 18] while electrochemical hydrogen oxidation is highly precedented in fuel cell literature. [19] Fuel cells traditionally operate under aqueous acidic conditions, although the hydrogen oxidation reaction can also be conducted in organic solvent. Operating in non-aqueous systems requires careful choice of system components such as electrolyte, and tailored engineering solutions such as specially designed gas diffusion electrodes are required to enable bulk electrolysis.[20–22] Further inspiration can be drawn from work involving the use of redox mediators in fuel cells, which avoid entirely the need to oxidize hydrogen on-electrode.[23] Power densities in excess of 200 mW cm^{-2} have been reported for quinone-mediated systems that shuttle between an electrode and a heterogeneous catalyst for regeneration.[24, 25] In this work, we present a mediated electrochemical hydrogen anode system in which hydrogen gas is used as the terminal reductant to facilitate cathodic Ni XEC.

Results and Discussion

With these design principles in hand, we first sought to identify an appropriate anodic mediator. Drawing inspiration from anodically mediated fuel cell systems,[25] we tested sodium anthraquinone-2-sulfonate (AQS) as a likely candidate. Notable features of the AQS/$AQSH_2$ system included facile reduction with H_2 on common heterogenous reduction catalysts in amide solvents and a reduction potential low enough to capture most of the driving force of hydrogen oxidation (SI, **Figure 3.8**). The heterogenous catalyst screening indicated that AQS can be readily hydrogenated with H_2 utilizing 5 wt % Pd on carbon as catalyst at rates of approximately 0.4 mmol s^{-1} g^{-1}, normalized to total catalyst loading (SI, **Figure 3.8**), sufficient for incorporation into a practical flow system. Through CV analysis, we identified the redox potentials of the major anodic

(H_2, AQS) and cathodic (ligated Ni^I and Ni^{II} catalyst complexes) species in our solvent conditions (**Figure 3.2 A**, SI **Figure 3.5-3.7)**. We note that while the AQS couple captures the large majority of the driving force of H_2, it is insufficient to turn over the Ni catalysts by a margin of over 0.5 V. This implies that any XEC reactivity observed from coupling with the mediated hydrogen anode will necessarily involve the "supercharging" of our reductant.

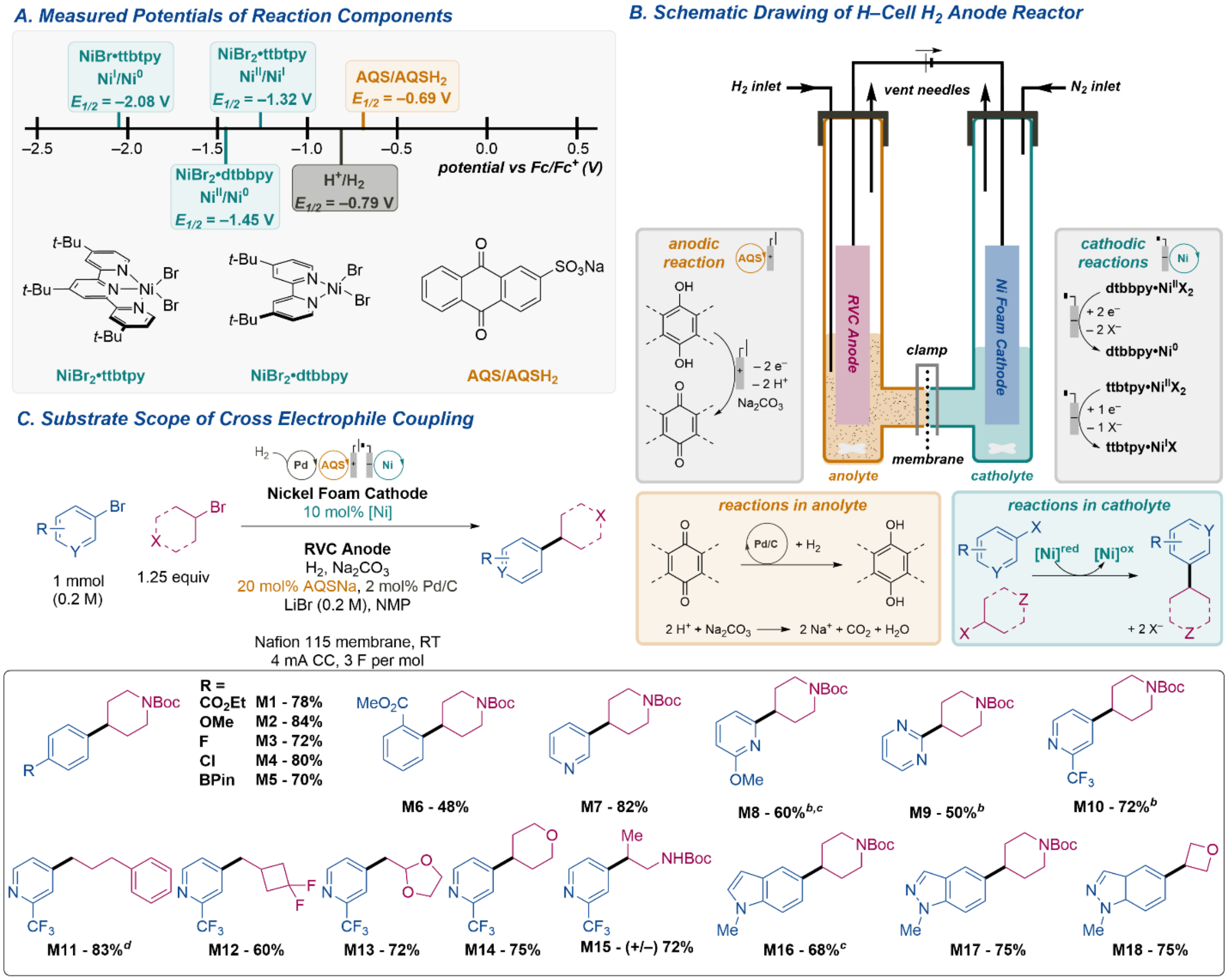

Figure 3.2: Substrate Scope for Hydrogen-Driven Ni XEC in Batch. A. Measured potentials of H_2, the AQS anodic redox mediator, and several Ni catalyst states, showing that hydrogen does not possess sufficient driving force to enable this reaction. B. Electrochemical substrate screening, conducted in an H-Cell,

demonstrates that supplying additional driving force through a power supply… C. enables access to a variety of products, including compounds with heterocycles and complex functional groups.

Having identified an appropriate mediator for H_2 oxidation in a flow configuration, the next step was to identify an appropriate nickel catalyst system for the cathodic reaction. We elected to optimize the Ni catalysis in a small-scale batch version of the mediated H_2 anode (see **Supplemental Information** for details) before moving to a larger-scale flow system. Based on our prior work on electrochemically-driven cross-electrophile coupling, [10, 26] we arrived at a two-catalyst system utilizing both 4,4’-di-*tert*-butyl-2,2’-bipyridine (dtbbpy) and 4,4′,4″-tri-*tert*-butyl-2,2′:6′,2″-terpyridine (ttbtpy) in a 4:1 ratio. The reactions were run in NMP solvent (0.2 M) with LiBr (0.2 M) as the supporting electrolyte and a small excess (1.25-1.5 equiv.) of the alkyl halide coupling partner. While not the focus of this study, the scope of these conditions with challenging, pharmaceutically relevant coupling partners is particularly notable (**Figure 3.2**). In particular, while our previous work with this system under electrochemical conditions provided lower yields with electron-rich aryl halides, under these H_2-coupled conditions electron-rich and electron-poor aryl bromides both coupled in high yield (**M2**, **M3**, **M5**, **M7**, **M16**). Lewis basic nitrogen heterocycles are prevalent in drug candidates but often require specialized conditions or even different catalysts. [14, 27] This single nickel dtbbpy/ttbtpy catalyst system can address a wide array of heterocycles, including pyridines (at the 2-, 3-, and 4-position), pyrimidine, indole, indazole, and pyrazole. Both secondary and primary alkyl bromides work equally well, regardless of sterics or ring-strain (**M17** vs **M18**). Additionally, the presence of ortho-coordinating groups and acidic protons was tolerated (**M6**, **M15**).

After validating both the anodic mediator and cathodic XEC conditions, we worked to design a flow reactor system suitable for gram-scale synthesis of Ni XEC products. Anodic performance was assessed in our proposed flow cell using a readily reduced oxoammonium-based cathode system (**Figure 3.3 A**). Solid Li_2CO_3 was loaded into the anodic reservoir to neutralize (or remove) the electrochemically generated acid and ICP analysis was used to ensure that the requisite cation migration to the cathode was indeed Li^+ (SI, **Figure 3.11**).

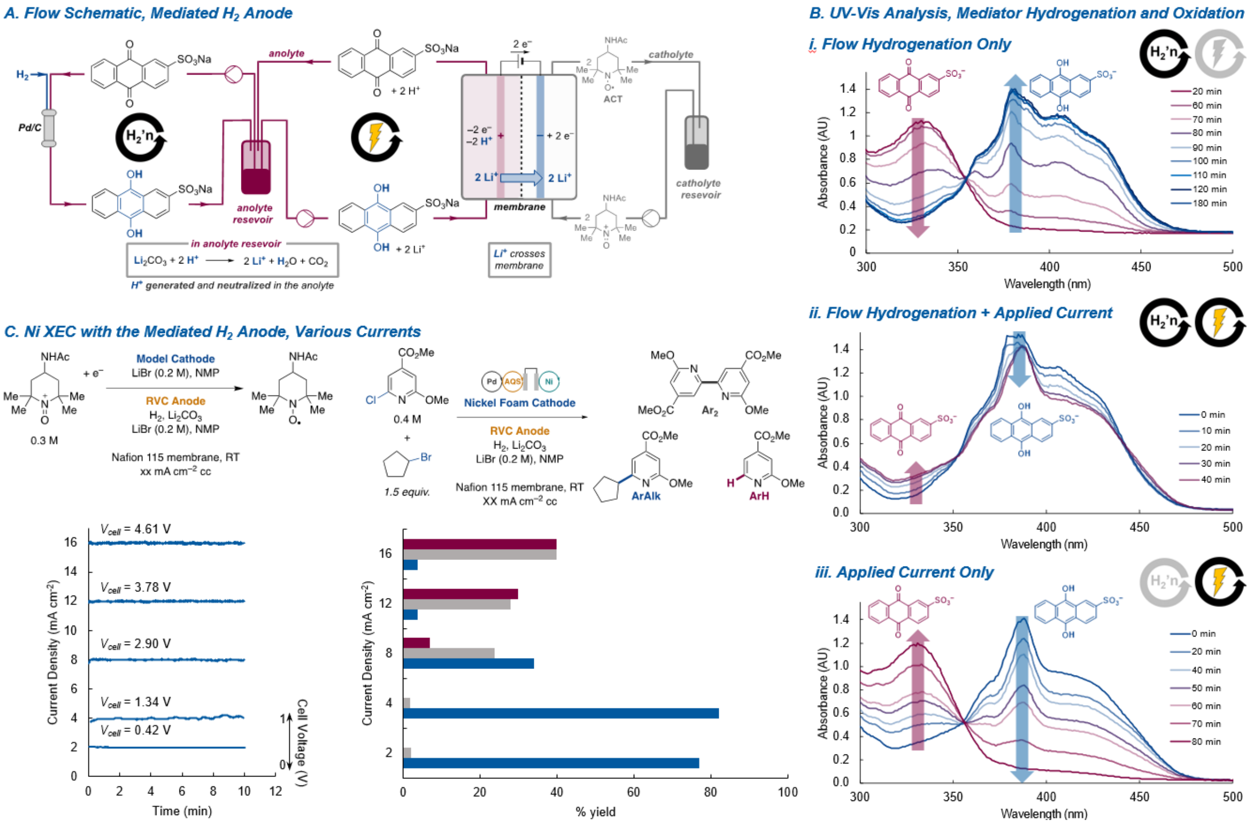

Figure 3.3: A. A schematic representation of the flow hydrogen anode system, featuring anodic and cathodic flow loops to the parallel plate reactor and an anodic hydrogenation loop through a catalytic packed bed. B. State of charge (SoC) characterization of the AQS mediator, using in-situ UV-Vis measurements of AQS and $AQSH_2$. (i) the mediator was passed through the hydrogenation loop and underwent reduction; (ii) while continuing the reductive loop, electrochemical oxidation was initiated and a steady state was

reached; (iii) cessation of reduction led to full re-oxidation of the mediator. C. Screening of accessible currents using the mediated hydrogen anode. Stable cell potentials are achieved through 16 mA/cm^2 when paired with the model cathode, indicating that the on-electrode AQSH$_2$ kinetics are sufficient to access these currents, but selectivity of the cathodic Ni XEC chemistry deteriorates above 4 mA/cm^2.

Mediator speciation between oxidized and reduced forms was interrogated by introducing a UV-Vis probe into the anodic reservoir and decreasing the anodic mediator concentration from 4 mM to 1 mM to stay within the linear Beer's Law regime. Operation of the hydrogenation loop without electrolysis shows full reduction of the AQS to AQSH$_2$ (**Figure 3.4 B, i**) and featured an isosbestic point at 355 nm, indicating that the reaction involved only interconversion of those species. Subsequent application of a 5 mA current while continuing to hydrogenate, the mode directly parallel to proposed synthetic operation, showed that the mediator reached a steady-state ratio of approximately 85% AQSH$_2$ (**Figure 3.3 B, ii**). Finally, ceasing hydrogenation while continuing to apply current showed regeneration of the initial AQS species while maintaining the isosbestic point, indicating full reversibility of the system (**Figure 3.3 B, iii)**. To additionally probe electrochemical performance, currents of 2–15 mA cm^{-2} were applied over short time intervals and cell voltage was monitored. Stable cell voltages at each applied current proved that the electroactive AQSH$_2$ species is kinetically capable of interfacing with the electrode at rates necessary to satisfy those demands (**Figure 3.3 C, i**). Ni XEC is typically performed at < 10 mA cm^{-2}, and attempts to utilize higher current densities showed a loss of selectivity for the cross-coupled product (**Figure 3.3 C, ii**). Together, these results suggested that the AQS-mediated flow system was well-suited for meeting all necessary demands for enabling synthesis of cross-coupled products.

As a showcase of the mediated hydrogen anode's utility, we proceeded to produce multiple pharmaceutical APIs on gram scale and to synthesize an intermediate for cenerimod on 81 g scale. The gram-scale syntheses translated seamlessly from batch conditions, maintaining similar yields while increasing throughput. These flow conditions were then linearly scaled (see **Supplemental Information** for details) from a parallel plate reactor where each electrode had an area of 5 cm^2 to one where each electrode had an area of 1600 cm^2, maintaining the same current density. High selectivity was maintained, despite a modest drop in yield, and throughput was increased to ~20 g/h. The success of this simple linear scaling contrasts sharply with the difficulties encountered with previously reported XEC-compatible reductants and suggests a clear line of sight for this technology to larger-scale production.

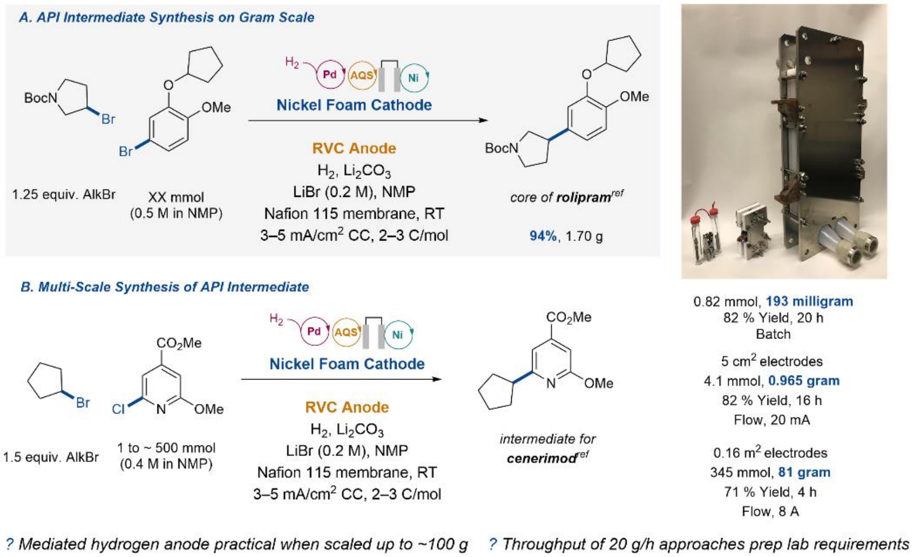

? Mediated hydrogen anode practical when scaled up to ~100 g ? Throughput of 20 g/h approaches prep lab requirements

Figure 3.4: Synthesis of API intermediates on scale. A. Synthesis of an intermediate for the drug, rolipram. Gram-scale, highly selective. B. Synthesis of an intermediate for the drug, cenerimod, at three different

scales. Moderate yields were achieved using a batch system (< 1 g), a small flow system (~1 g), and a large flow system (~100 g). Conditions for batch: Ni foam catholyte – 6 mol% $NiBr_2$•dtbbpy, 4 mol% $NiBr_2$•ttbtpy, 0.4 M LiBr. Carbon Anode – 5 mol% AQSNa, 1.5 equiv. Li_2CO_3, 0.4 M LiBr. Nafion 115 membrane, 4 mA cm^{-2}. Conditions for gram-scale: 5 cm^2 Ni foam

Conclusion

Taken together, these findings act as proof of concept for the mediated hydrogen anode system. As demonstrated, this new technology is well-suited for enabling electrochemical XEC reactions on scale by making hydrogen available as a low-cost and non-toxic reductant for organic electrochemistry. It also holds immense promise as a means of supplying reducing equivalents for other reductive reactions in a green and sustainable way. The application of an external potential minimizes the constraints of hydrogen's limited thermodynamic driving force.

Supplemental Information

Abbreviations:

Di-*tert-b*utyl bipyridine and dtbbpy refers to 4,4'-di-*tert*-butyl-2,2'-bipyridine.

4-*tert*-Butyl terpyridine, and ttbtpy refer to 4,4',4''-tri-*tert*-butyl-2,2':6',2''-terpyridine.

SM is sometimes used as an abbreviation for "starting material".

N-methylpyrrolidone (NMP)

cross electrophile coupling (XEC)

membrane electrode assembly (MEA)

reticulated vitreous carbon (RVC)

sodium anthraquinone-2-sulfonate (AQS)

sodium anthrahydroquinone-2-sulfonate (AQSH$_2$)

ferrocene (Fc)

cyclic voltammetry (CV)

open circuit potential (OCP)

Electrochemical Determination of Reduction Potentials: **Figure 3.2 A** depicts a series of reduction potentials for species of interest to this system. These were determined by CV and/or OCP analysis and were collected under reaction-relevant conditions as described below.

Electrochemical Evaluation of the Hydrogen Reduction Potential in NMP:

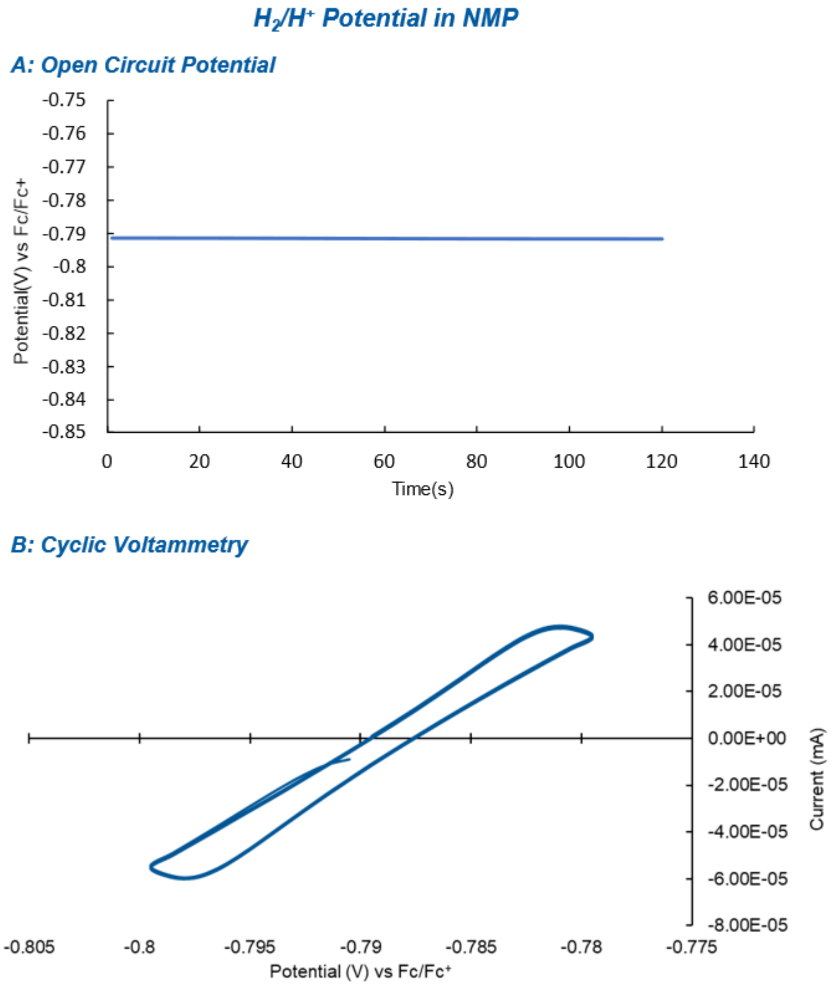

Figure 3.5: Electrochemical measurements for assessing the H_2/H^+ potential. Data was collected using a solution of 0.1 M CF_3SO_3H (proton source) and 0.1 M NBu_4PF_6 (supporting electrolyte) in NMP under an atmosphere of H_2. A glassy carbon working electrode, Pt counter electrode, and Ag/Ag^+ reference electrode were used. The reference was calibrated to $Fc^{+/0}$. A: OCP analysis showing a stable potential of –0.79 V; B: Complementary CV analysis, conducted at a scan rate of 10 mV/s, showing a zero-point potential at –0.79 V.

The H^+/H_2 reduction potential was characterized through both open circuit potential (OCP) and cyclic voltammetry (CV) analysis (**Figure 3.5**). CV analysis took place over a very narrow potential window centered around the open circuit potential and served to allow for calculation of a zero-point potential (E_z), the averaged potentials at which the voltammogram reached zero current on its oxidative (E_a) and reductive (E_c) sweeps. ($E_z = (E_a + E_c)/2$). This complementary analytical approach, reported in a recent study,[28] validated the OCP measurements and confirmed that the solution was electrochemically well-poised.

All measurements were conducted using a 1.6 mm diameter glassy carbon working electrode, platinum wire counter electrode, and Ag/Ag$^+$ reference electrode, with the latter then calibrated to Fc$^{+/0}$.

Electrochemical Mediator Evaluation:

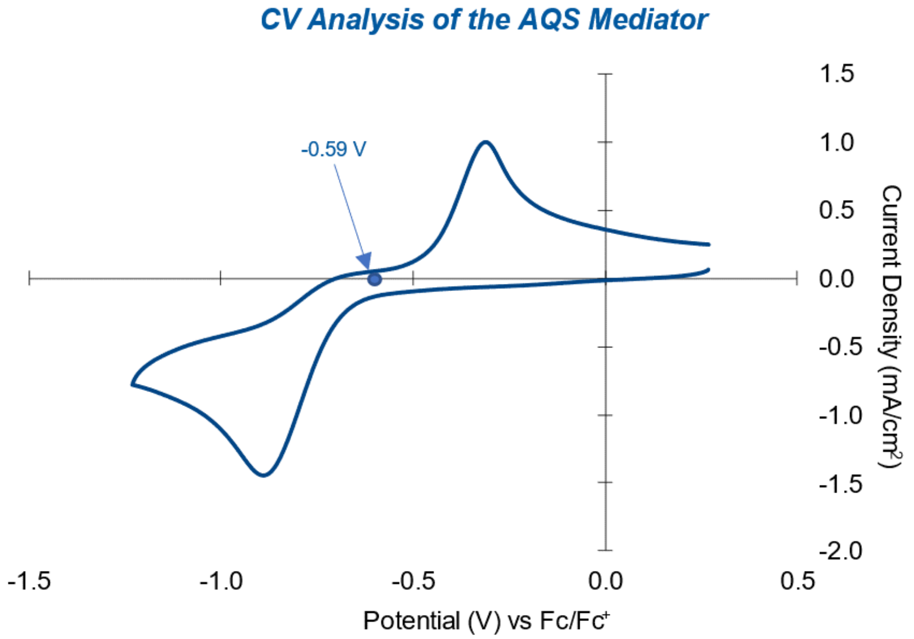

Figure 3.6: CV analysis of a 0.01 M AQS solution in NMP. 0.1M CF_3SO_3H proton source, N_2 atmosphere, 0.1 M NBu_4PF_6. Data was collected using a glassy carbon working electrode, and a platinum wire counter electrode at 100 mV s^{-1}. A Ag/Ag$^+$ reference electrode was used calibrated to Fc$^{+/0}$.

CV analysis was used to determine the reduction potential and electrochemical reversibility of mediator redox features in NMP. The use of anthraquinone 2,7-disulfonate (AQDS) is precedented in mediated fuel cells in aqueous acidic conditions, and so represented a natural starting point (see **Chapter 2**). Due to the low solubility of AQDS in NMP (<10 mM), however, the more soluble anthraquinone 2-sulfonate (AQS) was utilized instead. Figures of merit for mediator evaluation were a low measured redox potential, to capture as much of the hydrogen oxidation driving force as possible, and electrochemical pseudo-reversibility, as represented by a small peak-to-peak separation.

To a glass CV reaction vessel fitted with a cross shaped stir bar was added AQS (31.0 mg, 0.1 mmol), triflic acid (0.09 mL, 1 mmol), and 10 mL of 0.1 M NBu_4PF_6 in NMP solution. The vessel was then sealed with a cap fitted with a 1.6 mm diameter glassy carbon working electrode, Pt wire counter electrode and a Ag/Ag+ reference electrode. N_2 was bubbled through the solution for 20 min to degas the solution and cell. At this point, the gas stream was pulled above the solvent line, solution was allowed to become quiescent for two minutes, and a CV was collected (**Figure 3.6**). The trace showed a clear two-electron redox feature with $E_{1/2} = -0.59$ V vs $Fc^{0/+}$. The peak-to-peak separation was substantial at 0.55 V, indicating that electrochemical kinetics ought to be further investigated in the fully configured system (see **Figure 3.11** for further details). The redox potential was 200 mV below that of hydrogen, however, indicating that this mediator was thermodynamically suitable to be reduced by hydrogen while capturing most of the driving force of its oxidation.

Electrochemical Evaluation of Ni Catalysts for XEC:

The reduction potentials of the nickel catalysts used for XEC were determined by CV analysis (**Figure 3.7**). Midpoint potentials are noted on the x-axis and are represented in **Figure 3.2**.

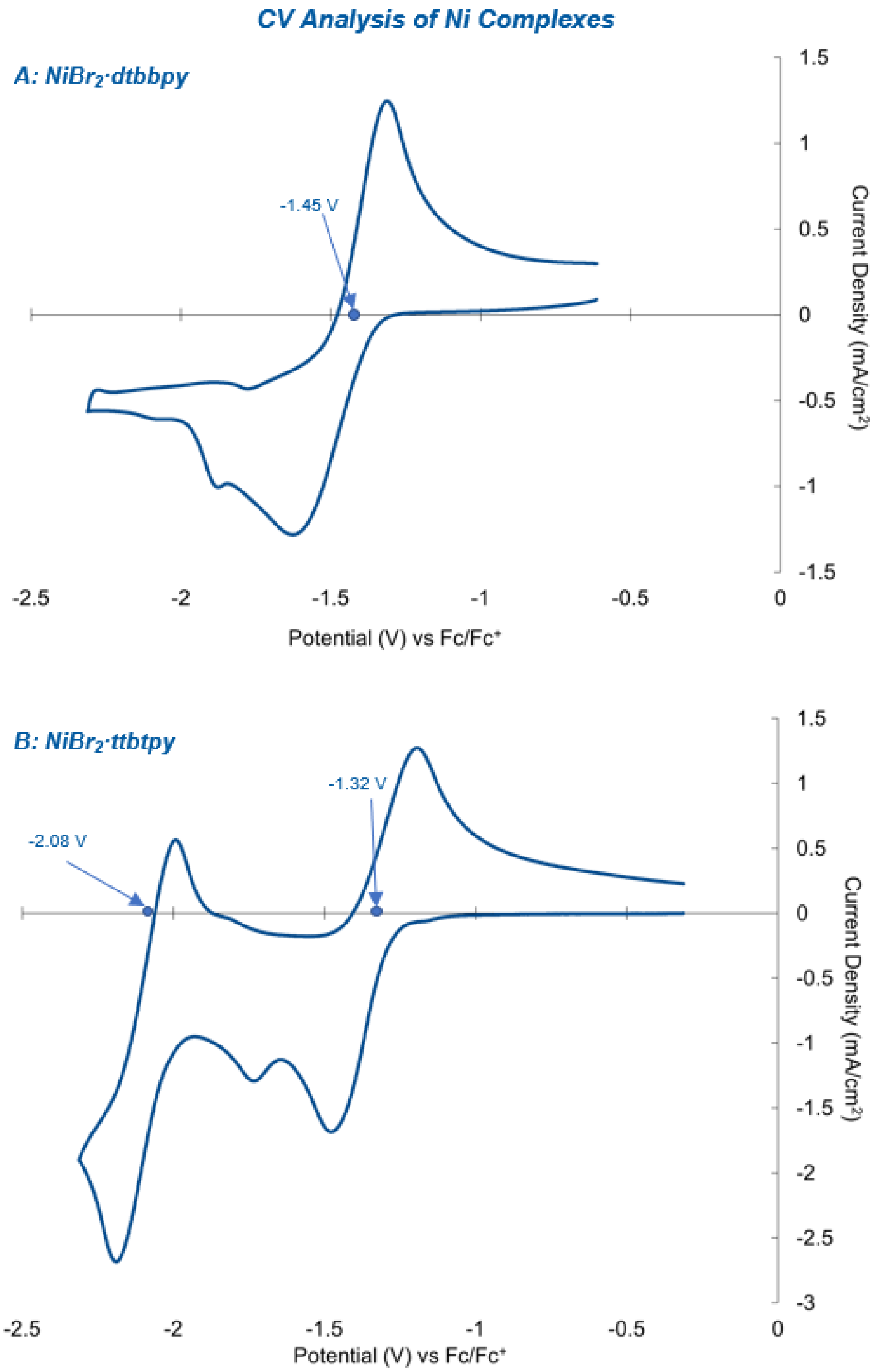

Figure 3.7: CV of a 0.01 M Ni solution in NMP with 0.1 M LiBr as supporting electrolyte. CV was conducted with a glassy carbon working electrode, platinum wire counter electrode at

100 mV s^{-1}. A Ag/Ag^+ reference electrode was used calibrated to $Fc^{+/0}$. A: $NiBr_2$•dtbbpy shows a single clear redox feature corresponding to a Ni^{II}/Ni^0 transition; B: $NiBr_2$•ttbtpy shows two redox features, a higher-potential feature corresponding to Ni^{II}/Ni^I and a lower-potential feature corresponding to Ni^I/Ni^0.

Evaluation of Hydrogenation Catalysts for Mediator Hydrogenation:

Hydrogenation catalysts for the identified AQS redox mediator were assessed in polar aprotic solvent. Pd/C was selected due it its extensive use as a reduction catalyst in the anthraquinone process for hydrogen peroxide synthesis,[29] and was then compared with Pt/C.

The solid catalyst (5 mol% metal, 0.005 mmol) and potassium carbonate (60 mg, 0.4 mmol, 4 equiv.) were weighed into thick-walled microwave vials fitted with oval shaped stir bars. The microwave vial was then fitted to a pressure transducer and sealed against atmosphere. The vial was evacuated and backfilled with H_2 three times before being sealed and allowed to equilibrate in a temperature-controlled ceramic block for 10 min. In a 20 mL vial was added AQS (310.3 mg, 1 mmol), and DMF (20 mL, 0.05 M). The vial was then sealed with a Teflon-lined screw cap and sparged with N_2 for 20 min. At this point, pressure change data began recording. A 2 mL aliquot of the 50 mM AQS solution was withdrawn and was added to each tube through a thick rubber septum. Magnetic stirring began (1200 RPM) and the pressure was monitored until it had equalized. The moment of solution injection was noted as a visible pressure spike on the uptake traces and was used as the starting point for the reaction. A decrease in pressure was measured and correlated to consumption of hydrogen. This method was used to screen catalyst identity, catalyst loading, and optimal reactor temperature (**Figure 3.8**).

Both Pd/C and Pt/C catalysts demonstrated rapid rates of AQS hydrogenation, achieving quasi-complete conversion within fifteen min. Pd/C was identified as optimal due to its lower cost.

At higher temperatures, however, the initial rate remained unchanged, but reactivity ceased well before complete substrate reduction. Reduction of the catalyst loading showed progressively earlier cessation of hydrogen consumption. These data suggest that the catalyst tolerates the AQS solution at room temperature, at least for short durations, but that it is deactivates at elevated temperature. For this reason, and given the sufficient RT reactivity, we chose to operate our reactor bed at room temperature.

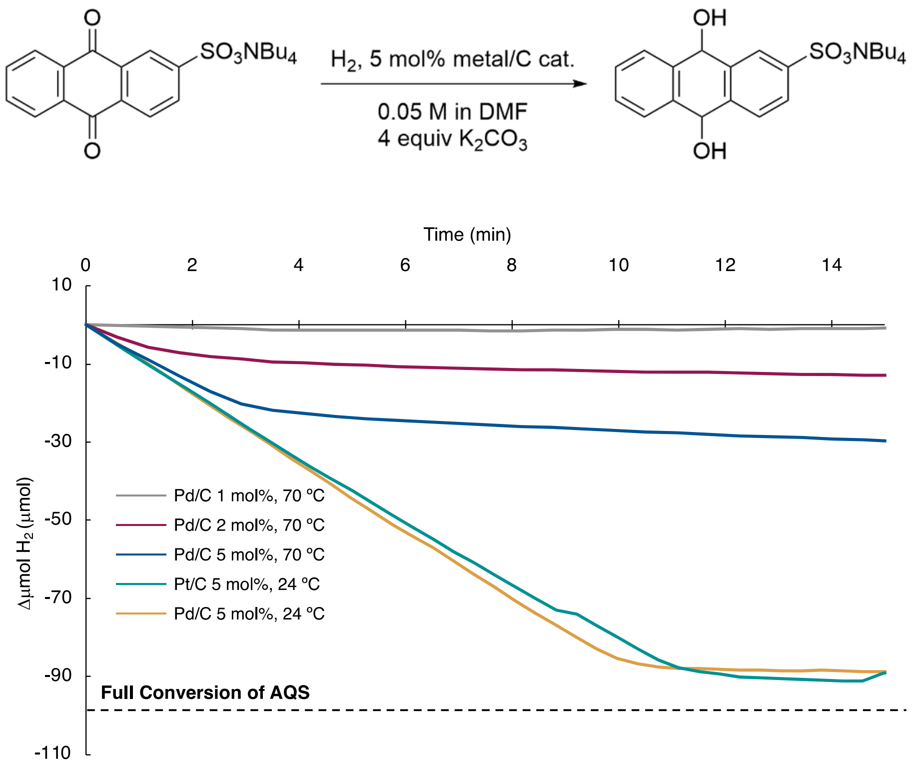

Figure 3.8: Reduction of AQS on carbon-supported Pt and Pd catalysts at 24 °C and 70 °C. Full substrate conversion would occur at 100 µmol of consumed H_2.

Mediated Anode Benchmarking using a Bobbitt's Salt Cathode:

An ElectroCell micro flow cell was used as the flow apparatus. The flow cell consisted of a Nafion 115 cation exchange membrane, a 5 cm^2 carbon paper anode distanced from the membrane with a

PTFE screen, a 5 cm^2 carbon paper cathode distanced from the membrane with a PTFE screen, and two PTFE flow frames, with incompressible components separated by Viton gaskets. Typically, these data were collected while maximizing parameters that would enable maximum attainable currents. Hence, the concentration of AQS in the anolyte was 0.3 M (5.58 g, 16.9 mmol) with 0.4 M Bu_4NBF_4 (7.9 g, 24 mmol 0.4 M) as supporting electrolyte, in 60 mL NMP (near the solubility limit of AQS in NMP) – a large excess of Li_2CO_3 was supplied for the purpose of the experiment. The catholyte consisted of 0.6 M Bobbitt's salt (4-acetamido-2,2,6,6-tetramethylpiperidine, 3.6 g, 12 mmol) and 0.4 M NBu_4BF_4 (2.63 g, 7.99 mmol) as the supporting electrolyte in 20 mL NMP, matching the faradaic capacity of the two solutions. The flow rate through the cell was 80 mL/min. Bobbitt's salt was readily reduced on a carbon paper electrode, leading to a symmetrical cell design (**Figure 3.9**).

The packed bed hydrogenation reactor (2.2" length, 0.5" OD) was made from a stainless-steel tube with 5 wt % Pd/C (50 mg, 0.023 mmol) retained using 1 inch of glass wool on each end. The anolyte solution, catholyte solution, and catalytic packed bed were prepared prior to operation.

Anolyte solution: two 24/40 rubber septa were punctured with a 14-gauge needle and Teflon tubing (1/8" ID and 3/16" OD) were threaded though the septa. This Teflon tubing was fitted with HPLC frits. To a 100 mL three-neck 24/40 round bottom flask with an oval stir bar was added AQS (5.58 mg, 18 mmol), Li_2CO_3 (665 mg, 9 mmol), and NMP (60 mL). Two of the openings were fitted with the septa fitted with the frits, the final opening was fitted with an unmodified 24/40 rubber septa, before stirring the solution for 20 min. H_2 gas was then vigorously bubbled through a 22-gauge needle into the solution to allow for hydrogen saturation of the solution.

Catholyte solution: to a separate 50 mL round bottom flask fitted with an oval shaped stir bar was added Bobbitt's salt (3.6 g, 12 mmol), NBu_4BF_4 (2.63 g, 7.99 mmol), and NMP (20 mL). This vessel was sealed with a rubber septum and placed under nitrogen atmosphere via headspace purge for 20 min. The catholyte was stirred for 10 min to ensure homogeneity.

A. *Schematic of Electrosyn Micro Flow Cell for H_2 Anode Bench-Marking with Bobbitt's Salt*

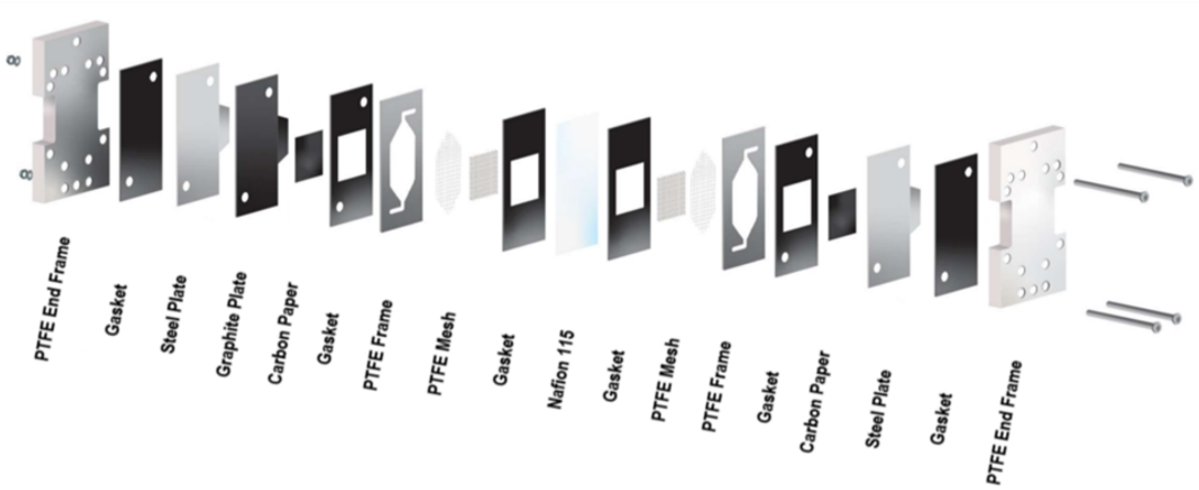

B. *H_2 Anode Parallel Flow Paths*

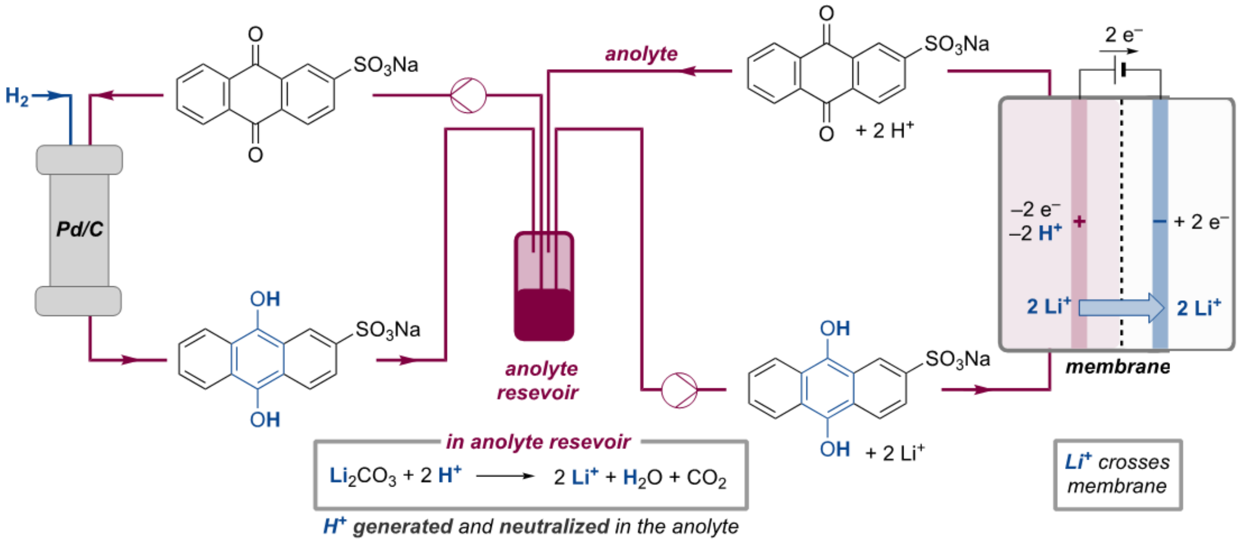

Figure 3.9: A. Schematic of ElectroCell Micro Flow Cell used for mediated H_2 Anode benchmarking. B. Schematic for anode flow path.

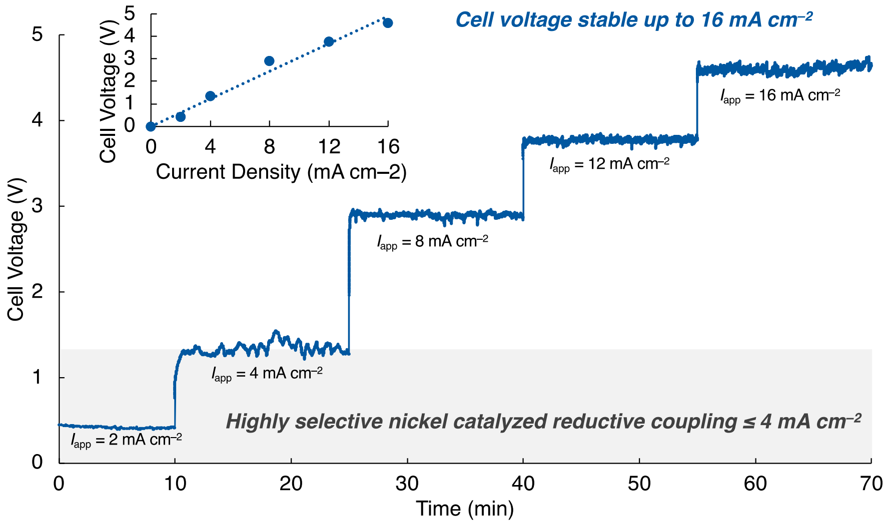

Figure 3.10: Current benchmarking experiments for electrochemical AQS mediated H_2 oxidation with Bobbitt's salt as terminal oxidant.

In the catalytic hydrogenation reactor, the AQS was reduced to anthrahydroquinone-2-sulfonate ($AQSH_2$) and the anolyte then flowed back into the reservoir. After 45 min, a second flow loop using a peristaltic pump to cycle anolyte and catholyte through the electrochemical flow cell was started. In ideality the $AQSH_2$ was oxidized on the carbon anode to form AQS and protons. The protons, separated from the proton exchange membrane by a PTFE screen, were carried back into the reservoir. Protons were prevented from accumulating by reaction with Li_2CO_3 in the anodic reservoir. On the cathode Bobbitt's salt is reduced. During electrolysis, a constant current was applied to the cell for each condition and was held constant for 15 min. Over this period, the cell voltage was measured and, where stable, was used as an indicator that the system was supplying electrons at the rate being tested. After each stable cell voltage, the applied current was increased.

As depicted in **Figure 3.10**, the cell voltage was stable at all measured current densities between 2–16 mA cm^{-2} (10–80 mA applied current). Each increase in potential led to a concomitant increase in cell voltage; as shown in the inset, these increases are linear and thus consistent with Ohmic losses due to fixed resistance within the system.

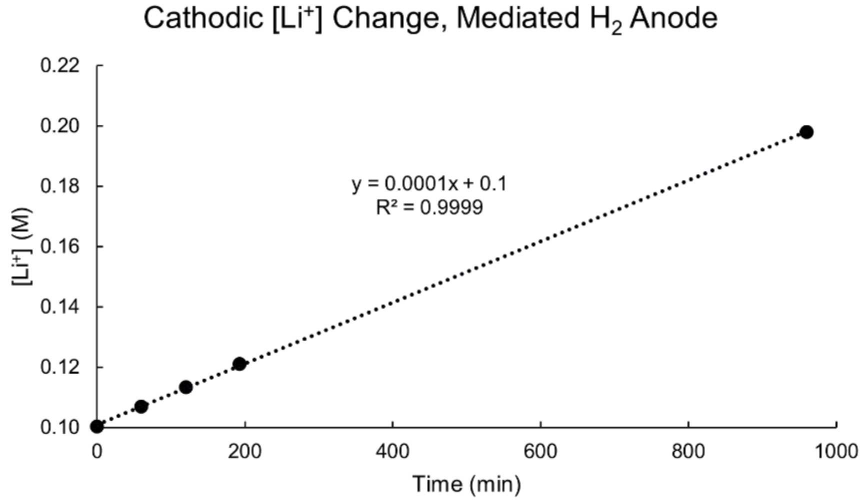

Figure 3.11: Time course for cathodic lithium concentration, monitored by ICP-OES.

The Bobbitt’s salt cathode configuration described in **Figure 3.9** was also used for experiments verifying proton control within the mediated H_2 anode system. Modifying the preparation to include a Li^+ electrolyte ($LiPF_6$) at 0.1 M in both anolyte and catholyte allowed the system to replicate a cation environment appropriate for XEC. The cathodic reservoir was substantially increased in volume while maintaining catholyte concentration (0.6 M Bobbitt’s salt, 7.2 g, 24 mmol), and constant current electrolysis was then conducted at 4 mA/cm^2 (20 mA) for 16 hours to mimic normal cell operation during gram-scale XEC reactions. Periodically over the course of the electrolysis, aliquots were withdrawn from the cathodic reservoir. These aliquots were then diluted and analyzed by inductively coupled plasma - optical emission spectrometry (ICP-OES) to track the Li content in the catholyte over time. As shown in **Figure 3.11**, we observe the correct starting concentration of Li (0.1 M, from electrolyte) followed by an excellent linear trend in Li crossover. The rate of Li crossover is slightly in excess of that required to ensure charge balance the applied current, implying that there is some small amount of non-Faradaic crossover as well.

Evaluation of Current Density on Selectivity of Ni-Catalyzed Cross Electrophile Coupling:

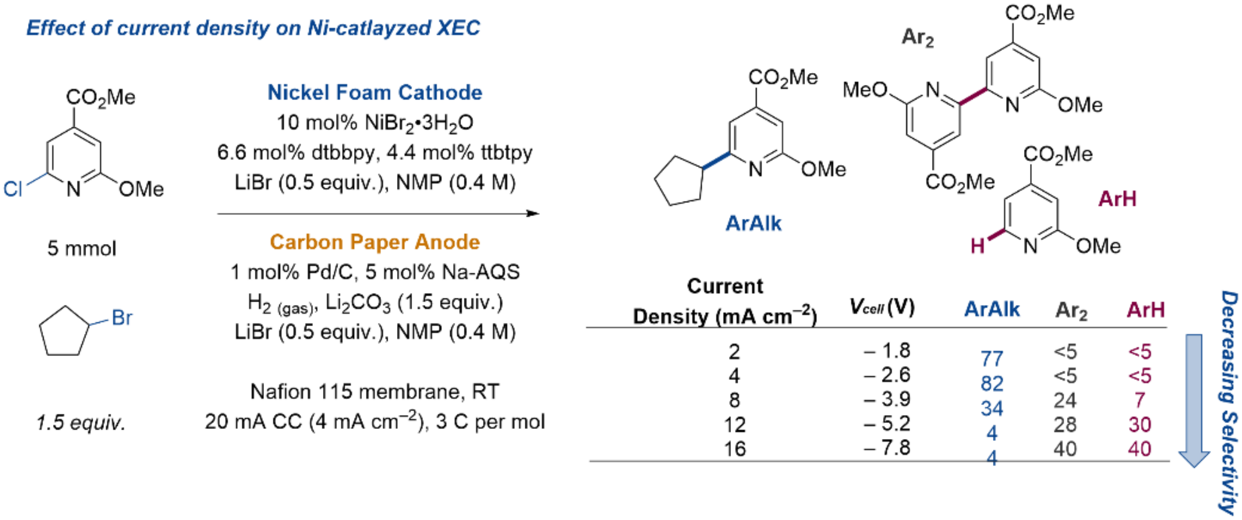

Current Density (mA cm^{-2})	V_{cell} (V)	ArAlk	Ar$_2$	ArH
2	– 1.8	77	<5	<5
4	– 2.6	82	<5	<5
8	– 3.9	34	24	7
12	– 5.2	4	28	30
16	– 7.8	4	40	40

Figure 3.12: Ni-catalyzed cross electrophile coupling used to evaluate effect of current density on selectivity.

To demonstrate that the mediated H_2 anode provided sufficient current density to enable Ni-catalyzed cross electrophile coupling, the cross coupling of methyl 2-chloro-6-methoxyisonicotinate and bromo cyclopentane were evaluated at multiple current densities in flow (see also **Figure 3.3**). The mediated H_2 anode can supply >15 mA cm^{-2} while maintaining a stable voltage. As shown in **Figure 3.12**, the Ni-catalyzed cross coupling shows diminished selectivity at current densities greater than 4 mA cm^{-2}. We hypothesize the decreased selectivity observed at higher current densities is due to mismatched rates of oxidative addition and alkyl radical generation mediated by the two different ligated Ni species.

Procedures for Operation in Batch, Gram-Scale Flow, and Large-Scale Flow Configurations:

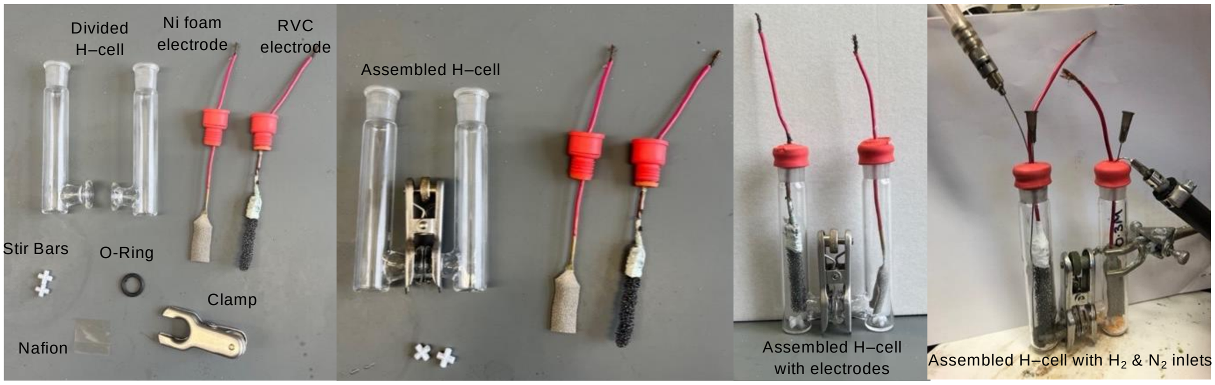

Figure 3.13: Photos of divided H–Cell as it is assembled – used for batch optimization of Ni-catalyzed XEC and for development of the substrate scope.

General Procedure for Reaction Optimization in a Divided H–cell: In a nitrogen filled glove box, to a 6-dram vial fitted with a cross shaped stir bar and a Teflon-lined cap was added supporting electrolyte (4 mmol) and solvent (20 mL). The mixture was stirred in a glove box until complete dissolution of the electrolyte. This vial was then removed from the glove box and placed under positive pressure on nitrogen on a Schlenk line. A 2.5 × 2.5 cm square of Nafion 115 was cut and placed in a small beaker. A 1 mL aliquot of the 0.2 M electrolyte solution was removed under positive pressure of nitrogen and used to soak the Nafion membrane for 10 min. A divided H–cell was then assembled around the Nafion membrane using a Viton O-ring and ring clamp to secure the cell (**Fig. S8**). Each chamber of the cell was fitted with a cross shaped stir bar. To the anodic chamber was added 5 wt % Pd/C (42 mg, 0.02 mmol, 2 mol%), AQS (62 mg, 0.2 mmol, 20 mol%), and Na_2CO_3 (210 mg, 2 mmol, 2 equiv.). A 5 cm × 1 × 0.5 cm rectangle of RVC was cut using a razor blade and affixed to copper wire. A 14/20 rubber septum was punctured with a 14-gauge needle and the copper wire (with RVC electrode) was threaded through the rubber septum before removal of the needle. The RVC electrode was then placed in the anodic chamber roughly 5 mm above the stir bar and the 14/20 joint sealed with the rubber septum.

To the cathodic chamber was added $NiBr_2•3H_2O$ (27.3 mg, 0.100 mmol, 10 mol%), dtbbpy (varying quantities), and ttbtpy (varying quantities). A 2 × 4 cm rectangle of nickel foam was cut and affixed to copper wire (folded over the wire and crimped with a pair of plyers). A 14/20 rubber septum was punctured with a 14-gauge needle and the copper wire (with nickel foam electrode) was threaded through the rubber septum before removal of the needle. The nickel foam electrode was then placed in the cathodic chamber roughly 5 mm above the stir bar and the 14/20 joint sealed with the rubber septum. The headspace of chamber of the H–cell was cleared via nitrogen flush for 10 min. The anodic compartment headspace was then cleared with hydrogen gas for 10 min. The electrolyte in solvent solution was withdrawn using a syringe; 5 mL was added to the cathodic compartment under nitrogen atmosphere, and 7.5 mL was added to the anodic compartment. The hydrogen purge needle was submerged under the surface of the solution and hydrogen flow rate adjusted to provide roughly one bubble per second, the anolyte and catholyte were stirred at 600 RMP until complete dissolution of the catholyte. At this stage ethyl 4-bromobenzoate (230 mg, 1.0 mmol, 1.0 equiv) and 1-bromo-3-phenylpropane (varying quantities) were added to the catholyte via Hamilton syringe. The copper wires were attached to a BASi Epsilon or CH instruments potentiostat with the cathode identified as working electrode and the anode as counter and reference electrode. Constant current electrolysis was performed until 3.5 F/mol had passed, or until the cell potential reach –10 V. Upon completion of the reaction, the catholyte was transferred via Eppendorf pipette to a 4 dram vial. The cathode and cathode chamber were rinsed with MeCN and these rinsings were transferred to the vial. 1,3,5-Trimethoxybenzene (84 mg, 0.5 mmol, 0.5 equiv) was added to the vial as internal standard. Either a 2 μL aliquot was removed and diluted into 200 μL 3:1 (v/v) mixture of MeCN/DMSO for UPLC-MS analysis, or a 50 mL aliquot was removed and diluted into 500 mL of MeCN-d_3 for ^{1}H NMR analysis. A 400 MHz NMR spectrometer was used with a d1 value of 6 seconds with 32 scans.

General Procedure for Substrate Screening in a Divided H-Cell: In a nitrogen filled glove box, to a 6-dram vial fitted with a cross shaped stir bar and a Teflon lined cap was added LiBr (347 mg, 4.00 mmol) and NMP (20 mL) to generate a 0.2 M LiBr in NMP electrolyte solution. The mixture was stirred in a glove box until complete dissolution of the LiBr. This vial was then removed from the glove box and placed under positive pressure on nitrogen on a Schlenk line. A 2.5 × 2.5 cm square of Nafion 115 was cut and placed in a small beaker. A 1 mL aliquot of the 0.2 M LiBr solution was removed under positive pressure of nitrogen and used to soak the Nafion membrane for 10 min. A divided H–cell was then assembled around the Nafion membrane using a Viton O-ring and ring clamp to secure the cell. Each chamber of the cell was fitted with a cross shaped stir bar. To the anodic chamber was added 5 wt % palladium on carbon (42 mg, 0.020 mmol, 2 mol%), AQS (62 mg, 0.19 mmol, 20 mol%), and Na_2CO_3 (210 mg, 2 mmol, 2 equiv.). A 5 cm × 1 × 0.5 cm rectangle of RVC was cut using a razor blade and affixed to copper wire. A 14/20 rubber septum was punctured with a 14-gauge needle and the copper wire (with RVC electrode) was threaded through the rubber septum before removal of the needle. The RVC electrode was then placed in the anodic chamber roughly 5 mm above the stir bar and the 14/20 joint sealed with the rubber septum.

To the cathodic chamber was added $NiBr_2•3H_2O$ (27.3 mg, 0.105 mmol, 10 mol%), dtbbpy (23.6 mg, 0.088 mmol, 8.8 mol%), and ttbtpy (8.8 mg, 0.022 mmol, 2.2 mol%). At this stage if the aryl halide, or alkyl halide coupling partners were solid they were added to the cathodic compartment. A 2 × 4 cm rectangle of nickel foam was cut and affixed to copper wire (folded over the wire and crimped with a pair of plyers). A 14/20 rubber septum was punctured with a 14-gauge needle and the copper wire (with nickel foam electrode) was threaded through the rubber septum before removal of the needle. The nickel foam electrode was then placed in the cathodic chamber roughly 5 mm above the stir bar and the 14/20 joint sealed with the rubber septum. The head space of chamber of the H–cell was cleared via nitrogen flush for 10 min. The anodic compartment head space was then cleared with hydrogen gas for 10 mins. The electrolyte solution was withdrawn using a syringe; 5 mL was added to the cathodic compartment under nitrogen atmosphere, and 7.5 mL was added to the anodic compartment. The hydrogen purge needle was submerged under the surface of the solution and hydrogen flow rate adjusted to provide roughly one bubble per second, the anolyte and catholyte were stirred at 600 RPM until complete dissolution of the catholyte. At this stage if the aryl or alkyl halide electrophile where a liquid they were added to the cathodic compartment via Hamilton syringe. The copper wires were attached to a BASi Epsilon or CH instruments potentiostat with the cathode identified as working electrode and the anode as counter and reference electrode. Constant current electrolysis was performed at –3 to –4 mA until the passage of 3.5 F/mol or until the cell potential reached –10 V. Upon completion of the reaction, the catholyte was collected and concentrated under reduced pressure to dryness. The resultant residue was dissolved in EtOAc and passed through a small plug of silica to remove metal salts, concentrated under reduced pressure to dryness, and purified by silica gel chromatography.

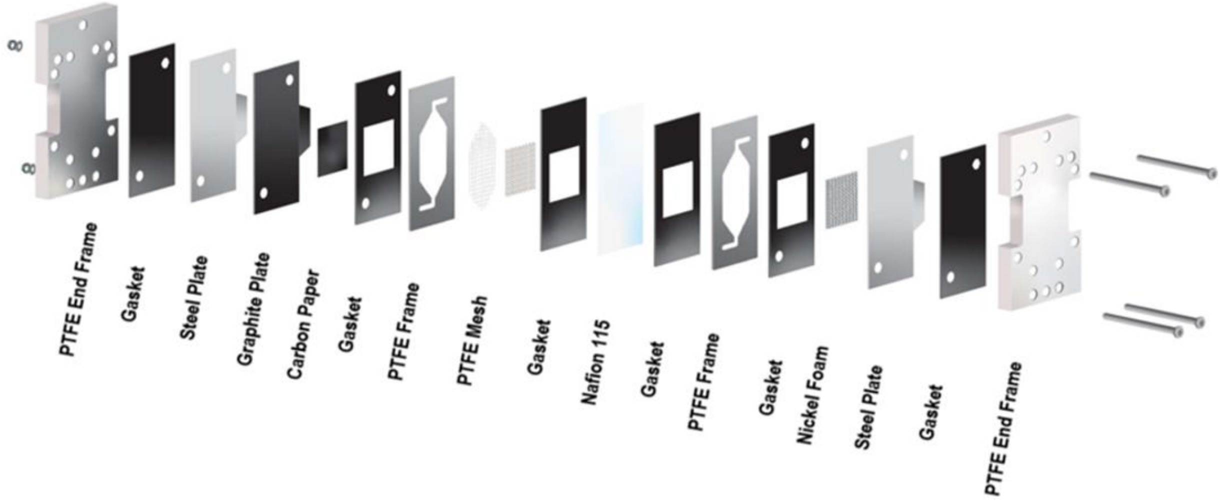

Figure 3.14: Schematic of micro flow cell from ElectroCell used for mediated H_2 anode synthesis on gram scale.

General Procedure for Ni XEC in the Gram-Scale Flow Cell: An ElectroCell micro flow cell (**Figures 3.14**, **3.15**) was used as the flow apparatus. The flow cell consisted of a Nafion 115 cation exchange membrane, a 5 cm^2 carbon paper anode distanced from the membrane with a PTFE screen, a 5 cm^2 commercial nickel foam cathode directly against the membrane, and two PTFE flow frames, with incompressible components separated by Viton gaskets.

The packed bed hydrogenation reactor (2.2” length, 0.5” OD) was made from a stainless-steel tube with 5 wt % Pd/C (23 mg, 0.01 mmol, 1 mol%) retained using 1” of glass wool on each end. The anolyte solution, catholyte solution, and catalytic packed bed were prepared prior to operation. Two 24/40 rubber septa were punctured with a 14 gauge needle and Teflon tubing (1/8” ID and 3/16” OD) were threaded though the septa. This Teflon tubing was fitted with HPLC frits. To a

100 mL three-neck 24/40 round bottom flask with an oval stir bar was added AQS (78 mg, 0.25 mmol, 5 mol%), and Li_2CO_3 (554 mg, 7.50 mmol, 1.5 equiv.). Two of the openings were fitted with the septa fitted with the frits, the final opening was fitted with an unmodified 24/40 rubber septa. The flask was then transferred into a nitrogen filled glove box and LiBr (1.042 g, 12.00 mmol) and NMP (60 mL) were added, the heterogenous mixture was stirred for 20 min. The flask was removed from the glove box and placed under nitrogen atmosphere on a Schlenk line for 10 min. The Teflon tubing outlets were attached to Masterflex Pharmed tubing connected to the packed bed reactor (with HPLC pump) and flow cell (with peristaltic pump). H_2 gas was then vigorously bubbled through a 22-gauge needle into the solution to allow for hydrogen saturation of the solution. To a 8-dram vial fitted with a cross shaped stir bar was added $NiBr_2•3H_2O$ (136 mg, 10 mol%, 0.5 mmol), 4,4'-di-*tert*-butyl-2,2'-bipyridine (118 mg, 8.8 mol%, 0.44 mmol) and 4,4',4"-tri-*tert*-butyl-2,2',2"-terpyridine (44.2 mg, 2.2 mol%, 0.11 mmol), at this stage if the alkyl or aryl electrophile where solid they were added to the vessel. The vial was then transferred to a nitrogen filled glove box, LiBr (0.208 g, 2.4 mmol, 0.48 equiv) and NMP (12 mL) were added. The catholyte containing vial was then stirred for 10 min. The sealed vial was then removed from the glove box and placed under nitrogen atmosphere on a Schlenk line. Masterflex Pharmed tubing connected to the cathodic side of the Microflow cell where fed into the cathodic reservoir via 16-gauge needle (with peristaltic pump). The system was left to equilibrate under nitrogen/hydrogen purge for 10 min. In one flow loop, an HPLC pump flowed the anolyte at 4 mL min^{-1} through Teflon tubing and into the catalytic packed bed reactor. In the catalytic reactor, the AQS was reduced to $AQSH_2$ and the anolyte then flowed back into the reservoir. After 45 min, a second flow loop, which used a peristaltic pump to cycle anolyte and catholyte through the

electrochemical flow cell, was started. In ideality the $AQSH_2$ was oxidized on the carbon anode to form AQS and protons. The protons, separated from the proton exchange membrane by a PTFE screen, were carried back into the reservoir. Protons were prevented from accumulating by reaction with Li_2CO_3 in the anodic reservoir. On the cathode, nickel catalyzed reductive coupling was expected to take place.

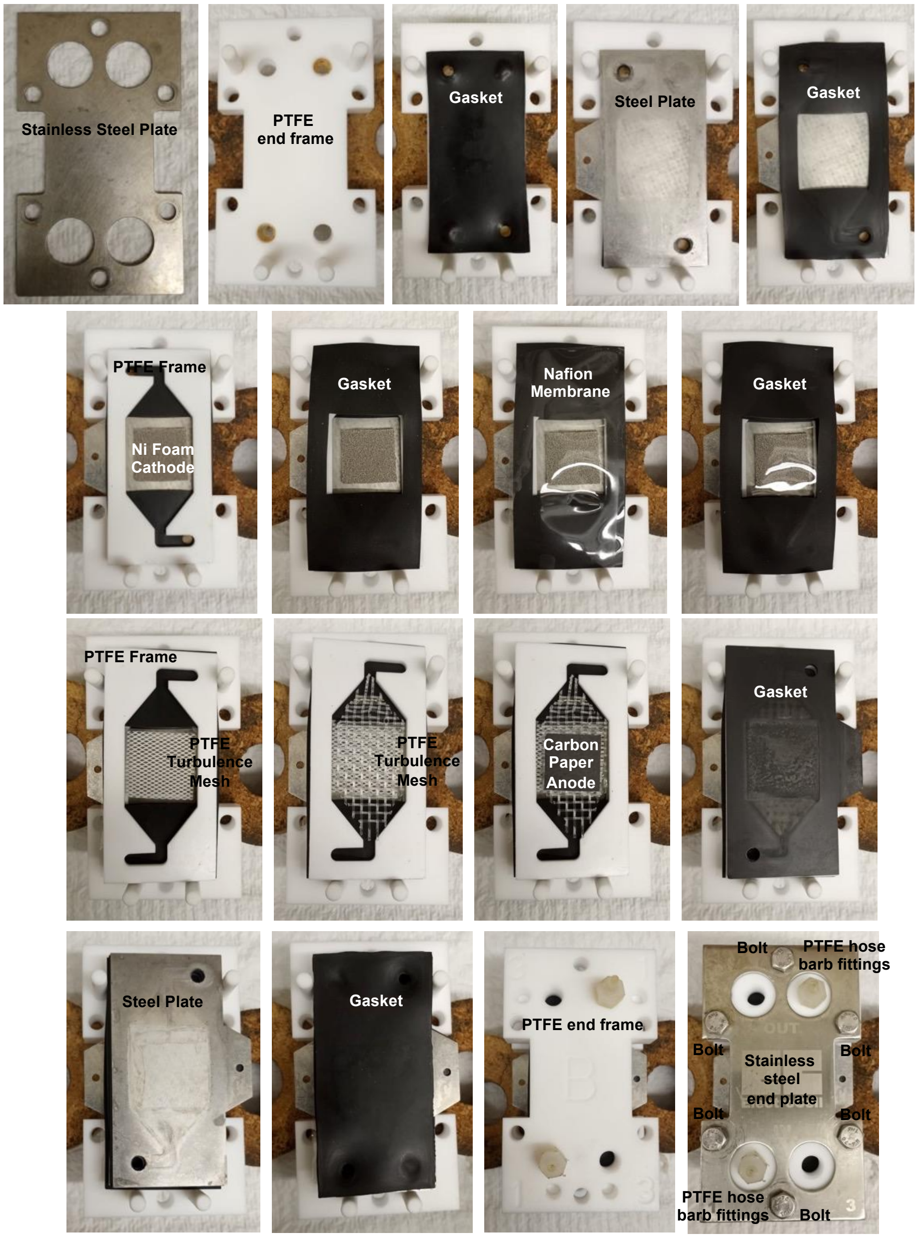

Figure 3.15: Photographs of the ElectroCell micro cell as it is assembled. Viton gaskets are used to separate solid components such as PTFE flow frames, turbulence mesh, and steel or graphite electrodes. PTFE and stainless steel end frames are pressed together with bolts to secure the assembly.

The flow cell was connected to a Biologic BP-300 potentiostat with the cathode selected as the working electrode and the anode as the counter electrode. A chronopotentiometry experiment was conducted with a constant current of –20 mA (current density = 4 mA cm^{-2}) until 3.5 F/mol were passed or until the cell potential dropped below –8 V. Upon completion of electrolysis the catholyte was collected and concentrated to dryness under high vacuum. The resultant residue was dissolved in EtOAc and passed through a small plug of silica to remove metal salts, concentrated to dryness, and purified by silica gel chromatography.

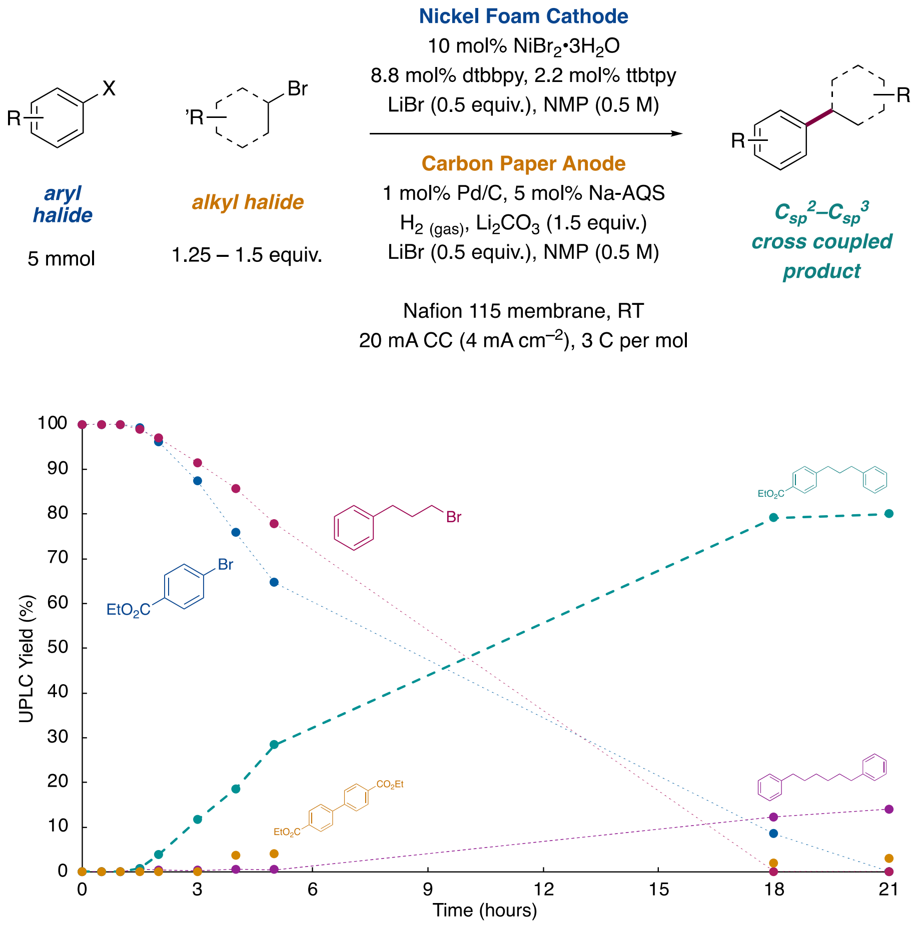

Figure 3.16: Time course data for the Ni-catalyzed cross electrophile coupling of 1-bromo-3-phenylpropane and ethyl-4-bromobenzoate under optimized conditions. 5 mA cm^{-2}, 0.5 M in ArBr substrate.

Figure 3.16 shows a representative synthesis, using the same substrate pair leveraged for batch screening. Aliquots analyzed over the course of the reaction show trends consistent with selective cross-coupling reactivity, and final product yields agree closely with those found in batch.

General Procedure for Ni XEC in the Large-Scale Flow Cell: An ElectroCell Syn Cell electrochemical flow cell was used as the flow apparatus (**Figure 3.17**). The flow cell consisted of a Nafion 117 cation exchange membrane, a 0.16 m^2 carbon felt anode distanced from the membrane with a PTFE screen, a 0.16 m^2 commercial nickel foam cathode directly against the membrane, and two polypropylene flow frames, with incompressible components separated by PTFE gaskets.

The anodic solution was prepared in a nitrogen filled glovebox by weighing sodium 9,10-dioxo-9,10-dihydroanthracene-2-sulfonate (AQS) into an 8-dram vial (7.69 g, 24.8 mmol, 5 mol%), LiBr into two 8-dram vials (2 × 52 g vials = 104 g, 1200 mmol, 2.4 equiv.). In a nitrogen filled glovebox, lithium carbonate (55 g, 744 mol, 1.5 equiv) was weighed into a 500 mL Nalgene container. AQS and 1 vial of LiBr were added to a 1 L Nalgene bottle fitted with a cross-shaped stir bar inside the glovebox. To a second 1 L Nalgene bottle fitted with a cross shaped stir bar was added the 2nd vial of LiBr. To each of the Nalgene bottles was added approximately 750 mL of anhydrous NMP from 2 × 1 L bottles. Each Nalgene bottle was mixed using rotary stirring for 1 h. On the day of reaction, the bottles were then removed from the glovebox, the stir bar was removed, and the contents were charged to the anolyte reservoir (12 L round bottom flask). The bottle was rinsed with remaining NMP (approx. 250 mL NMP per bottle). Dry NMP (1 L) was used to rinse the two Nalgene bottles. Lithium carbonate was added into the anodic reservoir to avoid accumulation of generated protons in solution. To retain the lithium carbonate, it was packaged into seven pouches made of filter paper sealed with polypropylene zip ties (approx. 7.9 g per pouch) for a total of 55 g of lithium carbonate charged. Finally, 3 L of NMP was added to the anolyte reservoir to bring the total volume to 6 L. The headspace was purged with N_2.

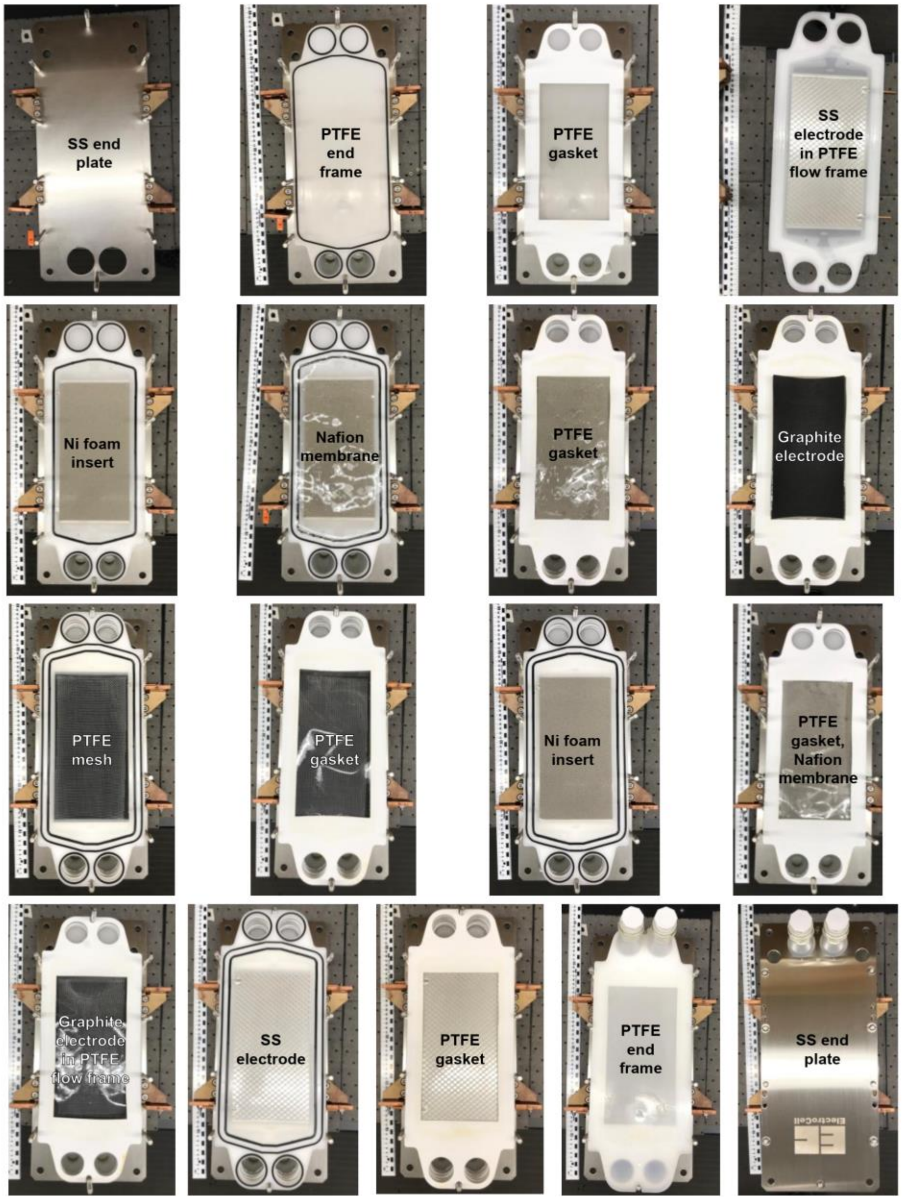

Figure 3.17: Photographs of the ElectroCell Syn Cell used for mediated H_2 anode synthesis of the cenerimod intermediate on 100 g scale.

The cathodic solution was prepared in a nitrogen glovebox. To separate 8-dram vials was weighed $NiBr_2$•glyme (1,2-dimethoxyethane)nickel dibromide (15.31 g, 49.6 mmol, 10 mol%), 4,4’-di-*tert*-

butyl-2,2’-bipyridine (8.79 g, 32.7 mmol, 6.6 mol%), 4,4’,4”-tri-tert-butyl-2,2’;6’,2”-terpyridine (8.76 g, 21.82 mmol, 4.4 mol%), and LiBr (52.1 g, 600 mmol, 1.2 equiv). These solids were transferred to a 1 L Nalgene bottle fitted with a cross shaped stir bar followed by 0.5 L of dry NMP. Methyl 2-chloro-6-methoxyisonicotinate (100 g, 496 mmol) was weighed into a 500 mL Nalgene bottle and then transferred into a second 1 L Nalgene bottle containing a stir bar inside the glovebox followed by 0.5 L of dry NMP. The contents of each were mixed using rotary stirring overnight, after which they were partially dissolved but not entirely homogeneous. On the day of the flow experiment, stir bars were removed and both solutions were charged to the catholyte reservoir (a 10 L glass vessel), every bottle was rinsed with 2 × 0.5 L NMP. Then, a solution of cyclopentyl bromide (111 g, 80 mL, 744 mmol, 1.5 equiv) in 0.25 L of NMP was added. Finally, 0.75 L of dry NMP was added to the reservoir to achieve the desired 3 L volume. The headspace was swept with N_2 (5 psi pressure) and the catholyte was mixed with overhead stirring for over 1 h (40 rpm), as a result a homogenous mixture was obtained and overhead stirring was ceased.

The packed bed hydrogenation reactor was composed of a Pd bed in a cylindrical stainless steel (SS) reactor. The SS reactor (0.5” OD, 9.5” height) was packed with 3 g of dry Pd/C (Evonik 5 wt %, lot# PMPC150388, catalyst type PMPC SP1010D, 1.4 mmol, 0.3 mol%) and secured with two SS disk frits (304 SS, 40 mesh). The Pd column was rinsed with NMP without return line to anolyte reservoir to remove any loose particulates and then the column outlet was plumbed into the anolyte reservoir return loop. All NMP was removed from both the anolyte and catholyte reservoirs and then Karl-Fischer titrations were performed to assess water content prior to charging reagents. (KF anolyte = 2 measurements: 4558 ppm, 4582 ppm; KF catholyte = 2 measurements: 1486 ppm, 1455 ppm). Anolyte and catholyte solutions were then charged and brought to the desired final volume (6 L anolyte, 3 L catholyte).

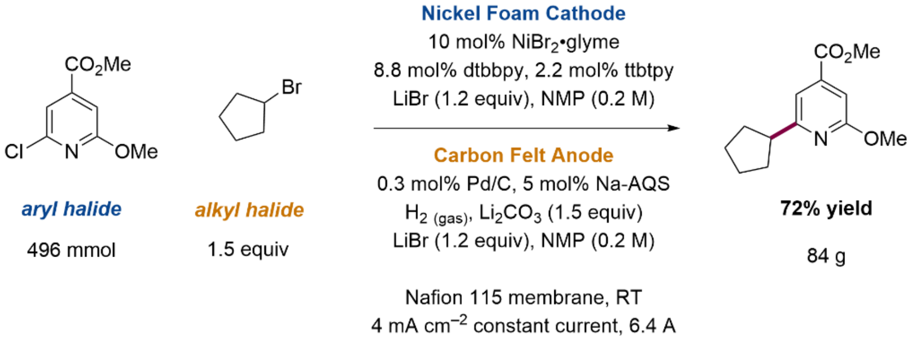

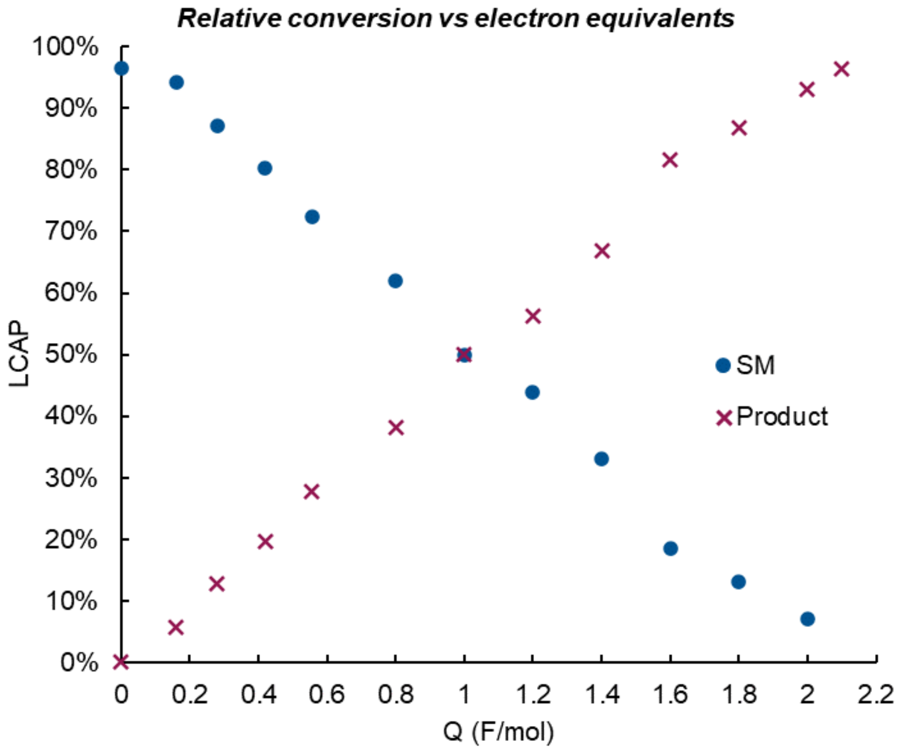

Figure 3.18: LCAP data of product and Ar–Cl SM from the 100 g scale synthesis of M29 as a function of supplied charge. LCAP was determined by integrating all SM related peaks and dividing the area of the product by that combined area.

Anolyte and catholyte solutions were pumped between the bed and the reservoir using a Masterflex Digital Gear Pump with pump head N25, while an N21 pump head was used for the hydrogenation reactor loop. Prior to electrolysis, the anolyte solution was pumped through the hydrogenation reactor at a rate of 0.5 L/min in co-flow with H_2 gas, which was controlled by an Alicat mass flow controller at 70 SCCM (roughly 70 cm^3 min^{-1}). The anolyte solution transitioned from yellow (fully oxidized) to green (partially or fully reduced). After pre-reduction of the anthraquinone species, the anolyte and catholyte were circulated through the cell at rates of 4.0 L/min. and a power supply was used to apply 6.4 A of constant current.

The reaction was monitored with bihourly analysis of cathodic aliquots by UPLC analysis (**Figure 3.18**) and the liquid chromatography area percent (LCAP) of the substrate and product were used to roughly monitor degree of reaction. When the reaction reached the cutoff cell voltage of 3 V after just under four hours, the experiment was stopped. The final product assay was conducted by quantitative-^{1}H-NMR in triplicate and showed 72% assay yield.

References

---

1. Brown, D. G.; Boström, J. Analysis of Past and Present Synthetic Methodologies on Medicinal Chemistry: Where Have All the New Reactions Gone? *J. Med. Chem.* **2016**, *59*, 4443–4458. DOI: 10.1021/acs.jmedchem.5b01409.

2. Buskes, M. J.; Blanco, M.-J. Impact of Cross-Coupling Reactions in Drug Discovery and Development. *Molecules* **2020**, *25*, 3493. DOI: 10.3390/molecules25153493.

3. Frisch, A. C.; Beller, M. Catalysts for Cross-Coupling Reactions with Non-Activated Alkyl Halides. *Angew. Chem. Int. Ed.* **2005**, *44*, 674–688. DOI: 10.1002/anie.200461432.

4. Weix, D. J. Methods and Mechanisms for Cross-Electrophile Coupling of Csp(2) Halides with Alkyl Electrophiles. *Acc. Chem. Res.* **2015**, *48*, 1767–1775. DOI: 10.1021/acs.accounts.5b00057.

5. Conan, A.; Sibille, S.; d'Incan, E.; Périchon, J. Nickel-Catalysed Electroreductive Coupling of α-Halogenoesters with Aryl or Vinyl Halides. *J. Chem. Soc. Chem. Commun.* **1990**, *1*, 48–49. DOI: 10.1039/c39900000048.

6. Everson, D. A.; Shrestha, R.; Weix, D. J. Nickel-Catalyzed Reductive Cross-Coupling of Aryl Halides with Alkyl Halides. *J. Am. Chem. Soc.* **2010**, *132*, 920-921. DOI: 10.1021/ja9093956

7. Everson, D. A.; Weix, D. J. Cross-Electrophile Coupling: Principles of Reactivity and Selectivity. *J. Org. Chem.* **2014**, *79*, 4793-4798. DOI: 10.1021/jo500507s

---

8. Goldfogel, M. J.; Huang, L.; Weix, D. J. Cross‐electrophile Coupling: Principles and New Reactions. *Nickel Catalysis in Organic Synthesis*. Wiley January 28, 2020, pp 183−222. DOI: 10.1002/9783527813827.ch9.

9. Kang, K.; Loud, N. L.; DiBenedetto, T. A.; Weix, D. J. A General, Multimetallic Cross-Ullmann Biheteroaryl Synthesis from Heteroaryl Halides and Heteroaryl Triflates. *J. Am. Chem. Soc.* **2021**, *143*, 21484–21491. DOI: 10.1021/jacs.1c10907.

10. Perkins, R. J.; Hughes, A. J.; Weix, D. J.; Hansen, E. C. Metal-Reductant-Free Electrochemical Nickel-Catalyzed Couplings of Aryl and Alkyl Bromides in Acetonitrile. *Org. Process Res. Dev.* **2019**, *23*, 1746-1751. DOI: 10.1021/acs.oprd.9b00232

11. Everson, D. A.; George, D. T.; Weix, D. J.; Buergler, J. F.; Wood, J. L. Nickel-Catalyzed Cross-Coupling of Aryl Halides with Alkyl Halides: Ethyl 4-(4-(4-methylphenylsulfonamido)-phenyl)butanoate. *Org. Synth.* **2013**, *90*, 200-214. DOI: 10.15227/orgsyn.090.0200

12. Acemoglu, M.; Baenziger, M.; Krell, C. M.; Marterer, W. Experiences with Negishi Couplings on Technical Scale in Early Development. In *Transition Metal-Catalyzed Couplings in Process Chemistry*, Magano, J.; Dunetz, J. R., Eds. Wiley-VCH: Weinheim, 2013; pp 15-23.

13. Li, H.; Breen, C. P.; Seo, H.; Jamison, T. F.; Fang, Y.-Q.; Bio, M. M. Ni-Catalyzed Electrochemical Decarboxylative C–C Couplings in Batch and Continuous Flow. *Org. Lett.* **2018**, *20*, 1338-1341. DOI: 10.1021/acs.orglett.8b00070

---

14. Hansen, E. C.; Li, C.; Yang, S.; Pedro, D.; Weix, D. J. Coupling of Challenging Heteroaryl Halides with Alkyl Halides via Nickel-Catalyzed Cross-Electrophile Coupling. *J. Org. Chem.* **2017**, *82,* 7085-7092. DOI: 10.1021/acs.joc.7b01334

15. Charboneau, D. J.; Huang, H.; Barth, E. L.; Germe, C. C.; Hazari, N.; Mercado, B. Q.; Uehling, M. R.; Zultanski, S. L. Tunable and Practical Homogeneous Organic Reductants for Cross-Electrophile Coupling. *J. Am. Chem. Soc.* **2021**, *143*, 21024–21036. DOI: 10.1021/jacs.1c10932.

16. Perkins, R. J.; Pedro, D. J.; Hansen, E. C. Electrochemical Nickel Catalysis for Sp2-Sp3 Cross-Electrophile Coupling Reactions of Unactivated Alkyl Halides. *Org. Lett.* **2017**, *19*, 3755–3758. DOI: 10.1021/acs.orglett.7b01598.

17. Truesdell, B. L.; Hamby, T. B.; Sevov, C. S. General C(Sp2)-C(Sp3) Cross-Electrophile Coupling Reactions Enabled by Overcharge Protection of Homogeneous Electrocatalysts. *J. Am. Chem. Soc.* **2020**, *142*, 5884–5893. DOI: 10.1021/jacs.0c01475.

18. Hamby, T. B.; LaLama, M. J.; Sevov, C. S. Controlling Ni Redox States by Dynamic Ligand Exchange for Electroreductive Csp3-Csp2 Coupling. *Science* **2022**, *376*, 410–416. DOI: 10.1126/science.abo0039.

19. Jiao, K.; Xuan, J.; Du, Q.; Bao, Z.; Xie, B.; Wang, B.; Zhao, Y.; Fan, L.; Wang, H.; Hou, Z.; Huo, S.; Brandon, N. P.; Yin, Y.; Guiver, M. D. Designing the next Generation of Proton-Exchange Membrane Fuel Cells. *Nature* **2021**, 595, 361–369. DOI: 10.1038/s41586-021-03482-7.

20. Barrette, W. C.; Sawyer, D. T. Determination of Dissolved Hydrogen and Effects of Media and Electrode Materials on the Electrochemical Oxidation of Molecular Hydrogen. *Anal. Chem.* **1984**, *56*, 653–657. DOI: 10.1021/ac00268a015.

21. Lazouski, N.; Chung, M.; Williams, K.; Gala, M. L.; Manthiram, K. Non-Aqueous Gas Diffusion Electrodes for Rapid Ammonia Synthesis from Nitrogen and Water-Splitting-Derived Hydrogen. *Nat. Catal.* **2020**, *3*, 463–469. DOI: 10.1038/s41929-020-0455-8.

22. Hodgetts, R. Y.; Du, H.-L.; Nguyen, T. D.; MacFarlane, D.; Simonov, A. N. Electrocatalytic Oxidation of Hydrogen as an Anode Reaction for the Li-Mediated N2 Reduction to Ammonia. *ACS Catal.* **2022**, *12*, 5231–5246. DOI: 10.1021/acscatal.2c00538.

23. Anson, C. W.; Stahl, S. S. Mediated Fuel Cells: Soluble Redox Mediators and Their Applications to Electrochemical Reduction of O2 and Oxidation of H2, Alcohols, Biomass, and Complex Fuels. *Chem. Rev.* **2020**, *120*, 3749–3786. DOI: 10.1021/acs.chemrev.9b00717

24. Preger, Y.; Gerken, J. B.; Biswas, S.; Anson, C. W.; Johnson, M. R.; Root, T. W.; Stahl, S. S. Quinone-Mediated Electrochemical O2 Reduction Accessing High Power Density with an Off-Electrode Co- N/C Catalyst. *Joule* **2018**, *2*, 2722−2731. DOI: 10.1016/j.joule.2018.09.010

25. Preger, Y; Johnson, M. R.; Biswas, S; Anson, C; Root, T. W.; Stahl, S. S. Anthraquinone-Mediated Fuel Cell Anode with an Off-Electrode Heterogeneous Catalyst Accessing High Power Density When Paired with a Mediated Cathode. *ACS Energy Letters* **2020**, *5*, 1407–1412. DOI: 10.1021/acsenergylett.0c00631

26. Franke, M. C.; Longley, V. R.; Rafiee, M.; Stahl, S. S.; Hansen, E. C.; Weix, D. J. Zinc-Free, Scalable Reductive Cross-Electrophile Coupling Driven by Electrochemistry in an Undivided Cell. *ACS Catal.* **2022**, 12617–12626. DOI: 10.1021/acscatal.2c03033

---

27. A. L. Aguirre, N. L. Loud, K. A. Johnson, D. J. Weix, Y. Wang, ChemBead Enabled High-Throughput Cross-Electrophile Coupling Reveals a New Complementary Ligand. Chem.–Eur. J. **2021**, *27*, 12981-12986. DOI: 10.1002/chem.202102347

28. J. A. Zamora Zeledón, A. Jackson, M. B. Stevens, G. A. Kamat, T. F. Jaramillo, Methods - a practical approach to the reversible hydrogen electrode scale. *J. Electrochem. Soc*. **2022**, *169*, 066505.

29. Campos-Martin, J. M.; Blanco-Brieva, G.; Fierro, J. L. G. Hydrogen Peroxide Synthesis: An Outlook beyond the Anthraquinone Process. *Angew. Chem. Int. Ed.* **2006**, *45*, 6962–6984. DOI: 10.1002/anie.200503779

Chapter 4

Heterogeneous M-N-C Catalysts: Review of Known Aerobic Oxidations and Synthetic Efforts to Adopt Catalysts from Fuel Cells for Mediators

Some of the content in this chapter has been published. A credit statement is provided below to clarify this author's contributions.

The review of aerobic oxidations is adapted from section 3 of the associated article. Johnson wrote the text of that section with contributions from Khamespanah. Bates provided excellent, detailed advice and heavy initial edits. All authors edited the final version of the text. The introductory paragraphs are also drawn from the article; they were written by Bates with contributions from Johnson and edited by all authors.

Jason S. Bates, Mathew R. Johnson, Fatemeh Khamespanah, Thatcher W. Root, Shannon S. Stahl. Heterogeneous M-N-C Catalysts for Aerobic Oxidation Reactions: Lessons from Oxygen Reduction Electrocatalysts. *Chem. Rev.* **2022**. *XX*, XX-XX. DOI: 10.1021/acs.chemrev.2c00424

Abstract

Heterogeneous catalysts are a critical component of every mediated electrochemical flow system discussed in this dissertation. They enable appreciable rates of substrate consumption, either directly at the electrode (e.g., Pt/C allowing gaseous hydrogen to be oxidized on an MEA) or in conjunction with a mediator (e.g., Pd/C allowing gaseous hydrogen to reduce an anthraquinone for a separate on-electrode reaction). These systems primarily make use of supported Pt or Pd catalysts, leveraging their versatility and generally high activity. For reasons of cost and scalability, however, the use of non-PGM metals is preferred where possible. In **Section 2.1**, we demonstrated that this was feasible with M-N-Cs in mediated fuel cells, using an Fe-based M-N-C to effect the aerobic oxidation of the t-MPSNa hydroquinone, regenerating the corresponding quinone for electrochemical reduction at the fuel cell's cathode cathode. M-N-C catalysts can be used for aerobic oxidations in organic media as well, providing another area of mutual advantage with molecular mediators, which can be used to sidestep reactions which prove challenging in organic solvent (e.g., HOR). Given this promising overlap, there is a compelling interest in better understanding the capabilities of this class of materials for aerobic oxidative catalysis.

This chapter defines and describes M-N-C materials, reviews their documented uses for the aerobic oxidation of organic molecules, and briefly summarizes some early efforts to translate M-N-C catalysts from applications in fuel cell cathodes to the oxidation of cathodic fuel cell mediators.

Introduction

Materials composed of metal ions integrated within nitrogen-doped carbon (M-N-Cs) are a class of "single-atom" catalysts[1,2] that have received extensive attention for the electrochemical oxygen reduction reaction (ORR) in fuel cells.[3–13] These catalysts often feature first-row transition-metal ions, such as iron and cobalt, and offer a compelling alternative to catalysts derived from platinum or other precious metals. Recent studies show that M-N-C catalysts are effective for many other applications, including CO_2 electroreduction,[14, 15] N_2 electroreduction,[16] and a variety of reductions[17–20] and oxidations[21] of organic molecules. The electrochemical ORR is closely related to aerobic oxidation reactions, as both reaction classes lead to the net reduction of O_2 to water using electrons and protons from a complementary electrochemical oxidation reaction (in the case of ORR) or from an organic molecule (for aerobic oxidation) (**Figure 4.1**). It is the premise of this chapter that advances in M-N-C catalysts for electrochemical ORR provide a foundation for future advances in aerobic oxidation catalysis.

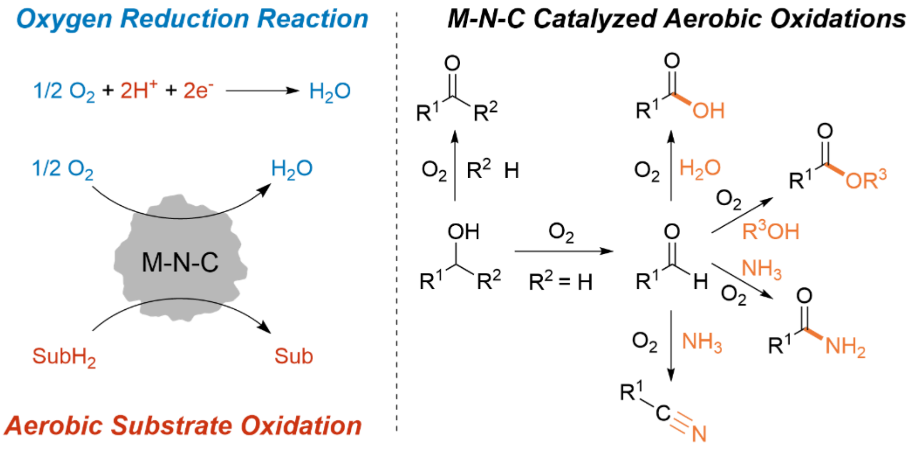

Figure 4.1: O_2 accepts protons and electrons in the oxygen reduction reaction and aerobic oxidation catalysis (left). In the latter case, the protons and electrons derive from the bonds of molecules ($SubH_2$), such as the O–H and C–H bonds of alcohols (right).

Aerobic oxidation reactions using M-N-C catalysts include the conversion of alcohols to aldehydes and ketones and oxidative coupling of primary alcohols with various partners to yield carboxylic acids, esters, and nitriles (**Figure 4.1**).[21] Many of these transformations have been developed by using empirical approaches to identify the preferred catalyst and optimize the reactions. The applications are still somewhat limited relative to reactions that employ noble metal heterogeneous catalysts[22–25] and homogeneous catalysts,[26–30] however, at least partly reflecting the common

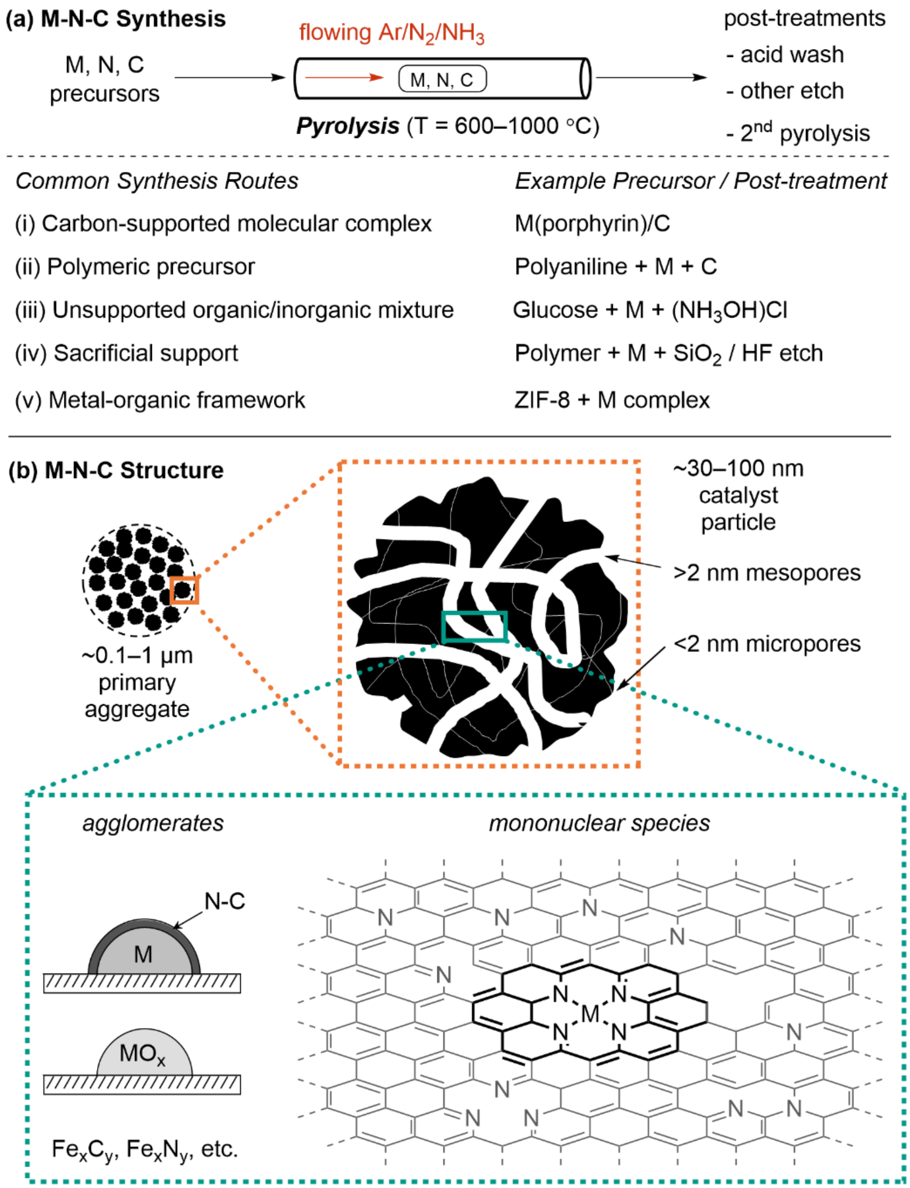

Figure 4.2: Overview of A. synthetic methods and B. structural features of M-N-C catalysts.

requirement for high reaction temperatures, high O_2 pressures, and/or long reaction times. A deeper understanding of the active sites in the M-N-C catalysts and the associated reaction mechanisms could play an important role in addressing these limitations. Uncovering the relationships between active-site structure and catalyst performance will require advances in structural characterization of the catalysts and quantitative studies of reaction kinetics. To date, few M-N-C-catalyzed aerobic oxidation reactions have been analyzed in this manner.

M-N-C catalysts are prepared by various pyrolysis-based synthetic routes (**Figure 4.2 A**). These methods are reviewed in detail elsewhere,[9,11] but the following overview provides important context for the content in this chapter. In most cases, a precursor mixture containing sources of the M, N, and C components is treated at temperatures of ~600–1000 °C under a flow of either an inert gas, such as Ar or N_2, or a reactive gas, such as NH_3 or H_2. Some components of the precursor mixtures decompose and/or volatilize during this pyrolysis treatment, while others form carbon-based solids with varying degrees of graphitization and nitrogen incorporation. The metal ions either integrate within specific mononuclear binding sites in the nitrogen-doped carbon support[31] or aggregate to form nanoparticles (e.g., metallic Fe, FeO_x, Fe_xC_y, Fe_xN_y, etc.). The resulting pyrolyzed M-N-C solids feature mesoporous and/or microporous voids that regulate substrate access to active sites within them (**Figure 4.2 B**). The structures of precursors and pyrolysis conditions, including the temperature, duration, spatial concentration gradients, and gas environment, influence the physicochemical properties of the catalyst, including the prevalence of N dopants and structural defects within the carbon, the speciation of metals as nanoparticles or single atoms, and the porosity of the material. Post-synthetic treatments are sometimes carried out with the intent to modify these properties. For example, metal aggregates may be removed by acid washing. The widely used pyrolysis-based synthesis routes may be grouped into four categories, defined according to the choice of precursors and/or post-synthetic treatments (**Figure 4.2 A**): (i) carbon-supported molecular complexes (e.g., Co(porphyrin)/C[3], Fe(Phen)$_3$/C[32]), (ii) polymeric precursors (e.g., polyacrylonitrile,[33] polyaniline[34]), (iii) unsupported organic mixtures (e.g., glucose, metal, and (NH$_3$OH)Cl[35]), (iv) sacrificial supports[36] that template mesopores after they are leached from the M-N-C (e.g., Fe-poly(ethyleneimine)-SiO$_2$ followed by HF etch after pyrolysis[37]), and (v) decomposition of metal–organic frameworks (e.g., Fe(Phen)-impregnated ZIF-8[38], Fe-doped ZIF-8[39]). The structural diversity of M-N-Cs that results from these synthetic routes requires further structural characterization to link the local structures of active centers to their kinetic function.

The remainder of this chapter will first provide a comprehensive summary of the scope of aerobic oxidation reactions catalyzed by earth-abundant M-N-Cs. The intrinsic kinetic behavior, quantities of and structures of active centers responsible for aerobic oxidations are less well understood than they are in the ORR field. This observation provides the inspiration for a brief results section, in which early-stage efforts are made to adapt M-N-C materials from the fuel cell literature for the oxidation of t-MPSNa quinone, a cathodic mediator in mediated fuel cells.

Review of M-N-Cs for Aerobic Oxidation of Organic Molecules

This section outlines the scope of aerobic oxidations catalyzed by M-N-C materials, starting with alcohol oxidation and oxidative coupling reactions and then addressing other oxidative dehydrogenation and coupling reactions. For each reaction class, we document the scope of reactivity, summarize any catalyst structural characterization provided, and, to the extent possible, assess relevant reactivity metrics and kinetic and mechanistic studies. Catalyst source materials and salient details of the synthetic methods will be presented in the text; however, catalysts will then be abbreviated with the notation “M-N-C(i/ii/iii/iv/v)” in figures, with the value i–v referring to the relevant synthetic approach noted in **Figure 4.2 A**. References to catalyst loadings in the different reactions reflect common usage by organic chemists, where "mol%" refers of total metal loading with respect to limiting reagent or substrate. It is acknowledged that this value represents an upper bound, as the fraction of catalytically relevant active centers per total metal is almost always less than unity. More rigorous active site densities have not been quantified for most of the systems outlined in this section.

Alcohol Oxidation to Aldehydes and Ketones

Oxidation of alcohols to aldehydes and ketones over M-N-C catalysts has been demonstrated for benzylic and simple aliphatic substrates. Li and coworkers[40] reported the oxidation of alcohols in 2016 over a Co-N-C(v) catalyst derived from the pyrolysis of a Co-carboxylate/triazine metal–organic framework. Substrates were oxidized under air in aqueous solvent without added base and required high catalyst loading (10 mol%), long reaction time (48 h), and high temperature (110 °C). Primary, secondary, and benzylic aldehydes and ketones were synthesized with GC-MS yields of 85–98%, whereas allylic and aliphatic ketones were afforded in 59–72% yields in 60 h reaction times (**Figure 4.3 A**). A similar scope of reactivity has been achieved without added base using Co-N-C(i) catalysts synthesized with either 1-Butyl-3-methylimidazolium bromide[41] or 1-methyl-3-cyanomethyl-1H-imidazolium chloride [42] as additives. Xu and coworkers [43] used a benzimidazole-derived Co-N-C(v) to expand the scope to include methoxy-functionalized benzylic substrates but required exogenous base. The broadest scope of aldehyde and ketone synthesis using exogenous base was reported in 2022 by Beller and coworkers[44] over a Co-N-C(i) catalyst synthesized with piperazine and tartaric acid. This method required lower temperature (80 °C), catalyst loading (6.5 mol% Co), and reaction time (24 h) than base-free methodologies.

Substituted aromatic and heterocyclic aldehydes and ketones containing a variety of pharmaceutically relevant functional groups could be synthesized with yields ≥75% (**Figure 4.3 B**). The same catalyst was competent for a variety of other aerobic oxidations that further functionalize the aldehyde (*vide infra*). Base-free methodologies for aldehyde and ketone synthesis have yet to reach comparable scope or reactivity compared with those that use exogenous base.

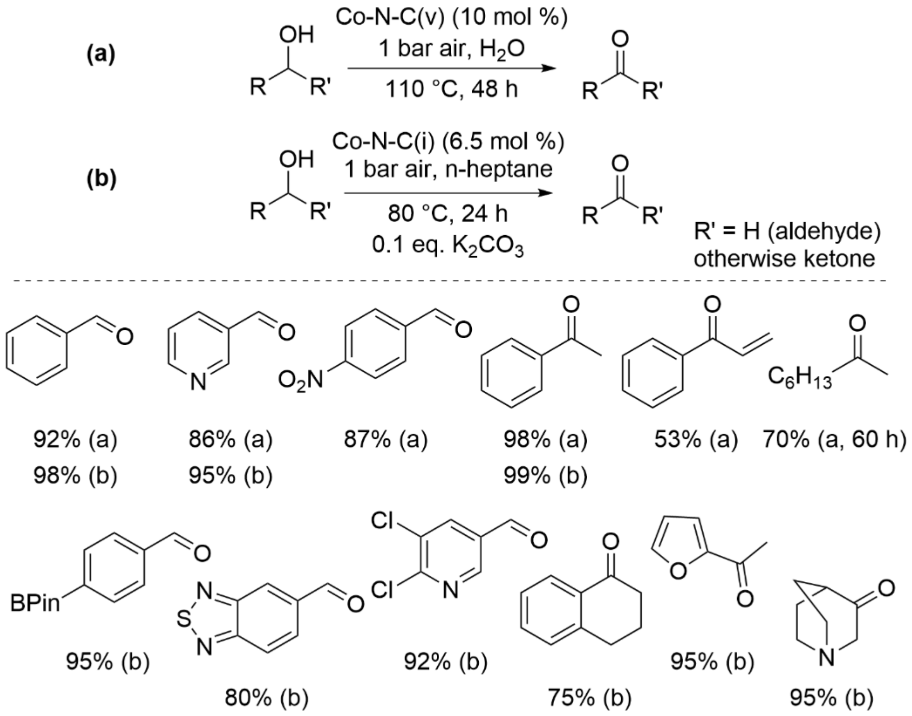

Figure 4.3: Aerobic oxidation of alcohols to aldehydes and ketones A. without exogenous base,[40] and… B. with exogenous base.[44] Percentages reflect yield of the specified product.

Some structural information has been provided for M-N-C alcohol oxidation catalysts. Li and coworkers[40] detected ~10 nm metallic Co nanoparticles using transmission electron microscopy (TEM) and X-ray diffraction (XRD), some of which were encapsulated within graphitic shells, whereas an N-free analog had particles ~100 nm in size and gave lower yields. Beller and coworkers[44] similarly identified metallic Co nanoparticles encapsulated by N-doped graphitic shells and observed lower yields using a catalyst containing CoO_x. These data point toward the importance of N-doping and Co but were not able to discriminate whether CoN_x or Co aggregates were the active centers. The Co-N-C(v) catalyst studied by Li and coworkers[40] showed qualitatively more types of basic sites than the N-free analog, inferred by the presence of additional peaks in its CO_2 temperature-programmed desorption (TPD) profile. The authors speculated that these basic sites facilitated reactivity without added base. Quantitative characterizations of the active sites were not attempted in these studies. Davis and coworkers[45] studied M-N-C(i) (M = Co, Cu) synthesized using 1,10-phenanthroline (Phen) as a nitrogen source that was proposed to have atomically dispersed MN_x species on the basis of X-ray absorption spectroscopy (XAS) and scanning transmission electron microscopy (STEM) data. The rate of aqueous benzyl alcohol oxidation to benzaldehyde (per g, 80 °C, 0.05 M alcohol, 10 bar O_2, 0.1 M NaOH) was unaffected by an acid washing treatment that removed nanoparticles from Co-N-C, suggesting that CoN_x are the active sites for alcohol oxidation.

The kinetics of alcohol oxidation have been studied more broadly than most aerobic oxidations catalyzed by M-N-Cs. Because active-site densities have not been directly quantified, rates are typically reported and/or available only as quantities normalized with respect to the total M content. These values represent a lower bound for the turnover frequency (TOF) because they assume that all metal atoms are catalytically active. Davis and coworkers[46] compared the rates of aqueous benzyl alcohol oxidation to benzaldehyde over M-N-C(iv) (M = Co, Cr, Fe, Ni, Cu). Normalized rate values (per total M, 80 °C, 0.05 M alcohol, 10 bar O_2) were between $0.08–3.4\times10^{-2}$ mol (mol M)$^{-1}$ s^{-1} and were higher on Cu-N-C and Co-N-C than on the other catalysts by factors of ≥5 (Cu) and ≥2 (Co). Catalysts reused after 8 h of reaction had 40–90% lower rates, which could be recovered to different extents by treatment in flowing H_2 at 300 °C for 3 h (Co = 74% recovery, Cu = 15% recovery, Fe ~ 100% recovery). The addition of 2,2,6,6-tetramethylpiperidine *N*-oxyl (TEMPO, 2 mol% relative to substrate) increased the rate over Fe-N-C by a factor of five. Zhang, Hu, and coworkers[47] measured a similar normalized rate (3.5×10^{-2} mol (mol Co)$^{-1}$ s^{-1}) of benzyl alcohol oxidation to benzaldehyde under different conditions (90 °C, n-heptane solvent, 0.2 M alcohol, 1 bar O_2) on a Co-N-C(iii) catalyst. Li et al.[48] measured the rate of oxidation of cinnamyl alcohol to cinnamaldehyde in n-octane solvent (100 °C, 1 atm of O_2) using a Cu-N-C(v) catalyst synthesized from a Cu-doped ZIF-8 MOF (ZIF = zeolitic imidazolate framework; MOF = metal organic framework). This corresponded to a normalized rate of 2 mol (mol Cu)$^{-1}$ s^{-1}. The different reaction conditions used in each of these studies together with the lack of active site quantitation prevent direct comparison of catalyst performance.

Mechanistic hypotheses for alcohol oxidation have been developed using kinetic isotope effect and reaction order measurements. Davis and coworkers[46] reported H/D kinetic isotope effect values for aerobic oxidation of $C_6H_5CD_2OH$ substrates (80 °C, 0.05 M alcohol, 10 bar O_2) of 4.8 and 2.2 for Fe-N-C(iv) and Cu-N-C(iv), respectively, to conclude that β-H elimination is a kinetically relevant step. The rate was zero-order in alcohol (0.025–0.1 M) on both Cu-N-C(iv) and Fe-N-C(iv). The rate was zero-order in O_2 on Fe-N-C(iv) (3–20 bar), whereas the order in O_2 transitioned from ~0.7 (3–10 bar) to zero-order at higher O_2 pressures (10–20 bar) on Cu-N-C(iv). The authors concluded that the catalyst surface was saturated with both O_2 and alcohol but did not propose a sequence of elementary steps to describe the mechanism. Zhang, Hu, and coworkers[47] reported that the rate of aerobic benzyl alcohol oxidation (90 °C) on Co-N-C(iii) in heptane solvent was ~0.5-order in O_2 (1–12 bar) and zero-order at higher O_2 pressures (12–36 bar), consistent with the rate data of Davis and coworkers.[46] In contrast, benzyl alcohol inhibited reaction rates (-0.3 order, 0.05–0.75 M, 2 bar O_2; -0.5 order, 0.2–3.9 M, 12 bar O_2), as did benzaldehyde (-0.4 order, 0.05–0.4 M, 0.01 M alcohol, 2 bar O_2) and H_2O (-0.5 order, 0.02–0.06 M, 0.01 M alcohol, 2 bar O_2).[47] The authors proposed a two-site mechanism wherein displacement of O_2 at the metal center by competitive adsorption of benzyl alcohol leads to the observed inhibition.

Alcohol Oxidation to Carboxylic Acids

Beller and coworkers[44] used H_2O as a reactant and solvent to support oxidation of primary alcohols to the corresponding carboxylic acids using the same Co-N-C(i) catalyst noted above (cf. **Figure 4.3 B**). More demanding reaction conditions were used, including higher temperature (110 °C), higher pressure (10 bar air), and 0.5 equivalents of KOH. A variety of substituted benzoic acids, including heterocycles, could be synthesized using this method (**Figure 4.4**). Rate data under well-defined conditions were not reported.

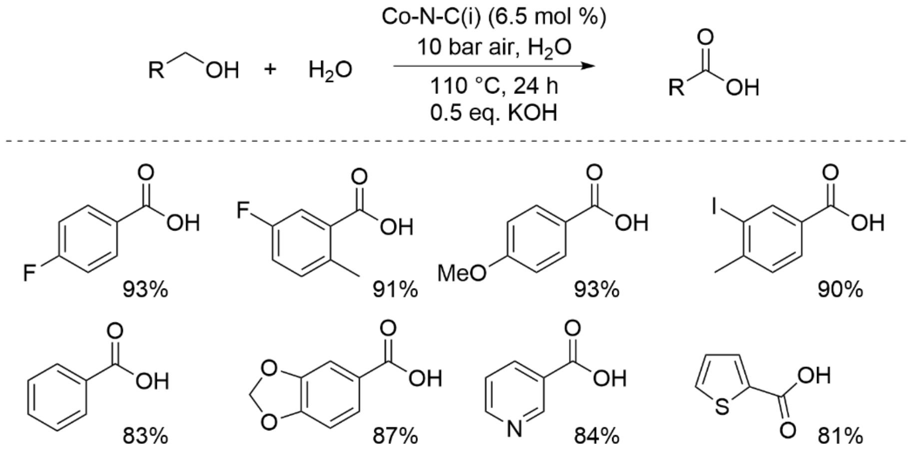

Figure 4.4: Oxidation of alcohols to carboxylic acids over M-N-C.[44] Percentages reflect yield of the specified product.

Alcohol Oxidation to Esters

Aldehydes generated by alcohol oxidation can be oxidatively coupled with alcohols to generate ester products. Beller and coworkers[49] reported alcohol esterification in 2013 using a Co-N-C(i) material synthesized using a carbon-supported Co(Phen)$_2$ precursor. Benzylic, heterobenzylic, and allylic alcohols were aerobically cross esterified with methanol, which also served as the solvent. Substrates included those with functional groups such as halides, alkyl groups, ethers, and thioethers, and afforded methyl esters in yields of $\geq$80%. Longer-chain primary alcohol partners (C_2–C_6) were cross coupled with benzylic alcohols and homocoupled in *n*-heptane. In 2017, Huang and coworkers[42] reported the methyl esterification of substituted benzyl alcohols using a Co-N-C(i) synthesized with a 1-methyl-3-cyanomethyl-1H-imidazolium chloride additive at lower temperatures (60 °C) but with a scope that lacked difficult substrates like S-containing molecules and coupling partners other than methanol. In 2022, Beller and coworkers[44] reported ester synthesis over a Co-N-C(i) catalyst synthesized with piperazine and tartaric acid ligands with a scope similar to their original report[49] but at lower temperature (55 °C), in air, and with lower base loading (0.1 eq., (**Figure 4.5**). Other studies extended this method using similar M-N-C catalysts to synthesize lactones from diols[50] and to oxidize biomass-derived furfural and 5-hydroxymethylfurfural.[51,52,53] Reaction conditions were also developed to eliminate the use of exogenous base, albeit with more limited synthetic scope, by using catalysts such as Co-N-C(v) derived from the Co-imidazolate MOF ZIF-67[50] and Co-N-C(i) using graphitic carbon nitride (g-C_3N_4) instead of carbon as a support for Co coordinated with 1,4-benzenedicarboxylic acid and triethylenediamine.[54]

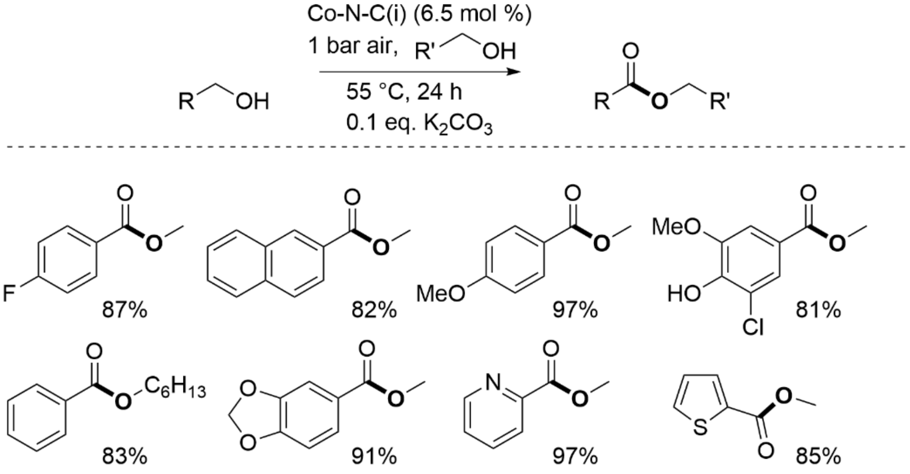

Figure 4.5: Oxidative alcohol coupling to form esters.[44] Percentages reflect yield of the specified product.

The structures and reactivity of M-N-C catalysts for esterification have been characterized to varying extents. In their initial report, Beller and coworkers[49] detected Co, CoO, and Co_3O_4 phases by XRD, and concluded that the surfaces of the particles were enriched in Co_3O_4 by STEM and EDS analysis, whereas only metallic Co particles with N-doped graphitic shells were detected in their later report.[44] In these studies cases, atomically dispersed CoN_x species were not considered as an alternative. Co appears to be privileged for this reactivity on the basis of screening studies, which evaluated benzyl alcohol methyl esterification over a range of M-N-C(iv) catalysts[55] (M = Co, Fe, Cu, V, Cr, Ni, Mn) and M-N-C(i) catalysts[44] (M = Fe, Mn, Co Cu). Co-N-C catalysts competent for esterification have been synthesized by a variety of methods noted in **Figure 4.2 A**, including (i),[42,44,49,51,54] (ii),[56] (iii),[57,58] (iv),[55] and (v).[50,53,59] These studies have observed CoO_x nanoparticles,[42,49,51,56,59] metallic Co nanoparticles[42,56,59] (often with N-C shells[44,49,50,53,54,58]), and an absence of large metal aggregates that suggests the presence of mononuclear CoN_x species.[55,57] Quantitative relationships between active site structures and reactivity have not been established.

Normalized rates (per total Co, 60 °C, 1 bar O_2) for the methyl esterification of benzyl alcohol are higher under conditions with added base. Among the three catalysts that have been tested in the presence and absence of base,[49,54,55] the Co-N-C(iv) of Gao and coworkers has the highest normalized rate with added base (9×10^{-2} mol (mol Co)$^{-1}$ s^{-1}),[552] whereas the Co-N-C(i) of Li et al. has the highest normalized rate in the absence of exogenous base (2×10^{-3} mol (mol Co)$^{-1}$ s^{-1}).[54] That the optimal catalyst is different in the presence and absence of base implicates mechanistic distinctions that have not yet been elucidated. Mechanistic pathways involving the oxidation of alcohol to aldehyde followed by hemiacetal formation and oxidation to the ester were proposed based on analogy with known homogeneous chemistry[49] and the observation of aldehydes as byproducts.[50] Some studies[44,53,54,57] have suggested that a surface-bound superoxide radical anion is involved based on lower yields in the presence of the free-radical scavenger butylated hydroxytoluene and EPR signals for 5,5-dimethyl-1-pyrroline *N*-oxide after radical capture; however, this evidence shows only the formation of radical species but not their abundance or catalytic relevance. The dearth of well-defined rate data and limited mechanistic understanding of the elementary steps involved in catalysis hamper the development of structure-reactivity relationships for esterification with M-N-C catalysts.

Alcohol Oxidation to Nitriles

Aldehydes generated by alcohol oxidation can be oxidatively coupled with ammonia to generate nitrile products. Beller and coworkers[60] reported nitrile synthesis using M-N-C(i) catalysts (M = Co, Fe) synthesized using $Co(Phen)_2$ and $Fe(Phen)_3$ precursors (**Figure 4.6a**). The two catalysts afforded similar yields for most nitriles, but Fe required a slightly higher catalyst loading (4.5 mol%) than Co (4 mol%). M-N-C(i) catalysts derived from other $M(Phen)_2$ complexes (M = Cu, Mn, Cr, V, Ni) gave lower yields in screening reactions with benzyl alcohol. Substituted and halogenated benzylic, heterocyclic, allylic, and aliphatic alcohols were oxidized to nitriles with yields ≥60% under 5 bar O_2 in *t*-amyl alcohol solvent at 130 °C in 20–30 h. A similar scope can be accessed using a Co-N-C(iv)[61] synthesized with a 11,11′-Bis(dipyrido[3,2-a:2′,3′-c]phenazinyl) polymer, a Co-N-C(i) synthesized with a 1-methyl-3-cyanomethyl-1H-imidazolium chloride additive,[42] a Cu-Fe-N-C(ii)[62] synthesized with carbon-supported polyvinylpyridine, or a Co-N-C(i)[44] synthesized with piperazine and tartaric acid ligands. Primary amine substrates can also be oxidized instead of alcohols to afford nitriles using Fe-N-C(i)[63] and Co-N-C(i)[64] catalysts. Aqueous conditions[65,66] that avoid the use of organic solvents have also been reported using a Co-N-C(v)[65] derived from a Co-imidazolate MOF core with a Zn-imidazolate shell or an Fe-N-C(v)[66] derived from an Fe-doped Zn-imidazolate MOF impregnated with benzylamine. In an exemplary case[66] (**Figure 4.6 B**), substituted and halogenated benzylic, heterocyclic, allylic, and aliphatic nitriles were synthesized in water at lower temperature (35 °C), although higher temperatures were required for less reactive substrates.

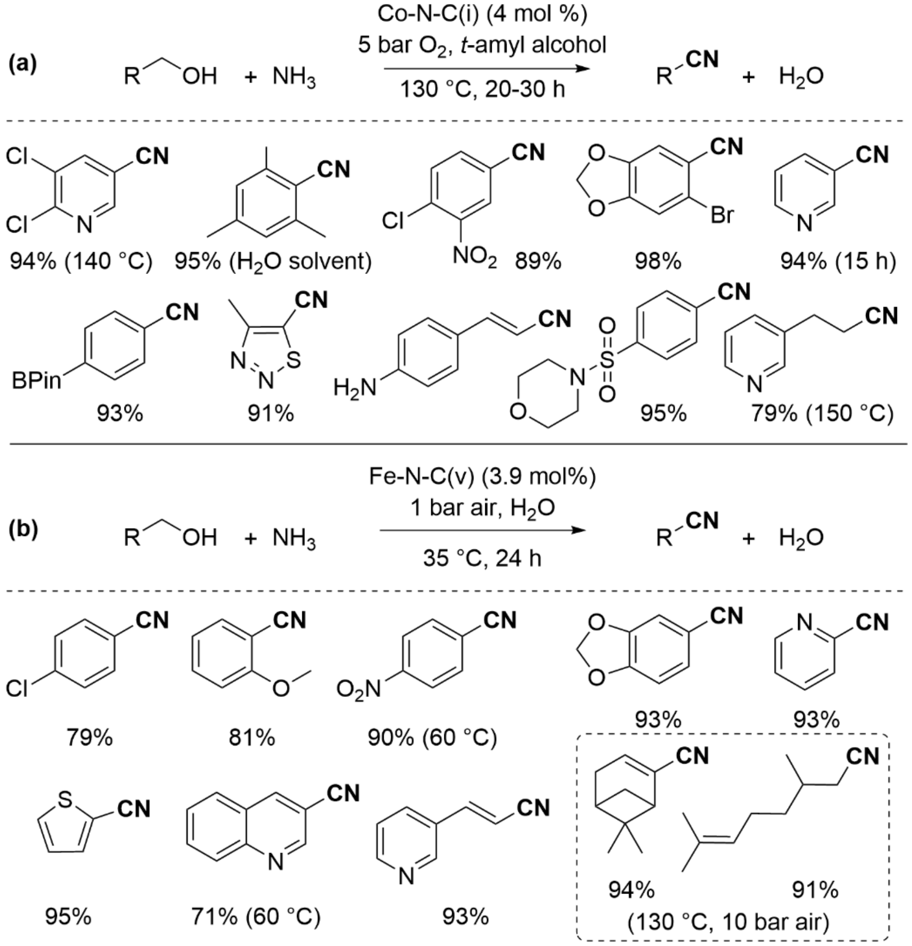

Figure 4.6: Synthesis of nitriles from alcohols and ammonia. A. in organic solvent[60] and… B. in aqueous solvent.[66] Percentages reflect yield of the specified product.

Different metal species have been characterized in catalysts used for nitrile synthesis. In their initial report,[60] Beller and coworkers attributed reactivity to CoO_x and FeO_x nanoparticles encapsulated within N-doped graphitic shells, while Huang and coworkers[42] observed metallic Co aggregates by XRD and ionic Co by XPS consistent with CoO_x surfaces. In a more recent study, Beller and coworkers[44] attributed reactivity to metallic Co particles within N-doped graphitic shells. Cai, Lu, and coworkers[65] similarly observed metallic Co nanoparticles (6 nm average diameter) in TEM images. On the other hand, metal nanoparticles were not detected in a Co-N-

C(iv)[61] by XRD or TEM, but XPS detected Co–N bonds, which is consistent with CoN_x species. FeN_x were also detected in STEM images of a Fe-N-C(v) catalyst[66] that lacked Fe nanoparticles in XRD patterns and STEM images. The bimetallic Cu-Fe-N-C(ii) studied by Kobayashi and coworkers[62] had both mono- and bimetallic nanoparticles according to XRD and STEM, and analysis after acid washing treatments suggested that active Fe species resisted acid washing whereas active Cu species were diminished. Metal-free reactivity for this transformation has also been claimed,[67] although it is difficult to exclude the role of adventitious metal species.[68] Overall, studies that have attributed reactivity to aggregates did not conclusively rule out the presence of MN_x species, while studies detecting MN_x species could not rigorously exclude the presence of small aggregates. A quantitative basis for the reactivity of either species is currently lacking.

The proposed reaction pathway[60] for nitrile synthesis involves alcohol oxidation to an aldehyde, which undergoes condensation with ammonia to generate an imine via a hemiaminal intermediate.[61,66] The imine can then undergo oxidation to the nitrile. Consistent with this proposal, time course studies[61] detected benzaldehyde as an intermediate that was later consumed, and quantified rates of benzaldehyde conversion to the nitrile revealed an order of magnitude higher rate than benzyl alcohol conversion. Other studies have independently reported nitrile syntheses from aldehydes over M-N-C catalysts.[69–71]

Alcohol Oxidation to Primary Amides

Beller and coworkers[44] showed that conditions for nitrile synthesis could be adapted to form amides by including H_2O as a reactant (and solvent). These reactions used the previously noted Co-N-C(i) catalyst synthesized with piperazine and tartaric acid ligands. The reaction required high temperatures (120 °C) and high pressures (10 bar air). A variety of substituted benzoic amides including heterocycles could be synthesized using this method (**Figure 4.7**). Quantitative conversion of benzonitrile to benzamide was observed when benzonitrile was subjected to the reaction conditions. A similar scope of amides can also be synthesized starting from aldehyde substrates using an Fe-N-C(i) catalyst and similar conditions (H_2O solvent, 120 °C, 10 bar air, 24 h).[69] Well-defined rate data were not reported in these studies.

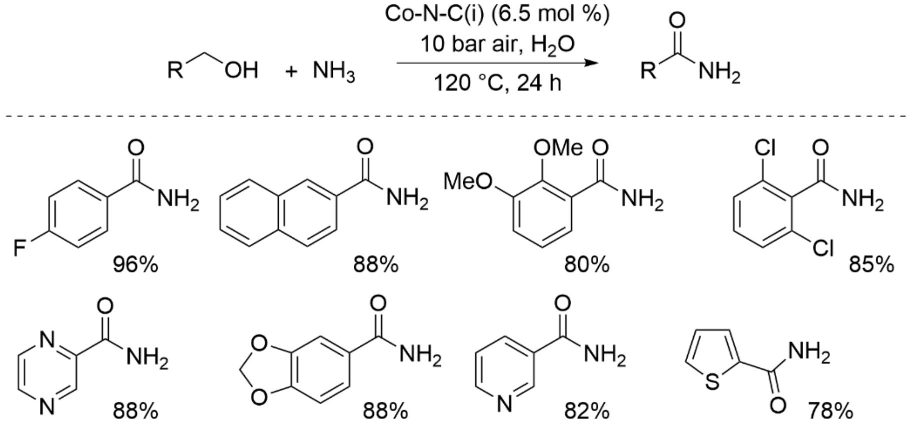

Figure 4.7: Aerobic oxidation of alcohols to amides over M-N-C.[44] Percentages reflect yield of the specified product.

Oxidative Dehydrogenation of *N*-heterocycles

Iosub and Stahl[72] reported the dehydrogenation of partially saturated *N*-heterocycles using a Co-N-C(i) catalyst synthesized via the pyrolysis of carbon-supported $Co(Phen)_2$ complex (**Figure 4.8 A**). A similar scope was reported concurrently by Beller and coworkers[73] using an Fe-N-C(i) catalyst synthesized with a carbon-supported $Fe(Phen)_3$ precursor (**Figure 4.8 B**). Substituted tetrahydroquinolines and other *N*-heterocycles were dehydrogenated under different conditions in each report: the Fe-N-C(i) catalyst was used at lower loading than the Co-N-C(i) catalyst and without exogenous base, but with higher temperature, O_2 pressure, and duration (100 °C, 15 bar

O_2, 12 h). Metallic Co and Co_3O_4 nanoparticles were detected in the Co-N-C(i) material by XRD, whereas the Fe-N-C(i) material did not have nanoparticles large enough to give XRD features, but FeO_x nanoparticles encapsulated within graphitic sheets were observed in TEM images. Selectivity improved when some of the nanoparticles were leached in an acid treatment step. The identity of the active centers was not probed further in these reports, and MN_x centers were not considered. Co-N-C(ii),[74] Co-N-C(v),[75] and Fe-N-C(iv)[76] catalysts with similar structural features have been reported to promote this reaction with similar scope. Zhang and coworkers[77] reported that an Fe-N-C(iii) catalyst synthesized with $FeCl_3$ and a 1-butyl-3-methylimidazolium bromide ionic liquid facilitated the oxidation of three biologically relevant *N*-heterocycles and 1,2-diphenylhydrazine in phosphate-buffered (pH = 7.4) aqueous solution under O_2 at ambient temperature. Including NaSCN in the reaction mixture eliminated reactivity, implicating FeN_x sites as the active centers. In a complementary study, Li, Jaouen, and coworkers[78] showed that an Fe-N-C(v) catalyst derived from an Fe(Phen)-impregnated ZIF-8 MOF catalyzed the oxidative dehydrogenation of NADPH to $NADP^+$. In 2022, Beller and coworkers[79] reported *N*-heterocycle dehydrogenation using a Zn-N-P-C(v) catalyst synthesized with a ZIF-8 MOF impregnated with triphenylphosphine as the precursor. Quinoline yields after 6 h (110 °C, 1 bar air, H_2O solvent) were weakly affected by the inclusion of KSCN (2–5 eq. with respect to Zn), suggesting that the active sites were not metallic.

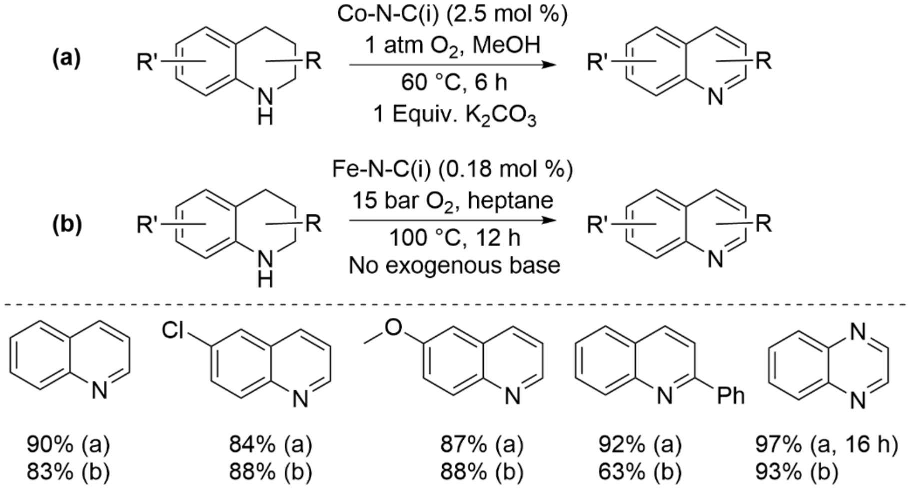

Figure 4.8: Dehydrogenation of *N*-heterocycles developed by A. Iosub and Stahl,[72] and B. Beller and coworkers.[73] Percentages reflect yield of the specified product.

Other Relevant Aerobic Oxidations

Aerobic oxidations related to those described above have also been developed. Intramolecular oxidative cyclization of an *o*-aminophenol-derived imine was reported to form a benzoxazole ring, using a Co-N-C catalyst synthesized by the pyrolysis of SiO_2-supported $Co(Phen)_2$ complex.[80]Xu et al.[81] reported benzylamine oxidation and subsequent reaction with primary amines to form imines over a V-N-C(v) catalyst synthesized by the pyrolysis of a V-containing MOF (NH_2-MIL-101(V)). The scope of its oxidative homocoupling reactivity included heteroatom-containing benzylic amines and aliphatic amines, in addition to cross-coupling of benzylamine with aniline or aliphatic amines. The V-N-C(v) catalyst did not have nanoparticles detectible by XRD or TEM. The authors concluded that VN_4 sites catalyzed the reaction, but suitable controls were not included to rule out the potential contributions of small VO_x moieties. The normalized rate (per total V) of the V-N-C(v) catalyst to form N-benzylidene benzylamine was 54 mol (mol V)$^{-1}$ s^{-1}.

Gu and coworkers[82] reported the preparation of conjugated diynes by a Glaser-Hay type reaction catalyzed by a Cu-N-C(iv) catalyst synthesized with dopamine hydrochloride and Cu precursors. At 40 °C in ambient air, 1,3-diynes were synthesized in 85–97% yields by oxidative homocoupling of terminal aryl and alkyl alkynes. The same catalyst under the same conditions achieved selective heterocoupling of aryl and alkyl alkynes with yields of 65–82% by using a slight excess of one substrate (1.3:1). Trifluoromethyl, halogen, methoxy, and phenoxy substituents, and S- and N-containing heterocycles were tolerated. The active centers were hypothesized to be mononuclear CuN_x sites based on a low Cu-Cu scattering intensity in the EXAFS and density functional theory (DFT) calculations showing a low energy barrier for coupling of aromatic and aliphatic alkynes on the CuN_x sites. Rate data under well-defined conditions were not quantified.

Ethylbenzene oxidation[83−87] and other arylalkane oxidations[88−90] have been reported in the presence of M-N-C catalysts, but the role of the M-N-C is unclear, as many studies report non-zero yields in blank reactions and with metal-free solids, suggesting a potential role of radical-chain pathways that could be modulated by the M-N-C. Oxidation of internal diols or esterification of benzylic ketones, both requiring C–C oxidative cleavage, also could feature radical pathways.[91,92]

Adopting Co-N-C Catalysts from the Fuel Cell Literature to Mediator Regeneration

The lack of careful characterization present in most aerobic oxidation studies utilizing M-N-C catalysts suggested that there might be an opportunity in the synthesis of materials instead precedented in the space of ORR, where characterization is typically more rigorous. As part of an early effort to grapple with this transition, the Stahl group identified a list of recently published procedures that identified such catalysts and synthesized them in-house (**Table 4.1**). (Many of them were synthesized as part of a separate effort, and a subset are included in that publication.[93]) The syntheses were followed closely with regards to ligand identity and pyrolysis conditions, but only cobalt-containing compositions were included within this comparison, vulcan black carbon was used as a support for each applicable These catalysts therefore share a metal dopant and a support – except for the MOF-derived catalysts, which have no exogenous support at all – but differences in nitrogen source and synthetic conditions ensured a diverse array of physical features and suggested the possibility of a correspondingly diverse set of activities for aerobic oxidation. (For precise synthetic conditions and the resultant active site properties, see the individual publications in the table).

Catalyst	**Ligand**	**Reference**
Co-DCD/C	Dicyandiamide	94
Co-phen/C	1,10-Phenanthroline	95
Co-Pc/C	Phthalocyanine	96
Co-(PANI+CM)/C	Polyaniline + Cyanamide	97
Co-PANI/C	Polyaniline	97
Co-CM/C	Cyanamide	98
CoNp-MOF/C	2-Methylimidazole	99
CoN_4-MOF/C	2-Methylimidazole	100

Table 4.1: Co-N-C materials precedented as ORR catalysts. In each case, the ligand acts as the nitrogen source.

Of particular interest among the assortment of catalysts selected were those derived from MOFs. Their lack of external support and intrinsic nitrogen content provided the potential for highly consistent batch-to-batch synthesis, which also provided an ideal platform for varying synthetic conditions in attempts to perturb active site formation and thus activity. Two catalysts were chosen from this class. A 2015 report using a relatively low pyrolysis temperature of 900 °C and a standard time profile (3 h total) found that the resultant Co-MOF/C formed primarily aggregated Co nanoparticles (notated as CoNp-MOF/C).[99] This characterization was confirmed with both XRD and TEM analysis, and was assessed as being reliable due to the agreement of the bulk and microscopic techniques. Fascinatingly, a 2017 report showed that the same MOF pyrolyzed under much more aggressive conditions at 1100 °C, but withdrawn after a shorter time period of 1 h, formed almost exclusively single-atom sites (notated as CoN_4-MOF/C).[100] In support of this single-atom characterization, they provided TEM, HRSTEM, and EELS data showing the presence of such sites. This was exceptionally strong evidence that single-atom sites existed, but their claim that they had *exclusively* generated these sites (supported primarily by the lack of nanoparticles seen by XRD, suggesting an absence of large bulk phases) was judged as being much weaker. Nonetheless, the differences were sufficiently drastic to warrant testing each.

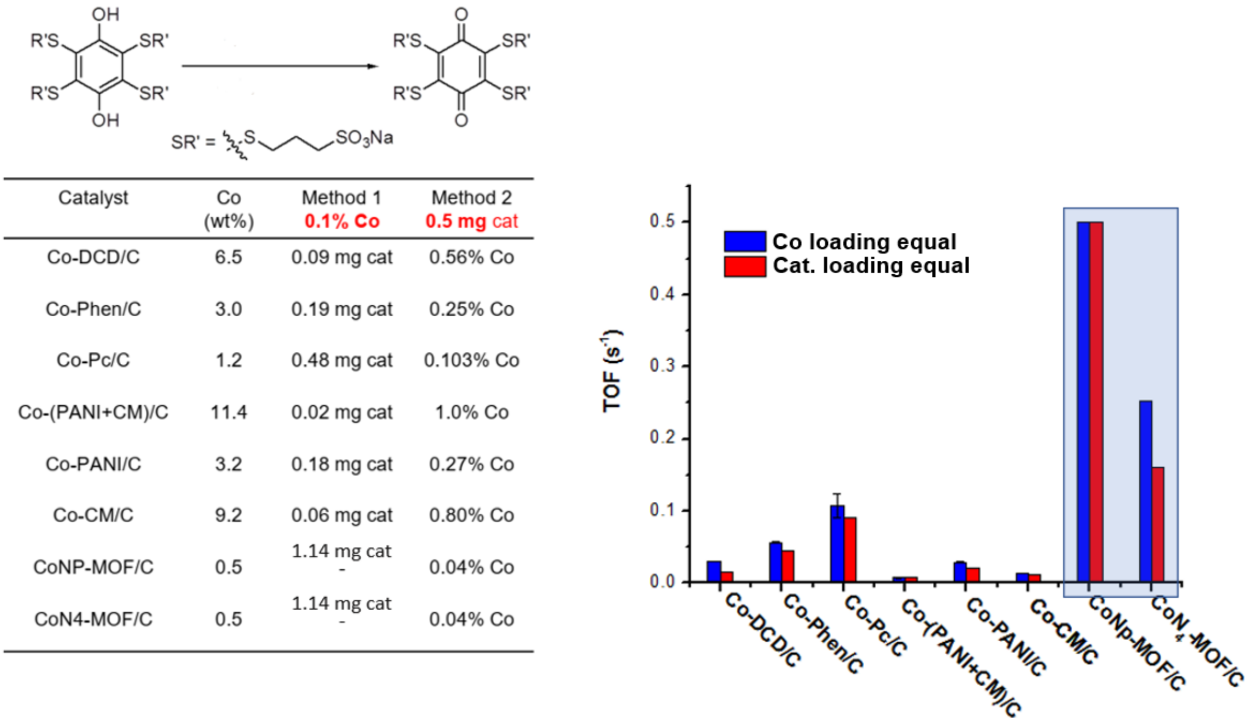

Catalyst	Co (wt%)	Method 1 **0.1% Co**	Method 2 **0.5 mg cat**
Co-DCD/C	6.5	0.09 mg cat	0.56% Co
Co-Phen/C	3.0	0.19 mg cat	0.25% Co
Co-Pc/C	1.2	0.48 mg cat	0.103% Co
Co-(PANI+CM)/C	11.4	0.02 mg cat	1.0% Co
Co-PANI/C	3.2	0.18 mg cat	0.27% Co
Co-CM/C	9.2	0.06 mg cat	0.80% Co
CoNP-MOF/C	0.5	1.14 mg cat -	0.04% Co
CoN4-MOF/C	0.5	1.14 mg cat -	0.04% Co

Figure 4.9: Screening of Co-N-C materials for catalytic activity in aerobic hydroquinone oxidation. Bulk metal loadings are listed on the left. The blue rectangle identifies the most active catalytic materials. Conditions: 0.1 M t-MPSNaH_2, 0.5 M H_2SO_4. 40 °C, 0.3 psig O_2.

The as-synthesized materials were used as catalysts for t-MPSNa oxidation. Batch screening was conducted and conversion was monitored over the first 10–20 minutes, allowing for the determination of an initial rate. This approach followed the general procedure published in the closely related work mentioned above).[93] Initial rates for each catalyst were measured twice, once with a catalyst loading normalized to the amount of bulk metal present in the system (meant as a first approximation for active sites) and once with loading normalized to the amount of bulk catalyst (the most relevant parameter for determining the size of a catalytic bed or maximum coating on an electrode). The results are summarized in **Figure 4.9**.

Screening for catalytic activity in mediator oxidation offered several insights into the reaction paradigm at play. The consistent high performance shown by catalysts with low metal content when using constant metal loading (e.g., Co-Pc/C, Co-MOF/Cs) suggested that many of these materials had significant amounts of metal trapped in inactive or inaccessible forms. Crucially, however, while the differences in rate sometimes diminished upon the switch to constant catalyst loading, the general trends between different compositions held true. This indicates that the choice of ligand has a clear impact on the final catalytic activity, despite the presumed complete decomposition of molecular structure during the extreme pyrolysis conditions. Further, this activity does not clearly correlate with the nitrogen ratio of the starting ligand, hinting at deeper mechanistic considerations. The clear outlying performance of the MOF-derived materials is striking, but its cause is difficult to identify. Some of the difference is presumably intrinsic, caused by an advantage of the 2-methylimidazole nitrogen source. The self-supporting nature of the material may itself be a contributing factor as well, however; the Vulcan black exogenous carbon support is expected to have a total BET surface area of approximately 200 m^2/g, (prior to pyrolysis, which will lower it) but the MOF precursor has > 1000 m^2/g of BET surface area and even the measured porosity of the post-pyrolysis MOFs (Figure 4.10) is 430 m^2/g. Greater surface area provides the opportunity for more active sites to be available to substrate, although a chemical titration method would be necessary to prove that point definitively (and had not been identified at the time of this research).

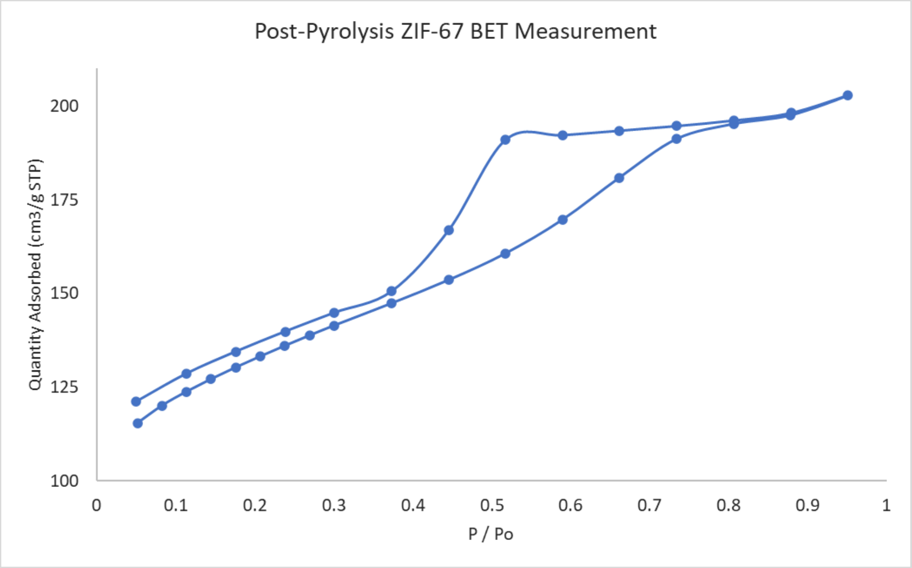

Figure 4.10: N_2 adsorption isotherm of the post-pyrolysis CoNp-MOF/C material. Note the hysteresis in the trace, likely indicative of mesoporous character in the material. The calculated BET surface area of this material is 430 m^2/g.

These findings suggest obvious next steps, some of which have been the targets of recent research findings. The clear need for more rigorous characterization of these materials, including complementary application of bulk and microscopic techniques and chemical titrations for active site counting, has already been the focus of discussion in previous sections. The implication that much of the metal in these catalysts remains inactive suggests a need for new metalation approaches, an exciting research area that is currently being pursued within the group.[101] Promising research directions remain unexplored. Work tuning the porosity of M-N-C materials – with salt additives, sacrificial templating, and macro-structured precursors all being popular directions – continues, but no compelling porosity-activity relationship has yet emerged within the community. In situ analysis of the reactions that various nitrogen dopants undergo during pyrolysis remains challenging, but would be a vital step in understanding how and tuning N moieties are incorporated within the graphitic framework. Solving that challenge is left as an exercise for the reader.

Acknowledgements

The work in this section is largely unpublished, and so a separate acknowledgements section is appropriate. We thank Dr. Sourav Biswas for the synthesis of the non-MOF catalysts referenced and for his contributions in joint characterization and activity benchmarking of these materials. This research was supported by the Center for Molecular Electrocatalysis, an Energy Frontier Research Center, funded by the U.S. Department of Energy, Office of Science, Office of Basic Energy Sciences.

References

---

1. Cui, X.; Li, W.; Ryabchuk, P.; Junge, K.; Beller, M. Bridging Homogeneous and Heterogeneous Catalysis by Heterogeneous Single-Metal-Site Catalysts. *Nat. Catal.* **2018**, *1*, 385.
2. Kaiser, S. K.; Chen, Z.; Faust Akl, D.; Mitchell, S.; Pérez-Ramírez, J. Single-Atom Catalysts across the Periodic Table. *Chem. Rev.* **2020**, *120*, 11703–11809.
3. Bagotzky, V. S.; Tarasevich, M. R.; Radyushkina, K. A.; Levina, O. A.; Andrusyova, S. I. Electrocatalysis of the Oxygen Reduction Process on Metal Chelates in Acid Electrolyte. *J. Power Sources* **1978**, *2*, 233–240.
4. van Veen, J. A. R.; van Baar, J. F.; Kroese, K. J. Effect of Heat Treatment on the Performance of Carbon-Supported Transition-Metal Chelates in the Electrochemical Reduction of Oxygen. *J. Chem. Soc., Faraday Trans. 1* **1981**, *77*, 2827–2843.
5. Scherson, D. A.; Gupta, S. L.; Fierro, C.; Yeager, E. B.; Kordesch, M. E.; Eldridge, J.; Hoffman, R. W.; Blue, J. Cobalt Tetramethoxyphenyl Porphyrin—Emission Mossbauer Spectroscopy and O2 Reduction Electrochemical Studies. *Electrochim. Acta* **1983**, *28*, 1205–1209.
6. Gewirth, A. A.; Varnell, J. A.; DiAscro, A. M. Nonprecious Metal Catalysts for Oxygen Reduction in Heterogeneous Aqueous Systems. *Chem. Rev.* **2018**, *118*, 2313–2339.
7. Wang, W.; Jia, Q.; Mukerjee, S.; Chen, S. Recent Insights into the Oxygen-Reduction Electrocatalysis of Fe/N/C Materials. *ACS Catal.* **2019**, *9*, 10126–10141.
8. Zhao, C.-X.; Li, B.-Q.; Liu, J.-N.; Zhang, Q. Intrinsic Electrocatalytic Activity Regulation of M–N–C Single-Atom Catalysts for the Oxygen Reduction Reaction. *Angew. Chem. Int. Ed.* **2021**, *60*, 4448–4463.

9. He, Y.; Liu, S.; Priest, C.; Shi, Q.; Wu, G. Atomically Dispersed Metal–Nitrogen–Carbon Catalysts for Fuel Cells: Advances in Catalyst Design, Electrode Performance, and Durability Improvement. *Chem. Soc. Rev.* **2020**, *49*, 3484–3524.
10. Sun, T.; Tian, B.; Lu, J.; Su, C. Recent Advances in Fe (or Co)/N/C Electrocatalysts for the Oxygen Reduction Reaction in Polymer Electrolyte Membrane Fuel Cells. *J. Mater. Chem. A* **2017**, *5*, 18933–18950.
11. Martinez, U.; Komini Babu, S.; Holby, E. F.; Chung, H. T.; Yin, X.; Zelenay, P. Progress in the Development of Fe-Based PGM-Free Electrocatalysts for the Oxygen Reduction Reaction. *Adv. Mater.* **2019**, *31*, 1806545.
12. Shi, Q.; Hwang, S.; Yang, H.; Ismail, F.; Su, D.; Higgins, D.; Wu, G. Supported and Coordinated Single Metal Site Electrocatalysts. *Mater. Today* **2020**, *37*, 93–111.
13. Asset, T.; Atanassov, P. Iron-Nitrogen-Carbon Catalysts for Proton Exchange Membrane Fuel Cells. *Joule* **2020**, *4*, 33–44.
14. Varela, A. S.; Ranjbar Sahraie, N.; Steinberg, J.; Ju, W.; Oh, H.-S.; Strasser, P. Metal-Doped Nitrogenated Carbon as an Efficient Catalyst for Direct CO2 Electroreduction to CO and Hydrocarbons. *Angew. Chem. Int. Ed.* **2015**, *54*, 10758–10762.
15. Li, J.; Pršlja, P.; Shinagawa, T.; Martín Fernández, A. J.; Krumeich, F.; Artyushkova, K.; Atanassov, P.; Zitolo, A.; Zhou, Y.; García-Muelas, R.; et al. Volcano Trend in Electrocatalytic CO2 Reduction Activity over Atomically Dispersed Metal Sites on Nitrogen-Doped Carbon. *ACS Catal.* **2019**, *9*, 10426–10439.

16. Geng, Z.; Liu, Y.; Kong, X.; Li, P.; Li, K.; Liu, Z.; Du, J.; Shu, M.; Si, R.; Zeng, J. Achieving a Record-High Yield Rate of 120.9 for N2 Electrochemical Reduction over Ru Single-Atom Catalysts. *Adv. Mater.* **2018**, *30*, 1803498.
17. Jagadeesh, R. V.; Wienhöfer, G.; Westerhaus, F. A.; Surkus, A.-E.; Pohl, M.-M.; Junge, H.; Junge, K.; Beller, M. Efficient and Highly Selective Iron-Catalyzed Reduction of Nitroarenes. *Chem. Commun.* **2011**, *47*, 10972.
18. Westerhaus, F. A.; Jagadeesh, R. V.; Wienhöfer, G.; Pohl, M.-M.; Radnik, J.; Surkus, A.-E.; Rabeah, J.; Junge, K.; Junge, H.; Nielsen, M.; et al. Heterogenized Cobalt Oxide Catalysts for Nitroarene Reduction by Pyrolysis of Molecularly Defined Complexes. *Nat. Chem.* **2013**, *5*, 537–543.
19. Jagadeesh, R. V.; Surkus, A.-E.; Junge, H.; Pohl, M.-M.; Radnik, J.; Rabeah, J.; Huan, H.; Schünemann, V.; Brückner, A.; Beller, M. Nanoscale Fe2O3-Based Catalysts for Selective Hydrogenation of Nitroarenes to Anilines. *Science* **2013**, *342*, 1073–1076.
20. Jagadeesh, R. V.; Murugesan, K.; Alshammari, A. S.; Neumann, H.; Pohl, M.-M.; Radnik, J.; Beller, M. MOF-Derived Cobalt Nanoparticles Catalyze a General Synthesis of Amines. *Science* **2017**, *358*, 326–332.
21. He, L.; Weniger, F.; Neumann, H.; Beller, M. Synthesis, Characterization, and Application of Metal Nanoparticles Supported on Nitrogen-Doped Carbon: Catalysis beyond Electrochemistry. *Angew. Chem. Int. Ed.* **2016**, *55*, 12582–12594.
22. Mallat, T.; Baiker, A. Oxidation of Alcohols with Molecular Oxygen on Solid Catalysts. *Chem. Rev.* **2004**, *104*, 3037–3058.

23. Liu, X.; Madix, R. J.; Friend, C. M. Unraveling Molecular Transformations on Surfaces: A Critical Comparison of Oxidation Reactions on Coinage Metals. *Chem. Soc. Rev.* **2008**, *37*, 2243–2261.

24. Davis, S. E.; Ide, M. S.; Davis, R. J. Selective Oxidation of Alcohols and Aldehydes over Supported Metal Nanoparticles. *Green Chem.* **2012**, *15*, 17–45.

25. Miyamura, H.; Kobayashi, S. Tandem Oxidative Processes Catalyzed by Polymer-Incarcerated Multimetallic Nanoclusters with Molecular Oxygen. *Acc. Chem. Res.* **2014**, *47*, 1054–1066.

26. Stahl, S. S. Palladium Oxidase Catalysis: Selective Oxidation of Organic Chemicals by Direct Dioxygen-Coupled Turnover. *Angew. Chem. Int. Ed.* **2004**, *43*, 3400–3420.

27. Piera, J.; Bäckvall, J.-E. Catalytic Oxidation of Organic Substrates by Molecular Oxygen and Hydrogen Peroxide by Multistep Electron Transfer—A Biomimetic Approach. *Angew. Chem. Int. Ed.* **2008**, *47*, 3506–3523.

28. Wendlandt, A. E.; Suess, A. M.; Stahl, S. S. Copper-Catalyzed Aerobic Oxidative C–H Functionalizations: Trends and Mechanistic Insights. *Angew. Chem. Int. Ed.* **2011**, *50*, 11062–11087.

29. Allen, S. E.; Walvoord, R. R.; Padilla-Salinas, R.; Kozlowski, M. C. Aerobic Copper-Catalyzed Organic Reactions. *Chem. Rev.* **2013**, *113*, 6234–6458.

30. Ryland, B. L.; Stahl, S. S. Practical Aerobic Oxidations of Alcohols and Amines with Homogeneous Copper/TEMPO and Related Catalyst Systems. *Angew. Chem. Int. Ed.* **2014**, *53*, 8824–8838.

---

31. Li, J.; Jiao, L.; Wegener, E.; Richard, L. L.; Liu, E.; Zitolo, A.; Sougrati, M. T.; Mukerjee, S.; Zhao, Z.; Huang, Y.; et al. Evolution Pathway from Iron Compounds to Fe1(II)–N4 Sites through Gas-Phase Iron during Pyrolysis. *J. Am. Chem. Soc.* **2020**, *142*, 1417–1423.
32. Lefèvre, M.; Proietti, E.; Jaouen, F.; Dodelet, J.-P. Iron-Based Catalysts with Improved Oxygen Reduction Activity in Polymer Electrolyte Fuel Cells. *Science* **2009**, *324*, 71–74.
33. Gupta, S.; Tryk, D.; Bae, I.; Aldred, W.; Yeager, E. Heat-Treated Polyacrylonitrile-Based Catalysts for Oxygen Electroreduction. *J. Appl. Electrochem.* **1989**, *19*, 19–27.
34. Wu, G.; More, K. L.; Johnston, C. M.; Zelenay, P. High-Performance Electrocatalysts for Oxygen Reduction Derived from Polyaniline, Iron, and Cobalt. *Science* **2011**, *332*, 443–447.
35. Han, L.; Cheng, H.; Liu, W.; Li, H.; Ou, P.; Lin, R.; Wang, H.-T.; Pao, C.-W.; Head, A. R.; Wang, C.-H.; et al. A Single-Atom Library for Guided Monometallic and Concentration-Complex Multimetallic Designs. *Nat. Mater.* **2022**, *21*, 681–688.
36. Serov, A.; Artyushkova, K.; Niangar, E.; Wang, C.; Dale, N.; Jaouen, F.; Sougrati, M.-T.; Jia, Q.; Mukerjee, S.; Atanassov, P. Nano-Structured Non-Platinum Catalysts for Automotive Fuel Cell Application. *Nano Energy* **2015**, *16*, 293–300.
37. Serov, A.; Robson, M. H.; Artyushkova, K.; Atanassov, P. Templated Non-PGM Cathode Catalysts Derived from Iron and Poly(Ethyleneimine) Precursors. *Appl. Catal., B* **2012**, *127*, 300–306.
38. Proietti, E.; Jaouen, F.; Lefèvre, M.; Larouche, N.; Tian, J.; Herranz, J.; Dodelet, J.-P. Iron-Based Cathode Catalyst with Enhanced Power Density in Polymer Electrolyte Membrane Fuel Cells. *Nat. Commun.* **2011**, *2*, 416.

---

39. Zhang, H.; Osgood, H.; Xie, X.; Shao, Y.; Wu, G. Engineering Nanostructures of PGM-Free Oxygen-Reduction Catalysts Using Metal-Organic Frameworks. *Nano Energy* **2017**, *31*, 331–350.

40. Bai, C.; Li, A.; Yao, X.; Liu, H.; Li, Y. Efficient and Selective Aerobic Oxidation of Alcohols Catalysed by MOF-Derived Co Catalysts. *Green Chem.* **2016**, *18*, 1061–1069.

41. Zhao, X.; Zhou, Y.; Jin, A.-L.; Huang, K.; Liu, F.; Tao, D.-J. Co-N-C Catalysts Synthesized by Pyrolysis of Co-Based Deep Eutectic Solvents for Aerobic Oxidation of Alcohols. *New J. Chem.* **2018**, *42*, 15871–15878.

42. Mao, F.; Qi, Z.; Fan, H.; Sui, D.; Chen, R.; Huang, J. Heterogeneous Cobalt Catalysts for Selective Oxygenation of Alcohols to Aldehydes, Esters and Nitriles. *RSC Adv.* **2017**, *7*, 1498–1503.

43. Sun, Y.; Ma, H.; Luo, Y.; Zhang, S.; Gao, J.; Xu, J. Activation of Molecular Oxygen Using Durable Cobalt Encapsulated with Nitrogen-Doped Graphitic Carbon Shells for Aerobic Oxidation of Lignin-Derived Alcohols. *Chem. Eur. J.* **2018**, *24*, 4653–4661.

44. Senthamarai, T.; Chandrashekhar, V. G.; Rockstroh, N.; Rabeah, J.; Bartling, S.; Jagadeesh, R. V.; Beller, M. A “Universal” Catalyst for Aerobic Oxidations to Synthesize (Hetero)Aromatic Aldehydes, Ketones, Esters, Acids, Nitriles, and Amides. *Chem* **2022**, *8*, 508–531.

45. Xie, J.; Kammert, J. D.; Kaylor, N.; Zheng, J. W.; Choi, E.; Pham, H. N.; Sang, X.; Stavitski, E.; Attenkofer, K.; Unocic, R. R.; et al. Atomically Dispersed Co and Cu on N-Doped Carbon for Reactions Involving C–H Activation. *ACS Catal.* **2018**, *8*, 3875–3884.

---

46. Xie, J.; Yin, K.; Serov, A.; Artyushkova, K.; Pham, H. N.; Sang, X.; Unocic, R. R.; Atanassov, P.; Datye, A. K.; Davis, R. J. Selective Aerobic Oxidation of Alcohols over Atomically-Dispersed Non-Precious Metal Catalysts. *ChemSusChem* **2017**, *10*, 359–362.
47. Huang, K.; Fu, H.; Shi, W.; Wang, H.; Cao, Y.; Yang, G.; Peng, F.; Wang, Q.; Liu, Z.; Zhang, B.; et al. Competitive Adsorption on Single-Atom Catalysts: Mechanistic Insights into the Aerobic Oxidation of Alcohols over Co–N–C. *J. Catal.* **2019**, *377*, 283–292.
48. Li, Z.; Fan, T.; Li, H.; Lu, X.; Ji, S.; Zhang, J.; Horton, J. H.; Xu, Q.; Zhu, J. Atomically Defined Undercoordinated Copper Active Sites over Nitrogen-Doped Carbon for Aerobic Oxidation of Alcohols. *Small* **2022**, *18*, 2106614.
49. Jagadeesh, R. V.; Junge, H.; Pohl, M.-M.; Radnik, J.; Brückner, A.; Beller, M. Selective Oxidation of Alcohols to Esters Using Heterogeneous Co3O4–N@C Catalysts under Mild Conditions. *J. Am. Chem. Soc.* **2013**, *135*, 10776–10782.
50. Zhong, W.; Liu, H.; Bai, C.; Liao, S.; Li, Y. Base-Free Oxidation of Alcohols to Esters at Room Temperature and Atmospheric Conditions Using Nanoscale Co-Based Catalysts. *ACS Catal.* **2015**, *5*, 1850–1856.
51. Deng, J.; Song, H.-J.; Cui, M.-S.; Du, Y.-P.; Fu, Y. Aerobic Oxidation of Hydroxymethylfurfural and Furfural by Using Heterogeneous CoxOy–N@C Catalysts. *ChemSusChem* **2014**, *7*, 3334–3340.
52. Lv, G.; Chen, S.; Zhu, H.; Li, M.; Yang, Y. Pyridinic-Nitrogen-Dominated Nitrogen-Doped Graphene Stabilized Cu for Efficient Selective Oxidation of 5-Hydroxymethfurfural. *Appl. Surf. Sci.* **2018**, *458*, 24–31.

---

53. Feng, Y.; Jia, W.; Yan, G.; Zeng, X.; Sperry, J.; Xu, B.; Sun, Y.; Tang, X.; Lei, T.; Lin, L. Insights into the Active Sites and Catalytic Mechanism of Oxidative Esterification of 5-Hydroxymethylfurfural by Metal-Organic Frameworks-Derived N-Doped Carbon. *J. Catal.* **2020**, *381*, 570–578.
54. Su, H.; Zhang, K.-X.; Zhang, B.; Wang, H.-H.; Yu, Q.-Y.; Li, X.-H.; Antonietti, M.; Chen, J.-S. Activating Cobalt Nanoparticles via the Mott-Schottky Effect in Nitrogen-Rich Carbon Shells for Base-Free Aerobic Oxidation of Alcohols to Esters. *J. Am. Chem. Soc.* **2017**, *139*, 811–818.
55. Li, N.; Shang, S.; Wang, L.; Niu, J.; Lv, Y.; Gao, S. Superior Performance of Co-N/m-C for Direct Oxidation of Alcohols to Esters under Air. *Chin. J. Catal.* **2018**, *39*, 1249–1257.
56. Panwar, V.; Ray, S. S.; Jain, S. L. Highly Efficient (CoOx-N@C, PANI) Nanopowder Derived from Pyrolysis of Polyaniline Grafted Cobalt Acetate for Oxidative Methyl Esterification of Benzyl Alcohols. *Mol. Catal.* **2017**, *427*, 31–38.
57. Long, Z.; Chen, X.; Lu, P.; Liu, S.; Zhang, Y.; Chen, G.; Tong, M.; Sun, L.; Zhan, W.; Huang, F. A Bi-Functional Cobalt and Nitrogen Co-Doped Carbon Catalyst for Aerobic Oxidative Esterification of Benzyl Alcohol with Methanol and Oxygen Reduction Reaction. *Catal. Lett.* **2019**, 149, 3160–3168.
58. Zhu, Q.; Wang, F.; Zhang, F.; Dong, Z. Renewable Chitosan-Derived Cobalt@N-Doped Porous Carbon for Efficient Aerobic Esterification of Alcohols under Air. *Nanoscale* **2019**, *11*, 17736–17745.

---

59. Zhou, Y.-X.; Chen, Y.-Z.; Cao, L.; Lu, J.; Jiang, H.-L. Conversion of a Metal–Organic Framework to N-Doped Porous Carbon Incorporating Co and CoO Nanoparticles: Direct Oxidation of Alcohols to Esters. *Chem. Commun.* **2015**, *51*, 8292–8295.
60. Jagadeesh, R. V.; Junge, H.; Beller, M. Green Synthesis of Nitriles Using Non-Noble Metal Oxides-Based Nanocatalysts. *Nat. Commun.* **2014**, *5*, 4123.
61. Shang, S.; Wang, L.; Dai, W.; Chen, B.; Lv, Y.; Gao, S. High Catalytic Activity of Mesoporous Co–N/C Catalysts for Aerobic Oxidative Synthesis of Nitriles. *Catal. Sci. Technol.* **2016**, *6*, 5746–5753.
62. Yasukawa, T.; Yang, X.; Kobayashi, S. Earth-Abundant Bimetallic Nanoparticle Catalysts for Aerobic Ammoxidation of Alcohols to Nitriles. *J. Org. Chem.* **2020**, *85*, 7543–7548.
63. Jagadeesh, R. V.; Junge, H.; Beller, M. “Nanorust”-Catalyzed Benign Oxidation of Amines for Selective Synthesis of Nitriles. *ChemSusChem* **2015**, *8*, 92–96.
64. Natte, K.; Jagadeesh, R. V.; Sharif, M.; Neumann, H.; Beller, M. Synthesis of Nitriles from Amines Using Nanoscale Co3O4-Based Catalysts via Sustainable Aerobic Oxidation. *Org. Biomol. Chem.* **2016**, *14*, 3356–3359.
65. Sun, K.; Sun, J.; Lu, G.-P.; Cai, C. Enhanced Catalytic Activity of Cobalt Nanoparticles Encapsulated with an N-Doped Porous Carbon Shell Derived from Hollow ZIF-8 for Efficient Synthesis of Nitriles from Primary Alcohols in Water. *Green Chem.* **2019**, *21*, 4334–4340.
66. Sun, K.; Shan, H.; Neumann, H.; Lu, G.-P.; Beller, M. Efficient Iron Single-Atom Catalysts for Selective Ammoxidation of Alcohols to Nitriles. *Nat. Commun.* **2022**, *13*, 1848.

---

67. Shang, S.; Dai, W.; Wang, L.; Lv, Y.; Gao, S. Metal-Free Catalysis of Nitrogen-Doped Nanocarbons for the Ammoxidation of Alcohols to Nitriles. *Chem. Commun.* **2017**, *53*, 1048–1051.
68. Wang, L.; Ambrosi, A.; Pumera, M. “Metal-Free” Catalytic Oxygen Reduction Reaction on Heteroatom-Doped Graphene Is Caused by Trace Metal Impurities. *Angew. Chem. Int. Ed.* **2013**, *52*, 13818–13821.
69. Murugesan, K.; Senthamarai, T.; Sohail, M.; Sharif, M.; Kalevaru, N. V.; Jagadeesh, R. V. Stable and Reusable Nanoscale Fe2O3-Catalyzed Aerobic Oxidation Process for the Selective Synthesis of Nitriles and Primary Amides. *Green Chem.* **2018**, *20*, 266–273.
70. Pan, L.; Fu, W.; Zhang, L.; Wang, S.; Tang, T. Highly Dispersed Co Species in N-Doped Carbon Enhanced the Aldehydes Ammoxidation Reaction Activity. *Mol. Catal.* **2022**, *518*, 112087.
71. Zhao, H.; Sun, X.; Xu, D.; Zhu, Q.; Zhu, Y.; Dong, Z. Fe-Based N-Doped Dendritic Catalysts for Catalytic Ammoxidation of Aromatic Aldehydes to Aromatic Nitriles. *J. Colloid Interface Sci.* **2020**, *565*, 177–185.
72. Iosub, A. V.; Stahl, S. S. Catalytic Aerobic Dehydrogenation of Nitrogen Heterocycles Using Heterogeneous Cobalt Oxide Supported on Nitrogen-Doped Carbon. *Org. Lett.* **2015**, *17*, 4404–4407.
73. Cui, X.; Li, Y.; Bachmann, S.; Scalone, M.; Surkus, A.-E.; Junge, K.; Topf, C.; Beller, M. Synthesis and Characterization of Iron–Nitrogen-Doped Graphene/Core–Shell Catalysts: Efficient Oxidative Dehydrogenation of *N*-Heterocycles. *J. Am. Chem. Soc.* **2015**, *137*, 10652–10658.

74. Liao, C.; Li, X.; Yao, K.; Yuan, Z.; Chi, Q.; Zhang, Z. Efficient Oxidative Dehydrogenation of *N*-Heterocycles over Nitrogen-Doped Carbon-Supported Cobalt Nanoparticles. *ACS Sustain. Chem. Eng.* **2019**, *7*, 3646–13654.
75. Wu, Y.; Chen, Z.; Cheong, W.-C.; Zhang, C.; Zheng, L.; Yan, W.; Yu, R.; Chen, C.; Li, Y. Nitrogen-Coordinated Cobalt Nanocrystals for Oxidative Dehydrogenation and Hydrogenation of N-Heterocycles. *Chem. Sci.* **2019**, *10*, 5345–5352.
76. Sun, S.; Liu, Z.; Yang, F.; Qiu, T.; Wang, M.; Feng, A.; Wang, Y.; Li, Y. FexC Enhancing the Catalytic Activity of FeNx in Oxidative Dehydration of N-Heterocycles. *Green Chemical Engineering* **2021**. DOI: 10.1016/j.gce.2021.12.007
77. He, F.; Mi, L.; Shen, Y.; Mori, T.; Liu, S.; Zhang, Y. Fe–N–C Artificial Enzyme: Activation of Oxygen for Dehydrogenation and Monoxygenation of Organic Substrates under Mild Condition and Cancer Therapeutic Application. *ACS Appl. Mater. Interfaces* **2018**, *10,* 35327–35333.
78. Wu, D.; Li, J.; Xu, S.; Xie, Q.; Pan, Y.; Liu, X.; Ma, R.; Zheng, H.; Gao, M.; Wang, W.; et al. Engineering Fe–N Doped Graphene to Mimic Biological Functions of NADPH Oxidase in Cells. *J. Am. Chem. Soc.* **2020**, *142*, 19602–19610.
79. Sun, K.; Shan, H.; Ma, R.; Wang, P.; Neumann, H.; Lu, G.-P.; Beller, M. Catalytic Oxidative Dehydrogenation of *N*-Heterocycles with Nitrogen/Phosphorus Co-Doped Porous Carbon Materials. *Chem. Sci.* **2022**, *13*, 6865–6872.
80. He, J.; Lin, F.; Yang, X.; Wang, D.; Tan, X.; Zhang, S. Sustainable Synthesis of 2-Arylbenzoxazoles over a Cobalt-Based Nanocomposite Catalyst. *Org. Process Res. Dev.* **2016**, *20*, 1093–1096.

---

81. Xu, Q.; Feng, B.; Ye, C.; Fu, Y.; Chen, D.-L.; Zhang, F.; Zhang, J.; Zhu, W. Atomically Dispersed Vanadium Sites Anchored on N-Doped Porous Carbon for the Efficient Oxidative Coupling of Amines to Imines. *ACS Appl. Mater. Interfaces* **2021**, *13*, 15168–15177.
82. Zhang, Y.; Wu, Y.; Su, Y.; Cao, Y.; Liang, Z.; Yang, D.; Yu, R.; Zhang, D.; Wu, J.; Xiao, W.; et al. In Situ Synthesis of CuN4/Mesoporous N-Doped Carbon for Selective Oxidative Crosscoupling of Terminal Alkynes under Mild Conditions. *Small* **2022**, *18*, 2105178.
83. Fu, L.; Chen, Y.; Zhao, S.; Liu, Z.; Zhu, R. Sulfur-Mediated Synthesis of N-Doped Carbon Supported Cobalt Catalysts Derived from Cobalt Porphyrin for Ethylbenzene Oxidation. *RSC Adv.* **2016**, *6*, 19482–19491.
84. Qiu, Y.; Yang, C.; Huo, J.; Liu, Z. Synthesis of Co-N-C Immobilized on Carbon Nanotubes for Ethylbenzene Oxidation. *J. Mol. Catal. A Chem.* **2016**, *424*, 276–282.
85. Yang, C.; Fu, L.; Zhu, R.; Liu, Z. Influence of Cobalt Species on the Catalytic Performance of Co-N-C/SiO2 for Ethylbenzene Oxidation. *Phys. Chem. Chem. Phys.* **2016**, *18*, 4635–4642.
86. Liu, W.; Zhang, L.; Liu, X.; Liu, X.; Yang, X.; Miao, S.; Wang, W.; Wang, A.; Zhang, T. Discriminating Catalytically Active FeNx Species of Atomically Dispersed Fe–N–C Catalyst for Selective Oxidation of the C–H Bond. *J. Am. Chem. Soc.* **2017**, *139*, 10790–10798.
87. Jie, S.; Yang, C.; Chen, Y.; Liu, Z. Facile Synthesis of Ultra-Stable Co-N-C Catalysts Using Cobalt Porphyrin and Peptides as Precursors for Selective Oxidation of Ethylbenzene. *Mol. Catal.* **2018**, *458*, 1–8.
88. Tu, D.-H.; Li, Y.; Li, J.; Gu, Y.-J.; Wang, B.; Liu, Z.-T.; Liu, Z.-W.; Lu, J. Selective Oxidation of Arylalkanes with N-Graphitic-Modified Cobalt Nanoparticles in Water. *Catal. Commun.* **2017**, *97*, 130–133.

---

89. Lin, X.; Jie, S.; Liu, Z. Sulfur and Nitrogen-Doped Porous Cobalt Carbon Catalyst for High Efficient Aerobic Oxidation of Hydrocarbons. *Mol. Catal.* **2018**, *455*, 143–149.
90. Wang, X.; Jie, S.; Liu, Z. The Influence of Encapsulated Cobalt Content within N-Doped Bamboo-like Carbon Nanotubes Catalysts for Arylalkanes Oxidation. *Mater. Chem. Phys.* **2019**, *232*, 393–399.
91. Luo, H.; Wang, L.; Shang, S.; Niu, J.; Gao, S. Aerobic Oxidative Cleavage of 1,2-Diols Catalyzed by Atomic-Scale Cobalt-Based Heterogeneous Catalyst. *Commun. Chem.* **2019**, *2*, 17.
92. Xie, C.; Lin, L.; Huang, L.; Wang, Z.; Jiang, Z.; Zhang, Z.; Han, B. Zn-Nx Sites on N-Doped Carbon for Aerobic Oxidative Cleavage and Esterification of C(CO)-C Bonds. *Nat. Commun.* **2021**, *12*, 4823.
93. Bates, J. S.; Biswas, S.; Suh, S.-E.; Johnson, M. R.; Mondal, B.; Root, T. W.; Stahl, S. S. Chemical and Electrochemical O2 Reduction on Earth-Abundant M-N-C Catalysts and Implications for Mediated Electrolysis. *J. Am. Chem. Soc.* **2022**, *144*, 922–927.
94. Lu, X.; Xu, K.; Chen, P.; Jia, K.; Liu, S.; Wu, C. Facile One Step Method Realizing Scalable Production of G-C3N4nanosheets and Study of Their Photocatalytic H2evolution Activity. *J. Mater. Chem. A.* **2014**, 2, 18924–18928.
95. Fu, X.; Zamani, P.; Choi, J.-Y.; Hassan, F. M.; Jiang, G.; Higgins, D. C.; Zhang, Y.; Hoque, M. A.; Chen, Z. In Situ Polymer Graphenization Ingrained with Nanoporosity in a Nitrogenous Electrocatalyst Boosting the Performance of Polymer-Electrolyte-Membrane Fuel Cells. Adv. Mater. **2017**, *29*.

96. Zhang, Z.; Sun, J.; Wang, F.; Dai, L. Efficient Oxygen Reduction Reaction (ORR) Catalysts Based on Single Iron Atoms Dispersed on a Hierarchically Structured Porous Carbon Framework. *Angew. Chem.* **2018**, *130*, 9176–9181.

97. Wu, G.; More, K. L.; Johnston, C. M.; Zelenay, P. High-Performance Electrocatalysts for Oxygen Reduction Derived from Polyaniline, Iron, and Cobalt. *Science* **2011**, *332*, 443–447.

98. Chung, H. T.; Won, J. H.; Zelenay, P. Active and Stable Carbon Nanotube/Nanoparticle Composite Electrocatalyst for Oxygen Reduction. *Nat. Commun.* **2013**, *4*, 1922.

99. You, B.; Jiang, N.; Sheng, M.; Drisdell, W. S.; Yano, J.; Sun, Y. Bimetal–Organic Framework Self-Adjusted Synthesis of Support-Free Nonprecious Electrocatalysts for Efficient Oxygen Reduction. *ACS Catal.* **2015**, *5*, 7068–7076.

100. Wang, X. X.; Cullen, D. A.; Pan, Y.-T.; Hwang, S.; Wang, M.; Feng, Z.; Wang, J.; Engelhard, M. H.; Zhang, H.; He, Y.; Shao, Y.; Su, D.; More, K. L.; Spendelow, J. S.; Wu, G. Nitrogen-Coordinated Single Cobalt Atom Catalysts for Oxygen Reduction in Proton Exchange Membrane Fuel Cells. *Adv. Mater.* **2018**, *30*.

101. Bates, J. S.; Khamespanah, F.; Cullen, D. A.; Al-Omari, A. A.; Hopkins, M. N.; Martinez, J. J.; Root, T. W.; Stahl, S. S. Molecular Catalyst Synthesis Strategies to Prepare Atomically Dispersed Fe-N-C Heterogeneous Catalysts. *J. Am. Chem. Soc.* **2022**, *144*, 18797–18802.

Appendix 1

Alternatives to the Packed Bed for Lab-Scale Flow Chemistry

Introduction

Design of a flow system that involves a catalyst typically requires the catalyst to be retained within one part of the system. The systems described throughout this dissertation accomplish this goal through the use of packed bed reactors, which have the advantages of providing excellent contact in two- and three-phase reactions and readily scaling to arbitrary sizes. One major disadvantage of the packed bed, however, is the pressure drop it experiences when packed with fine powders. The Kozeny-Carman equation illustrates the issue:

$$\frac{\Delta p}{L} = -\frac{180\mu}{\Phi_s^2 D_p^2} \frac{(1-\in)^2}{\in^3}\, u_s$$

Where Δp is the pressure drop, L is the bed height, μ is fluid viscosity, Φ_s is particle sphericity, D_p is particle diameter, $\in$ is the void fraction, and u_s is the superficial velocity.

Note the inverse exponential relationship between the pressure drop across the bed and the diameter of the particles being packed into it. When catalyst loadings are small, this can be successfully mitigated on the typical academic lab scale by substantially decreasing the height of the bed. This was the approach taken in **Section 2.2** and in **Chapter 3** when using small quantities of supported precious metals to catalyze hydrogenations. As discussed in Chapter 4, though, there are clear incentives to explore non-PGM catalysts, even when they are less active and require higher loadings. In **Section 2.1**, we explored controlling pressure drop by increasing the particle diameter. The “granular” catalysts used in that section made effective use of that inverse proportionality to minimize pressure drop. Further exploration of that direction was discontinued when it became clear that the use of granular supports was notably curtailing per-gram catalytic activity (see Figure A1 for an example case using hydroquinone oxidation).

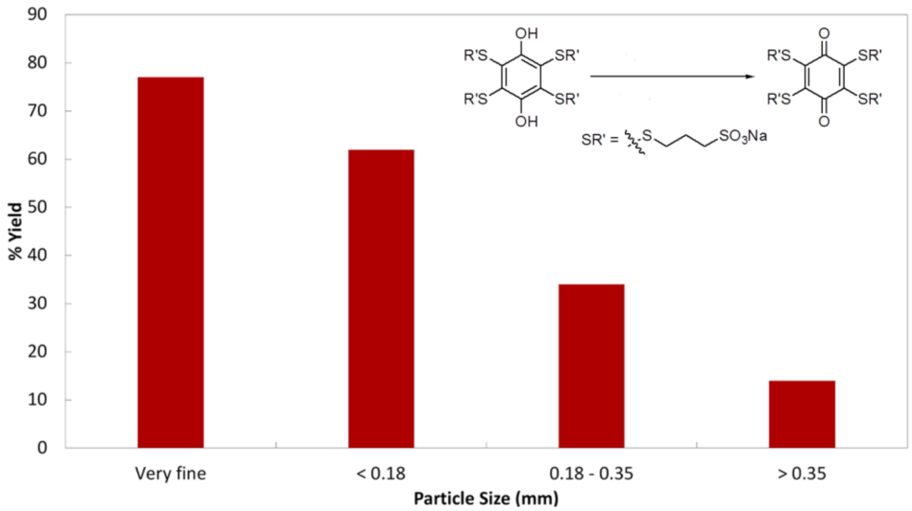

Figure A1: Catalytic activity of a Co-phen/C catalyst for t-MPSNaH$_2$ oxidation. The leftmost bar notes the intrinsic activity of the finely ground catalyst, which then decrease as the size of the catalyst granule (controlled by sieving) increases. Conditions: 0.1 M t-MPSNaH$_2$ in 1M H_2SO_4, 6 mg Co-phen/C, 40 °C, 30 min, 0.3 psig O_2.

Appendix 1 details alternative methods to avoid high pressure drop when dealing with fine powders. **Section A1.1** details the construction of a slurry reactor, which avoids the dynamics of a packed bed entirely, while **section A1.2** details the synthesis of pyrolyzed melamine foams (PMFs) with a high void fraction.

A1.1 A Slurry Reactor Enables Hydroquinone Oxidation by Finely Powdered Catalysts

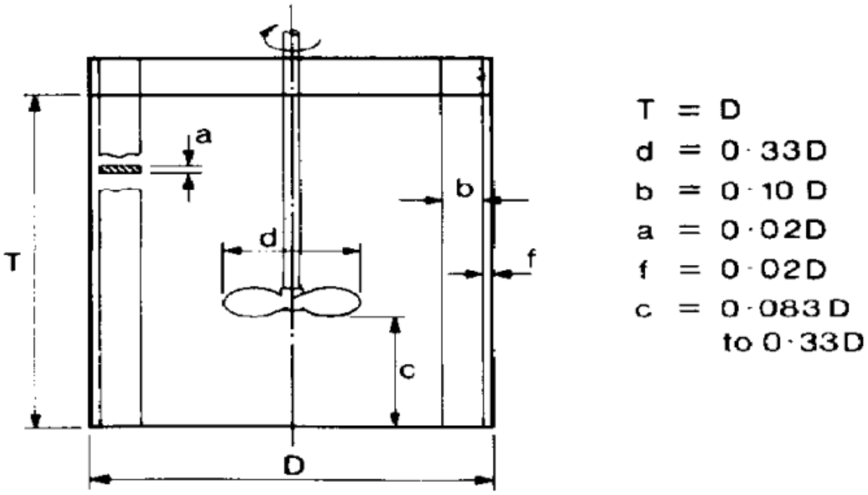

Figure A2: Schematic of a classic flat-bottom slurry reactor. Idealized dimensional ratios for optimal mixing are found to the right, defined in terms of the labeled components on the left.

There are a multitude of reactor configurations suitable for handling fine powders. Given that our system inevitably required three-phase contact, we elected to design a slurry reactor. Slurry reactors suspend a solid within a liquid medium and then bubble gas through that medium, giving us everything necessary to react our hydroquinone (in solution) over our heterogeneous catalyst (solid) in the presence of O_2 (gas). Slurry reactors have been heavily studied and countless iterations exist, but for our lab-scale unit we elected to follow the standards for a simple flat-bottom tank (Figure A2, adapted from the literature[1]).

We selected a beaker as a quasi-flat-bottom vessel, a glass tube with a glass frit as our gas sparger, and machined a stainless steel impeller, canted to promote radial rather than axial flow (**Figure A3**). Components were selected to roughly align with the ideal dimensional ratios, with the farthest departure being our impeller width (d = 0.14D; the 1: 0.33 ratio is important primarily as an upper bound).

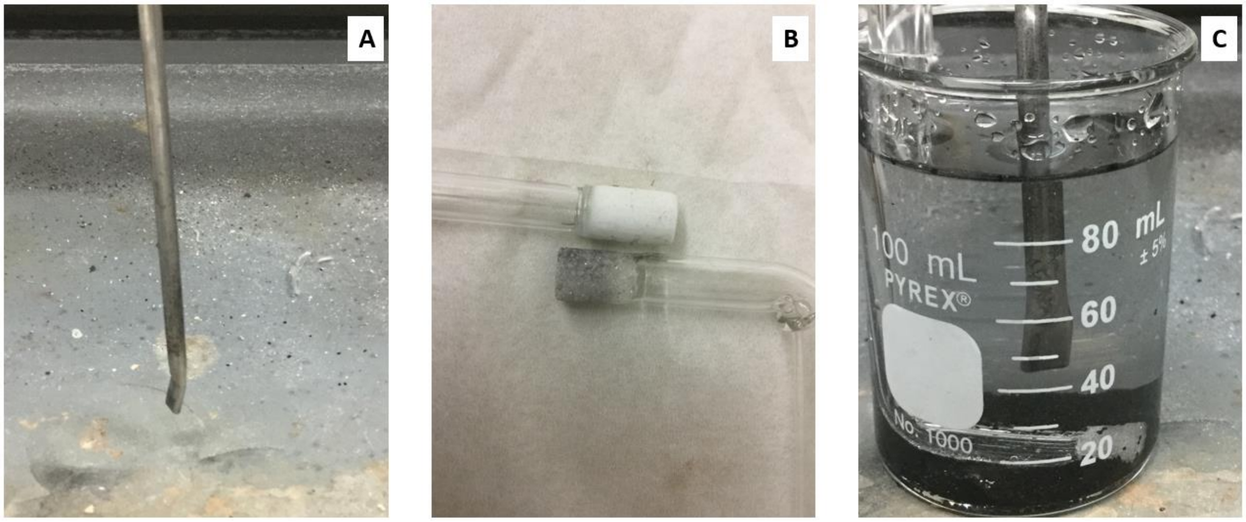

Figure A3: Components for a lab-scale slurry reactor. A. a stainless steel impeller, bottom 1/8” canted to promote radial flow. B. glass frits used to sparge O_2. The bottom frit has been used and is irreversibly contaminated with catalyst, but does not suffer degraded gas sparging. C. The fully constituted reactor, filled with water. An overhead stirrer moves the impeller. A Teflon cap can be safely placed over the top, given a small allowance for the impeller.

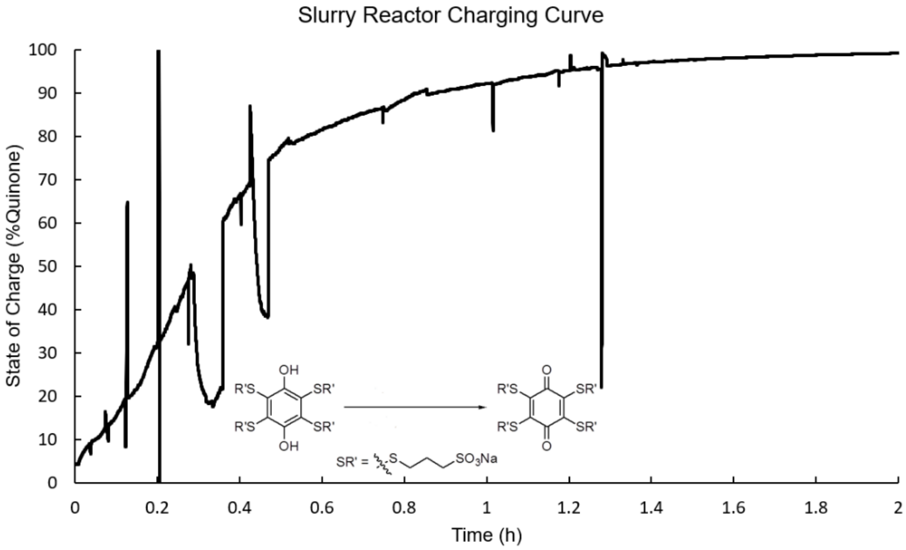

Figure A4: Hydroquinone oxidation in the lab-scale slurry reactor. State of charge was monitored by use of submerged electrodes. The spikes and dips in apparent state of charge are artefacts of operator intervention. Conditions: 80 mL 0.1 M t-MPSNa, 1 M H_2SO_4, 5.0 g Co-phen/C, 62 °C.

To demonstrate the efficacy of the reactor, we enacted a test reaction, oxidizing t-MPSNa hydroquinone using sparged O_2 and Co-phen/C catalyst. Using the potentiometric monitoring approach described in Section 2.1, we were able to observe full conversion of the starting material within two hours (**Figure A4**). This was comparable to the time for full oxidation when circulating through a packed bed reactor.

The slurry reactor has both advantages and disadvantages compared to the packed bed reactor. Its ability to avoid pressure drop is a major boon, but the sparging of O_2 tends to disrupt the readings of submerged electrodes, making potentiometric assays difficult. While a loose-fitting cap can be placed over the vessel to minimize liquid splashing, a tight fit with an impeller using overhead stirring would require a more technically advanced solution. This would present challenges if working with air-sensitive systems or those with highly volatile substrates. Ultimately, the choice of reactor configuration will depend, as always, on the requirements of the specific chemistry being conducted.

A1.2 Pyrolyzed Melamine Foams as M-N-C Materials with High Void Fractions

Melamine is a nitrogen-dense carbonaceous material. It is commonly used to make melamine-formaldehyde copolymer foams, which has applications as a sonic and thermal insulator and as an abrasive cleaner (e.g., “Mr. Clean Magic Erasers”). Much like nitrogenous MOFs, this makes melamine foams potentially interesting as precursors for M-N-C materials. This section is intended as an abbreviated accounting of the procedure for making pyrolyzed melamine foams (PMFs) from Mr. Clean Magic Eraser starting material.

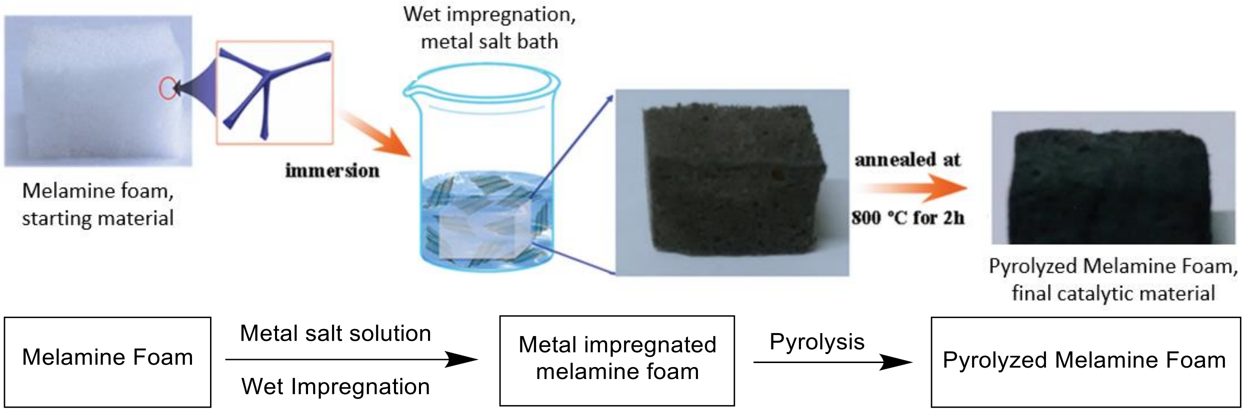

Figure A5: General synthesis of a PMF. The foam precursor is impregnated with metal ions (60 mM aq Co, left to evaporate), pyrolyzed in an inert atmosphere, and can then be used for catalysis. Cartoon renderings adapted from the literature.[2]

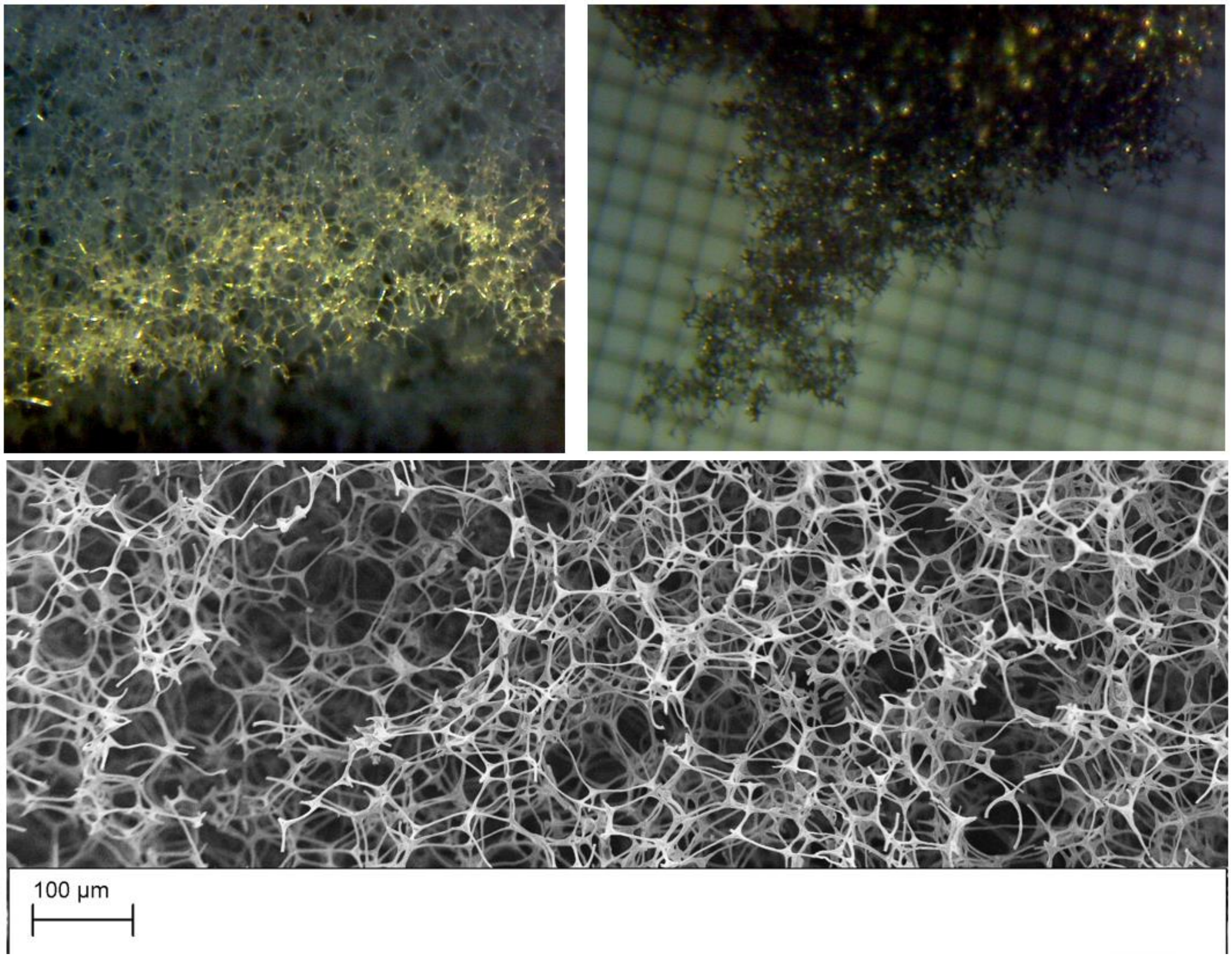

Figure A6: Bulk melamine foam structure before (left) and after (right) pyrolysis shows that the bulk morphology is altered but intact. SEM images at the mm-scale (below) show that the foam matrix is retained despite forcing pyrolysis conditions.

Pyrolysis of these melamine foams shows substantial retention of the initial foam matrix, suggesting that the void fraction of the final material remains extremely high (**Figure A6**). Initial activity benchmarking of PMF materials suggests they are catalytically active, although the rates of oxidation are much slower than the most active M-N-Cs discussed previously. Screening of pyrolysis conditions indicates that “moderate” pyrolysis temperatures of approximately 800 °C lead to optimal performance (**Figure A7**). The catalyst performs equally well when reacting as a single 1 cm^3 unit or when finely ground, indicating that unlike the granular M-N-Cs in **Section 2.1**, these experience no internal diffusion limitation or sequestering of active sites.

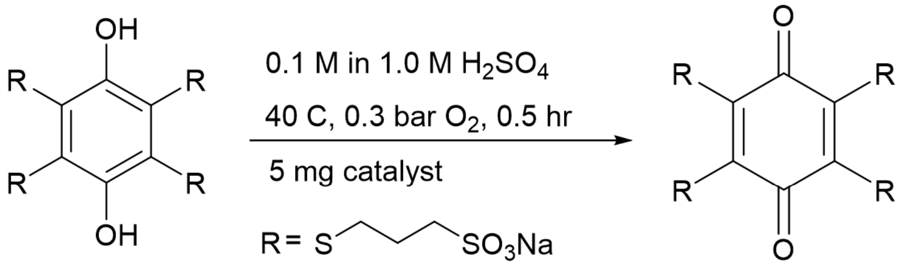

Pyrolysis Conditions		
Temperature	Time	Conversion
700ºC	3h	34%
800ºC	3h	54%
900ºC	3h	49%

Figure A7: Screening of PMFs for hydroquinone oxidation activity at various pyrolysis temperatures.

The lack of diffusion limitations can be partially explained by the existence of the large internal channels, but it also implies a lack of microporous structure. Highly microporous materials, no matter how thoroughly riddled with diffusional macro-channels, will typically lose active sites due to restrictive apertures. Both N_2 adsorption data and SEM images confirm this lack of microporosity (**Figures A8**, **A9**). This suggests that the mediocre activity of these materials is perhaps due to a low number of active sites rather than intrinsically low site activity.

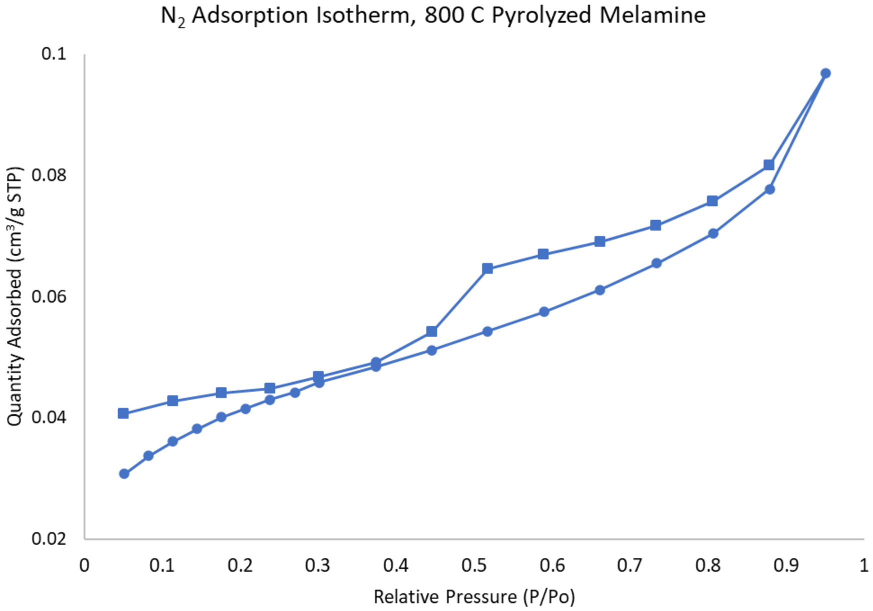

Figure A8: N_2 adsorption isotherm of Co-PMF pyrolyzed at 800 °C. The calculated BET surface area of this material is only 7 m^2/g, indicating that it is effectively non-porous.

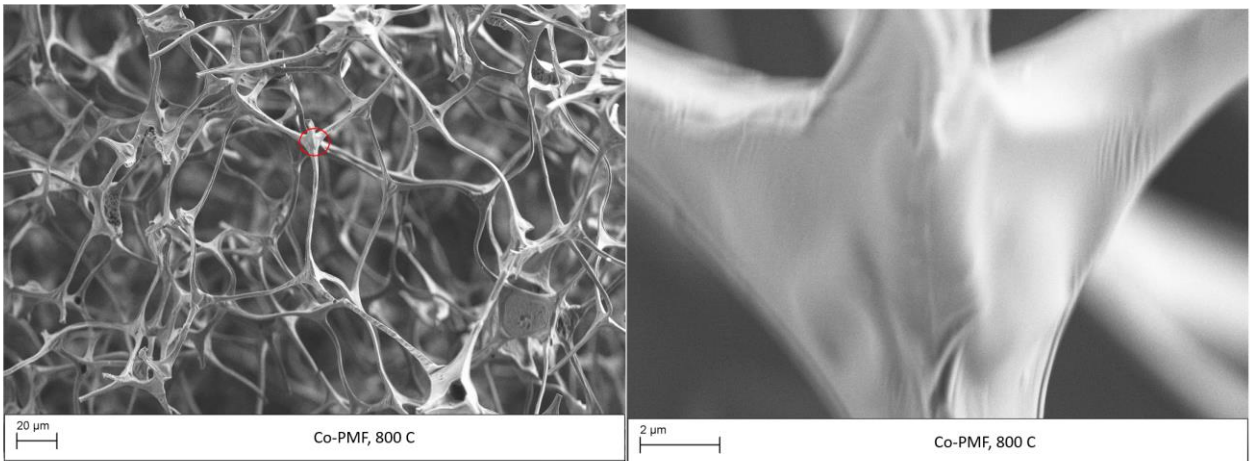

Figure A9: SEM images of Co-PMF pyrolyzed at 800 °C. The left frame covers hundreds of micrometers and shows the bulk structure of the foam. By zooming in further to the right frame (pictured inside the red circle, left), we can see that the structure of the PMF does not show any visible porosity.

Regardless of its origin, the lack of high activity poses a problem for further development of PMFs. They do not compare favorably even with the previously used granular M-N-Cs already published. With that said, there is at least one potential direction for them moving forward. While they don't compete well with our best M-N-C catalysts, they *do* compare favorably to the complete lack of activity found in traditional solid monolith structures (which are not conventionally catalytic in nature). Research into PMFs as monolithic structures, meant for being coated with more active catalysts, may both solve the pressure drop problem that fine catalyst powders face and increase the net activity of a PMF-filled reactor.

References

---

1. Chudacek, M. W. Solids Suspension Behaviour in Profiled Bottom and Flat Bottom Mixing Tanks. *Chem. Eng. Sci.* **1985**, *40*, 385–392. DOI: 10.1016/0009-2509(85)85100-9.

2. Zhang, P.; Wang, R.; He, M.; Lang, J.; Xu, S.; Yan, X. 3D Hierarchical Co/CoO-Graphene-Carbonized Melamine Foam as a Superior Cathode toward Long-Life Lithium Oxygen Batteries. *Adv. Funct. Mater.* **2016**, *26*, 1354–1364. DOI: 10.1002/adfm.201503907.